Università degli Studi di Padova
Dipartimento di Fisica ed Astronomia
"Galileo Galilei"

Tesi di laurea magistrale in Fisica

High-frequency Electron Paramagnetic Resonance (EPR) studies of hetero-trinuclear 3d-4f metalorganic Ni_2Ln-complexes (Ln = La, Ho)

Laureando: Simone Fiorentini

Relatore interno: prof. Marco Bazzan

Relatore esterno: prof. Rüdiger Klingeler
Correlatore esterno: dott. Changyung Koo

Controrelatore: prof. Alberto Carnera

Anno accademico 2016/2017
Sessione di laurea invernale

Contents

Abstract

Composti eterometallici di ioni di metalli di transizione e terre rare hanno recentemente suscitato interesse per le loro possibili applicazioni nel campo dei magneti molecolari, grazie all'elevata anisotropia magnetica dovuta al forte accoppiamento spin-orbitale e alla possibilità di avere accoppiamento magnetico intramolecolare. Due composti in polvere del tipo 3d-4f nella forma $[Ln(III)Ni(II)(L^{tacn})_2]ClO_4$, dove Ln=La, Ho, sono stati studiati per mezzo di spettroscopia a risonanza paramagnetica elettronica ad alta frequenza ed alto campo (HF-EPR), in un campo magnetico con intensità fino a 16 T e frequenze nel range 50 - 450 GHz. L'analisi dei dati tramite fit lineare e simulazione di un hamiltoniana efficacie di spin permettono di ottenere informazioni sull'anisotropia magnetica e sul g-factor nel caso della presenza di uno ione 4f non paramagnetico (La). La simulazione è stata poi adattata al caso di ione 4f con alto momento angolare totale (Ho), permettendo di determinare i cambiamenti nell'anisotropia e nell'interazione di scambio con l'introduzione di un elemento 4f magnetico nel complesso trinucleare. Dai risultati sul Ni_2La si dimostra la necessità di implementare un programma in grado di riprodurre l'orientazione dei singoli spin ricavata dai dati cristallografici. L'implementazione di un termine di Ising nell'hamiltoniana permette di adattare la simulazione al campione di Ni_2Ho, e i risultati dimostrano la presenza di un lieve accoppiamento ferromagnetico tra ioni Ni(III) e Ho(II), conducendo alla possibilità di applicazione di tale composto come Single Molecular Magnet.

Chapter 1

Introduction

Recent reasearch in physics and chemistry has brought up a growing interest in the field of the so-called nanoscience. When building devices with smaller and smaller size, quantum interactions become increasingly important but the physics can still be studied deeply and in great detail.

Fig. 1.1 [1] shows the hierarchy of phenomena in ferromagnetic systems associated with different system sizes. At macroscopic sizes, a magnetic system is described by magnetic domains, regions of space where all the spins align in the same direction, separated by domain walls and this brings the system close to a minimum of the free energy. However, when we consider a system whose spatial extent is of the order of magnitude of the domain walls width or of the exchange length, the formation of domain walls becomes energetically unfavorable, and single-domain behaviour arises. At this point, the anisotropy barrier for magnetization reversal becomes strongly dependant on the system size and shape. Eventually, when the size is small enough, the energy of the barrier becomes comparable with the thermal energy of the system, magnetization can fluctuate and the system is no longer ferromagnetic.

For sizes well below the domain walls width, one must explicitly take into account the behaviour of spins, which represent single magnetic dipoles, and their coupling: the best candidates for observing this behaviour are Single Molecular Magnets (SMMs). The first SMMs synthetized were metal-organic molecular clusters containing a finite number of paramagnetic centers [2]: the organic bridges in the system connect these centers via the superexchange interaction, thus creating a well-isolated spin ground state. The main objective of this type of approach is to produce molecules with a large intrinsic magnetic dipole moment, and which presents an axial anisotropy, arising from the crystal field: in this case, the anisotropy creates a preferred orientation for the magnetic dipoles and the splitting of energy levels depending on the value of $|m_S|$, and the hysteresis of the magnetization is given by discrete jumps between energy states with different values

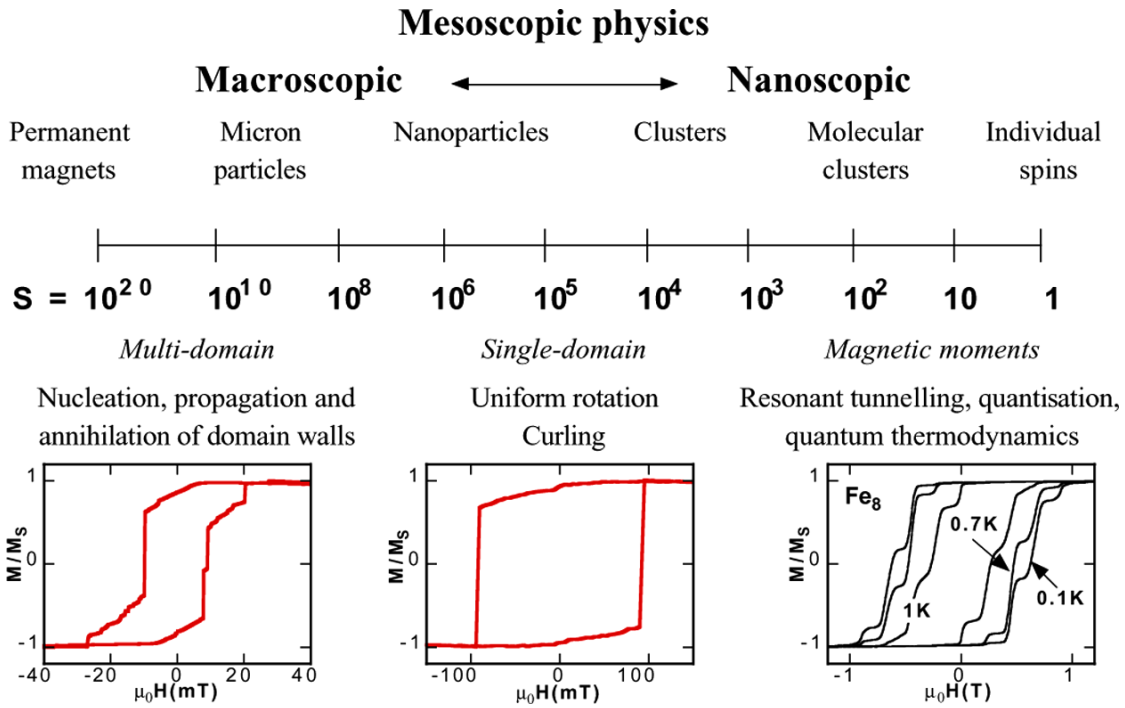

Figure 1.1: The hierarchy of magnetization phenomena as a function of system size. The system size is given as the number of magnetic dipoles in the system.

of $|m_S|$. Thus, the anisotropy creates an energy barrier $U = |D| \left(S^2_{z,max} - S^2_{z,min}\right)$ (where D is the parameter characterizing the anisotropy of the spin centers) between states with $m_S < 0$ and $m_S > 0$, and a related blocking temperature T_b at which the hysteresis process starts to take place: increasing this temperature is the main objective in the SMMs research, as higher T_b yields a higher working temperature for the possible applications.

In quantum computing applications [3], the fact that the hysteretic behaviour originates from single molecules creates the possibility of dealing with q-bits of molecular size. Applications to data storage are also possible, with highly localized molecular units with magnetization retention [4], as well as medical applications in the framework of magnetic resonance imaging and drug delivery [5].

In the early 2000s new candidates for SMM behaviour started being discovered, which focused on the use of lanthanide ions [6][7]. Lanthanides are good candidates for SMMs because they possess a large single-ion anisotropy, producing a well isolated high spin ground state even on their own. The first compounds containing Lanthanide ions were synthetized in 2005[8]. The interesting property of these new compounds was their record blocking temperature, the temperature at which the magnetization hysteresis process first shows up, reaching temperatures as high as

40 K. To better exploit their single ion anisotropy, they were also coupled with paramagnetic centers that present a strong crystal field anisotropy, thus producing the so called *3d-4f* compounds.

The production and the characterization of new *3d-4f* compounds is thus fundamental in the progress of this kind of research. This thesis focuses on the characterization of two newly produced *3d-4f* compounds, which are part of a batch of metallorganic complexes with chemical formula $[Ln(III)Ni(II)(L^{tacn})_2]ClO_4$, where Ln is a lanthanide ion, usually referred to as Ni_2Ln. This compounds are characterized by the presence of two different molecular orientations inside the crystal unit. The two compounds considered in this thesis are Ni_2La and Ni_2Ho. The first was chosen because Lanthanium is non paramagnetic ion, thus permitting to study the Nickel ion properties without worrying of the lanthanide. The second was chosen due to the high single-ion anisotropy and magnetic moment (total angular momentum J=8) typical of Holmium. The comparison between the two can give information both on the strength of the coupling between the Ni(II) and Ho(III) ions and on the influence that the substitution of Lanthanum with Holmium has on the magnetic parameters of the Nickel ions.

The study was conducted by means of Electron-Paramagnetic resonance (EPR). This technique is often used for determining the crystal field anisotropy properties of 3d metals compounds, and has recently been employed in the study of the exchange coupling between lanthanides and transition metal ions [9] [10]. The resonance data gathered from EPR Spectroscopy at low temperature ($T < 10$ K) were first linearly fitted in order to gain a first overview of the g-factor and anisotropy parameters of the system, and a temperature dependance measurement was undertaken to help determine which feature should be ascribed to transitions from the ground state of the system. The Ni_2La sample was analyzed first in order to allow the determination of the correct rotation matrices to employ to describe the different Nickel spins orientations concurring to the energy of the system. A Matlab script was developed to build the rotation matrices and insert them into the system Hamiltonian, which was then used to simulate the resonance data and determine the system parameters, such as the Ni ions anisotropy and coupling. For the second compound the previous Hamiltonian was adapted with the insertion into the script of a term behaving as an Ising spin with high spin-value S=8, capable of describing the ground-state behaviour of the lanthanide. The new Hamiltonian was used for determination of the Nickel ions anisotropy properties inside the second compound, evidencing the differences arisen by the change of the Lanthanide in the system, and was also able to determine the presence of weak electromagnetic coupling, which increases the potential of SMMs applications of this kind of compounds.

Chapter 2

Single Molecular Magnets Overview

When SMMs where first uncovered, the objective of increasing the anisotropy barrier, and thus the blocking tempeerature (see Eq. 2.2) was mainly pursued by creating the gratest possible clusters of coupled spin centers. Molecules with high effective spins have already been realized in the past, the record being hold by the ferromagnetically coupled Mn_{19} cluster with a very high ground state spin of $S = \frac{83}{2}$ [11]. One thing that makes this compunds successful is that they can be organized in single crystals made by a macroscopic number of identical clusters. To retain zero dimensionality, which means, to retain molecular (microscopic) behaviour from macroscopic crystals, the clusters are usually encompassed in an organic shell which suppresses intramolecular coupling.

2.1 Single Molecular Magnets Properties

The two most prominent representative of this particular kind of compounds, usually referred to as the prototypes of their kind, are the $Mn_{12}Ac$ and Fe_8 compounds. Their chemical formulas are

$$Mn_{12}O_{12}(O_2CCH_3)_{16}(H_2O)_4$$

and

$$[(C_6H_{15}N_3)_6Fe_8O_2(OH)_{12}]Br_7(H_{20})Br \cdot 8H_2O$$

respectively.

The first synthesis of the $Mn_{12}Ac$ compound was carried over by Lis in 1980 [2]. This compound will be briefly described in order to gain a better understanding of the prototypical behaviour of a Single Molecular Magnet. In this cluster, pictured

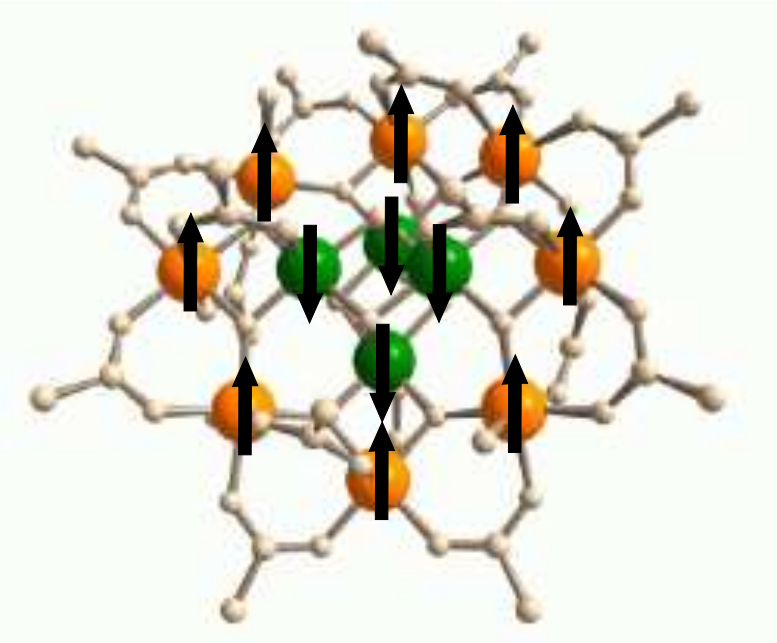

Figure 2.1: Crystal structure of Mn12Ac. The Mn^{3+} ions have been indicated by orange spheres, while the Mn^{4+} ones are green. The disordered acetic molecules are omitted for clarity.

in Fig. 2.1, the four inner Mn^{4+} ions ($3d^3$, $S_{Mn4} = 3/2$) are ferromagnetically coupled via bridge O atoms, and form a single spin unit with $S = 3/2 \cdot 4 = 6$. This unit has spin antiparallel to that of the outer ring of Manganese atoms, which are Mn^{3+} ions ($3d^4$, $S_{Mn3} = 2$), yielding a total ground state spin of $S = 2 \cdot 8 - 6 = 10$. What is found in the complex is a negative high axial magnetic anisotropy, with $D = -0.72K$, which removes the $2S+1$ degeneracy of the ground state multiplet, dividing it into 21 levels, with $m_S = \pm 10, \pm 9, \ldots, \pm 1, 0$, with increasing energy. The states with $m_S = \pm 10$ have the same energy, yielding a bi-stable ground state, where the $m_S = 10$ one can be viewed as the "spin-up" state, and the $m_S = -10$ as the "spin-down" state. This bi-stable ground state is common among high spin SMMs. As the two lowest energy states represent two different spin orientation, they are separated by the energy barrier

$$U = |D| \left(S^2_{z,max} - S^2_{z,min} \right) \tag{2.1}$$

which strongly influences the low temperature behaviour of the cluster if polarized. For temperatures $T < U/k_B$ the relaxation time τ of the magnetization depends on the height of the barrier according to the Arrhenius equation

$$\tau = \tau_0 \exp\left\{ \frac{U}{k_B T} \right\} \tag{2.2}$$

where τ_0 is the pre-exponential factor. Therefore, the relaxation time goes up (and the relaxation process slows down) with an increase in the ratio of U/k_BT, and this yields to an hysteretic behaviour of the magnetization.

The term *Single Molecular Magnets* is due to the fact that, as shown, this hysteretic behaviour arises only due to molecular properties, and not due to the presence of a macroscopic number of aligned spins like in bulk magnets. As is clear from Eq. 2.2, the hysteretic behaviour mainly arises below a certain temperature regime. This regime is defined by the so called blocking Temperature, T_B.

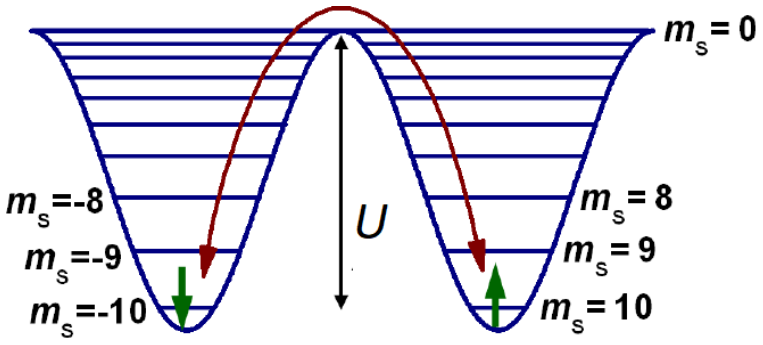

(a) Thermal mechanism for the relaxation of magnetization.

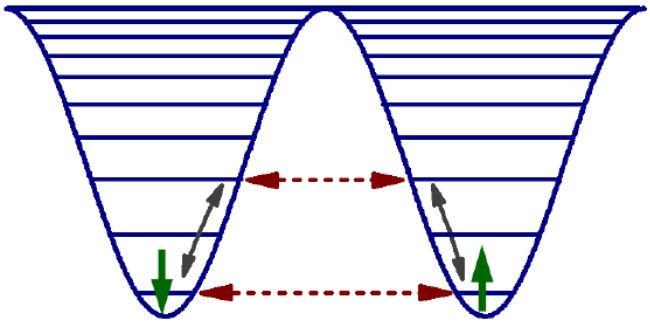

(b) QTM mechanism for the relaxation of magnetization.

Figure 2.2: Energy levels for $m_S > 0$ and $m_S < 0$ (splitted by axial single ion anisotropy), separated by an energy barrier U

2.1.1 Quantum Tunneling of The Magnetization

Thermal activation is not the only mechanism yielding to the relaxation of the magnetization. This was first observed in 1996, when unusual steps where found in the hysteresys loop $Mn_{12}Ac$ at regular magnetic field intervals. Each step was

due do a sudden substantial increase in the magnetic relaxtion rate. The mechanism underlying this particular behaviour is now known as *quantum tunneling of magnetization* (QTM), owing to the fact that the magnetization vector goes thorugh the potential barrier, directly from states with $m_S < 0$ to $m_S > 0$, without passing from the maximum energy state ($m_S = 0$). The situation is schematized in Fig. 2.2. This effect is not yet fully understood, but it is closely related to the crystal field symmetry of the system: ortorhombic (in-plane) and higher order anisotropy may yield to the admixture of isoenergetic states on different sides of the barrier, and thus to a finite probability of transition between them.

2.2 3d-4f Compounds

In the early 2000s new candidates for SMM behaviour started being discovered, which focused on the use of lanthanide ions [6][7]. Lanthanides are good candidates for SMMs because they possess a large single-ion anisotropy, producing a well isolated high spin ground state even on their own. In 2004, Ishikawa and coworkers reported mononuclear TBA-[Ln(Pc)$_2$] complexes [8], which were the first mononuclear SMMs and the first lanthanide SMMs. The TBA[Ln(Pc)$_2$] complex displayed frequency-dependent ac out-of-phase blocking temperature peaks peaks as high as T_B=40 K and had energy barriers of $U_{eff}/k_B = 230$ K and $U_eff/k_B = 28$ K with Ln = Tb and Ln = Dy, respectively. After these developments, the quest for improved SMMs took a new approach: to combine *3d* and *4f* metal centres in the same complex to obtain SMMs that would have higher working temperatures than those obtained for *3d* metal SMMs.

In lanthanide ions the large ground state spin is not given by ferromagnetic coupling between different centers, or by an high number of unpaired electron, but by the fact that spin-orbit coupling is way stronger than the crystal field, and so their magnetic properties are ruled by the total angular momentum J, which has the maximum value of $|L + S|$ for more than half-filled f shells (Tb, Dy, Ho, Er, Tm, Yb, Lu) and the minimum value of $|L - S|$ for less than half-filled f shells (Ce, Pr, Nd, Pm, Sm, Eu). A strong magnetic moment is determined just by a high value of m_J. The ground state bistability characteristic of a SMM arises from the m_J sublevels of the $^{2S+1}L_J$ term.

After the discovery of a possible use of lanthanide ions in the design of new SMMs, effort was poured into finding a way to better exploit their large single-ion anisotropy. Some simple rules were, for example, proposed by Long and Richards in 2011 [6]. For polynuclear complexes design, the best results can be obtained by combining lanthanides with paramagnetic centers that present a strong anisotropy: in this way, the anisotropy of the molecular complex will be a combination of the single-ion anisotropies of all the paramagnetic metal centres involved. With this

Ln	$\mathbf{g}_{Ni}$	**D**(K)	**E**(K)	**J**(K)
Tb	2.07(4)	4.5(2)	-0.58(6)	-0.216(12)
Dy	2.10	3.7	-0.73	0.031
Ho	2.03(7)	3.73(8)	-0.70(3)	-0.122(3)

Table 2.1: Hamiltonian parameters for three 3d-4f compounds in the form [Ln_2Ni] [10]. The parameter g is the giromagnetic factor, which for a free electron is equal to 2. D and E are parameters charazterizing the Ni spin centers anisotropy. J is the exchange coupling between Ni and Ln ions.

in mind, the most anisotropic *3d* metal ions must be the best candidates for the design of lanthanide-based SMM complexes.

The greatest problem with *3d-4f* systems is the coupling between paramagnetic centers. As it has been explained, in order to produce a well-isolated ground state, the coupling should be strong and ferromagnetic. Moreover, this is also needed in order to avoid mixing of low-lying excited states that can cause QTM to occur.

In *3d-4f* ions, the exchange coupling tends to be weak or very weak. *3d* ions are used in this complexes also for their long-extending *3d* orbitals, which can more easily interact with the inner *4f* orbitals of lanthanides, and the strongest possible coupling is usually achived through the use of oxygen bridges. Several *3d-4f* SMMs were already reported, both in tetranuclear (see for example [12], [13]) and trinuclear form ([14], [9]), and were analyzed by various means.

2.2.1 3d-4f Characterization Thorugh EPR

One of the ways of characterizing the properties of such a complex is the use of Electron Paramagnetic Resonance Spectroscopy, which, even if it cannot directly value the nergy barrier or blocking temperature of the system, it can give informations both about the paramagnetic properties of the 3d ions and the coupling between 3d and 4f ions: having ferromagnetic coupling and a strong 3d ion anisotropy is the starting point in the realization of a good 3d-4f SMM. In table 2.1 are reported the magnetic parameters obtained on 3d-4f compunds of the class [Ln2Ni] through the use of electron paramgnetic resonance by Okazawa [10]. The most important achievement for this compounds is the presence, in almost all of them, of ferromagnetic coupling. The chemical structure of this compounds is the same of the second one reported in Fig. 2.3 (below).

The present thesis work will focus on the use of EPR Spectroscopy in the parametrization of newly produced candidates for 3d-4f SMMs in the form [Ni_2Ln]. In particular, it will focus on the confrontation of the Ni parameters in two different compounds, one containing a non paramagnetic La(III) ion, the other containing

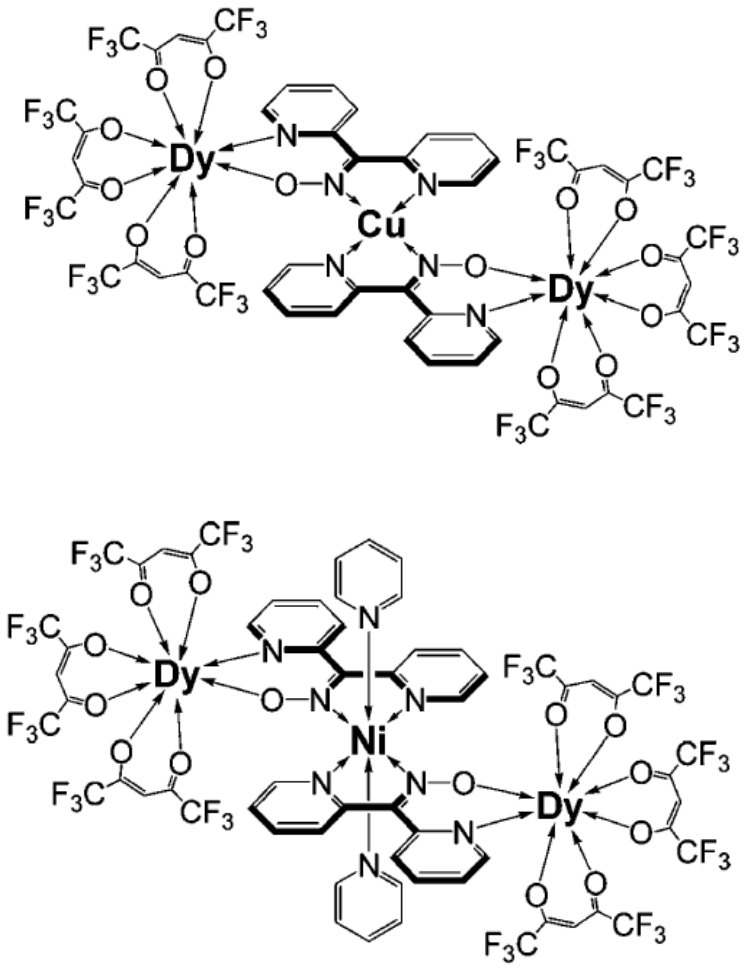

Figure 2.3: Examples of *3d-4f* SMMs molecular structure (Dy-Cu-Dy and Dy-Ni-Dy, respectively), as reported by Okazawa [9] [10].

a highly paramagnetic Ho(III) ion, and in the evalutaion of the exchange coupling between Ni and Ho ions.

Chapter 3

Electron Paramagnetic Resonance

Electron Paramagnetic Resonance (EPR), also known as Electron Spin Resonance (ESR), is a spectroscopic technique widely used to study paramagnetic species, in particular, those found in metal complexes or organic radicals. The method is similar to the Nuclear Magnetic Resonance (NMR), greatly used for medical imaging [15]. Both techniques are based on the excitation of transitions between adjacent energy levels in a spin system subjected to a magnetic field. The difference is that, while the latter technique employs nuclear spins, electron spins are the ones subject to excitation in EPR, so the electromagnetic radiation frequency needs to be much higher than in NMR ($\sim$MHz in NMR, $\sim$GHz in EPR). The method can be used to study a wide variety of materials with unpaired electrons (i. e. with non-null total angular momentum), such as metal complexes or organic radicals, but also defects in solids, liquids, gases, etc.

This chapter will give a theoretical background to the EPR technique. First, the simple resonance with one free electron will be analyzed. Then, the description will focus on the effects of the presence of many electrons and of the crystal field on the system properties. The spin-Hamiltonian approach will be introduced: this allows to connect the effects described before to simple parameters, which can be used to characterize the system.

3.1 Free electron resonance

The basic concept of EPR is to study the effects of an applied magnetic field on the energy of a system. This is possible due to the electrons' spin: even in the absence of angular momentum, the presence of spin ensures the existence of a magnetic dipole, $\vec{\mu}$, that can interact with the magnetic field $\vec{B}$.

The intrinsic magnetic moment of a particle with spin is [16]

$$\vec{\mu} = -\frac{g\mu_B}{\hbar}\vec{S} \tag{3.1}$$

Here μ_B is the Bohr magneton, g is the giromagnetic factor (or g-factor), $\vec{S}$ is the spin operator which can take the discrete values $\sqrt{S(S+1)}\hbar$, and a z-component with magnitude $m_S = \{-S, -S+1, \ldots, S-1, S\}$. The exact value of g for a free electron, predicted by quantum electrodynamics and in good agreement with experiments, is

$$g_e \approx 2.00232 \tag{3.2}$$

However, for almost any solid state physics application, one can use the approximate value

$$g_e = 2 \tag{3.3}$$

Using these premises and assuming to have an external magnetic field in the form $\vec{B} = B\hat{e}_z$, the energy of the interaction of a particle with spin and the given magnetic field is of the form

$$E = -\vec{\mu} \cdot \vec{B} = g\mu_B m_S B \tag{3.4}$$

so the energy of the system splits in $N = 2S + 1$ levels: this is known as the *Zeeman Effect*.

In the case of a single electron, S is equal to $\frac{1}{2}$, and m_S can take the values $\pm\frac{1}{2}$, so the energy splits in only two levels, as seen in Fig. 3.1. The energy difference between the two levels can be measured because, thanks to Planck law, one can use the equivalence

$$\Delta E = h\nu = g\mu_B \left|\Delta m_S\right| B \tag{3.5}$$

This means that, by using electromagnetic radiation at the proper frequency, it's possible to stimulate the transition of the system from one level to the other, and so one can measure the energy difference by varying the frequency of the radiation or the applied field. According to Boltzmann statistics, the population ratio of the two different levels is given by

$$\frac{n_{up}}{n_{low}} = \exp\left(-\frac{\Delta E}{k_B T}\right) = \exp\left(-\frac{h\nu}{k_B T}\right) \tag{3.6}$$

Even considering an experiment at room temperature, $T = 298K$, and with a frequency of 50 GHz, equation 3.6 gives a population ratio of 0.992, which means that the excited state is slightly less populated than the lower one. The resonance will thus always result in absorption. Obviously, the absorption at room temperature will be very weak, because the population of the two states are almost the same. This is why the majority of EPR experiments are performed at low temperature. The present thesis focuses on experiments carried out between 2 and 40 K, where the population ratio is lower (0.3 for $T = 2K$) and permits to see clearly the absorption features typical of EPR spectroscopy.

From the free electron example, it's evident that EPR can be used to study a system behaviour under a magnetic field using electromagnetic radiation absorption spectra.

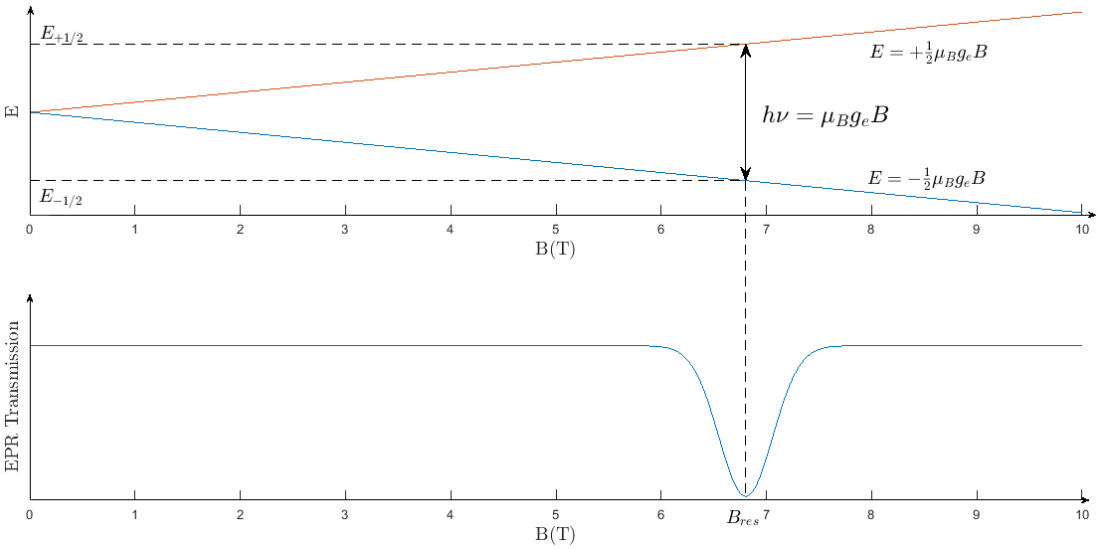

Figure 3.1: Energy levels of a free electron system and relative absorption spectra for a frequency $\nu = 200GHz$.

3.2 Many-Electron Ions

The simple free electron model given in paragraph 3.1 is useful to introduce the concept of EPR Spectroscopy, but is not sufficient for most real cases. For example, a typical transition metal atom will contain many electrons. Although most of them are bound in filled shells, which have no net angular momentum, there may be electrons in unfilled shells. The spins and angular momentum of these external electrons will combine to give non-zero spin and orbital angular momentum. The atom itself will thus possess a non-zero total angular momentum, which can interact with the magnetic field used in EPR. This leads to the necessity of finding some simple rules to help estimate what the total angular momentum of a free ion will be in the ground state, in order to help predict it's behaviour when EPR Spectroscopy is performed on such ion.

3.2.1 The Landé factor

In the case of a system with many electrons, thus possessing both spin and orbital angular momentum, with a gyromagnetic factor g_L, the total magnetic moment becomes

$$\vec{\mu} = \mu_B(g_L\vec{L} + g_e\vec{S}) \tag{3.7}$$

and the energy of the interaction with an external magnetic field is of the form

$$E = -\vec{\mu}\cdot\vec{B} = \mu_B(g_L\vec{L} + g_e\vec{S})\cdot\vec{B} \tag{3.8}$$

Due to the presence of spin-orbit coupling, $\vec{S}$ and $\vec{L}$ are usually not preserved, but the total angular momentum, $\vec{J}$, is. Equation 3.8 can thus be rewritten as

$$E = \mu_B g_J \vec{J} \cdot \vec{B} \tag{3.9}$$

with the total magnetic moment being

$$\vec{\mu} = -\mu_B g_J \vec{J} \tag{3.10}$$

It can be shown [16] that the factor g_J, or Landé factor, has the form

$$g_J = \frac{J(J+1)(g_L + g_e) + [L(L+1) - S(S+1)](g_L - g_e)}{2J(J+1)} \tag{3.11}$$

which, using the approximate value $g_e = 2$ and value $g_L = 1$, reduces to

$$g_J = \frac{3}{2} - \frac{L(L+1) - S(S+1)}{2J(J+1)} \tag{3.12}$$

3.2.2 Hund's Rules

In order to determine the ground state of a free, many-electron ion, a set of three empirical rules determined by Hund can be employed. These rules, once the valence shell configuration is known, yield the spin and orbital angular momentum quantum numbers that minimize the energy of the ion. The three rules are as follows:

1. choose the maximum value of the spin angular momentum, S: in this way the Coulomb energy is minimized because of the Pauli exclusion principle;

2. choose the maximum value of the orbital angular momentum, L, consistent with rule 1: one can imagine that, by having all the electrons "rotating" in the same direction, they tend to remain further apart from each other, and thus reduce Coulomb repulsion;

3. choose the value of the total angular momentum, J, as:

   - $|L - S|$ if the shell is less than half full, or
   - $L + S$ if the shell is more than half full.

   This third rule arises from an attempt to minimize the spin-orbit energy.

One should note that the third rule is only valid when the spin-orbit coupling is not overcome by some other effect. This is true, for example, for rare earth ions (e.g. lanthanides), but not for transition metals: in this case the effect of the crystal field is much more significant than spin-orbit coupling. These two effects will be described in the following paragraphs.

3.2.3 Spin-Orbit Coupling

When trying to predict the magnetic behaviour of electrons bound in an ion, the first thing to take into consideration is the fact that they do not possess only spin angular momentum, $\vec{S}$, but also orbit angular momentum, $\vec{L}$. An electron orbiting around a nucleus produces a current, and so a magnetic field, proportional to $\vec{L}$. The interaction between this magnetic field and the electron's spin magnetic moment can be written as:

$$\mathcal{H}_{SO} = \frac{e\hbar^2}{2m_e c^2 r}\frac{dV(r)}{dr}\vec{S}\cdot\vec{L} \tag{3.13}$$

where V(r) is the Coulomb potential. For an hydrogen-like atom

$$\frac{1}{r}\frac{dV(r)}{dr} = \frac{Ze}{4\pi\epsilon_0 r^3} \tag{3.14}$$

This interaction is known as *spin-orbit* or *L-S coupling*. It is usually taken into consideration as a weak perturbation to the main Hamiltonian of the system, and because of this, $\vec{L}$ and $\vec{S}$ are not separately conserved, while the total angular momentum, $\vec{J} = \vec{L} + \vec{S}$, is. If relativistic effects can be considered negligible, which is the case of this thesis work and most EPR applications, $\vec{L}^2 = L(L+1)$ and $\vec{S}^2 = S(S+1)$ are still preserved quantities. States with a certain value of L and S are split into a set of sublevels based on their total angular momentum J. This quantum number is associated with the quantity $\vec{J}^2 = J(J+1)$, and can assume values

$$|L - S| \leq J \leq L + S \tag{3.15}$$

Since the spin orbit interaction, from equation 3.14, takes the form

$$\mathcal{H}_{SO} = \left\langle \lambda\vec{L}\cdot\vec{S} \right\rangle \tag{3.16}$$

with λ being a proportionality factor, the expected energy values are, remembering the definition of $\vec{J}$

$$\left\langle \frac{\lambda}{2}\left(\vec{J}^2 - \vec{L}^2 - \vec{S}^2\right) \right\rangle = \frac{\lambda}{2}\left[J\left(J+1\right) - L\left(L+1\right) - S\left(S+1\right)\right] \tag{3.17}$$

The difference between each of these levels is λJ, and they can be split up into their degeneracy m_J by applying a magnetic field. Thus, for atoms with both L and S, the interaction with the magnetic field is given by the ground state value of J, and not of L and S separately.

Since the spin orbit interaction depends on Z^4, with Z the atomic number [16], the interaction can not be seen as a weak perturbation for atoms with high Z. In this case, a better scheme is known as *i-i coupling*: here the spin-orbit interaction is the dominant energy and we couple the spin and orbital angular momentum of each electron separately.

3.3 Molecular Magnetism

The previous section explained the magnetic properties of ions considering them to be isolated, with negligible interaction with their surroundings. In this paragraph, the effect of the crystalline environment is discussed. This is important in the case of transition metal ions, where the effects of the crystal structure are strong enough to compete with spin-orbit coupling, and thus must therefore be taken into consideration.

3.3.1 Crystal Field

The influence of crystal field on the magnetic properties of paramagnetic ions is due to the Coulomb interaction between the electric charge distribution of the ligands, the non magnetic ions in the crystal, and the electrons of the ion under study.

This effect is greater for electrons with a distribution which reaches great distances from the nucleus, as they are less shielded from their surroundings. In rare earths, the magnetic electrons are in the *4f* or *5f* orbitals, which are located near the nucleus and thus shielded by the outer shells, so crystal field effect are negligible. For transition metal atoms, however, the last occupied orbital is usually *3d*, so the electrons are less shielded and the crystal field potential is stronger than spin-orbit coupling.

Octahedral Symmetry

A common case to consider is the octahedral environment. This is because in many transition metal compounds a transition metal ion sits at the centre of an octahedron with other ions, such as oxygen, on each corner. For the following description, a reference system with the x, y and z axis pointing along the lattice vectors will be considered.

The *3d* orbitals, which constitute the non-filled shell for transition metal ions, can be divided into two classes, represented in Fig. 3.2:

the t_{2g} orbitals , which point between the x, y and z axes, called d_{xy}, d_{xz} and d_{yz} orbitals;

the e_g orbitals , pointing along the axes, called d_{z^2} orbital, which has lobes pointing along the z axis, and $d_{x^2-y^2}$ orbital, which has lobes pointing along both the x and y axes.

In the case of spherical symmetry, the paramagnetic ion can be imagined at the centre of a sphere uniformly charged: the presence of the charge on the sphere

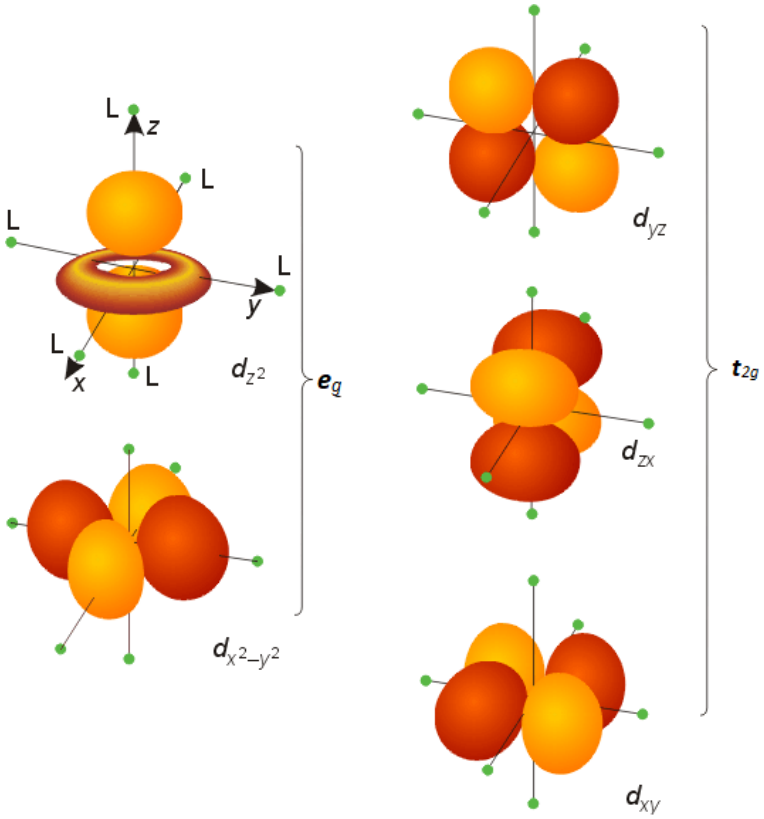

Figure 3.2: 3d orbitals for a transition metal ion, divided between e_g and t_{2g}. The L letters indicate the ligands at the corner of the octahedron (octahedral symmetry).

can interact equally with all the *5d* orbitals, so the energy of the system will rise while the orbitals will be degenerate.

Now, the the effect of the atomic arrangement on the total ion energy can be understood by imagining the same charge as before collected into six discrete point charges, each lying at the vertexes of an octahedron, but still on the surface of the sphere. The total electron energy of the d orbitals will not change, but the d orbitals will no longer be degenerate: using Fig. 3.2 as reference, the 4 atoms lying in the xy plane will interact more with the e_g orbitals, and less with the t_{2g} orbitals, so the first will become higher in energy, and the latter lower [16].

Other symmetries

If the local environment is something other than octahedrally symmetric, the crystal field may even work in the opposite sense. For example, in a tetrahedral environment the e_g orbitals are the ones that maximally avoid the charge density associated with the atoms, so they become the lower in energy, and the t_{2g} orbitals

become the higher.

The distortion of the octahedral coordination along one of the axes lowers the symmetry of the lattice, which goes from octahedral to tetragonal. In this environment, the energy levels are further split: the e_g level splits into the a_{1t} and b_{1t} levels, and the t_{2g} level splits into the 2-fold degenerate e_t level and the b_{2t} level. This axial distortion of the crystal field gives rise to the axial magnetic anisotropy for the paramagnetic center, which is essentially absent in the case of the ideal octahedron (see section 3.4.1). Further reduction of coordination along another axis can lower even more the crystal symmetry, splitting also the degeneracy of the e_t level. The effects of the octahedral and and tetragonal symmetry are represented in Fig. 3.3.

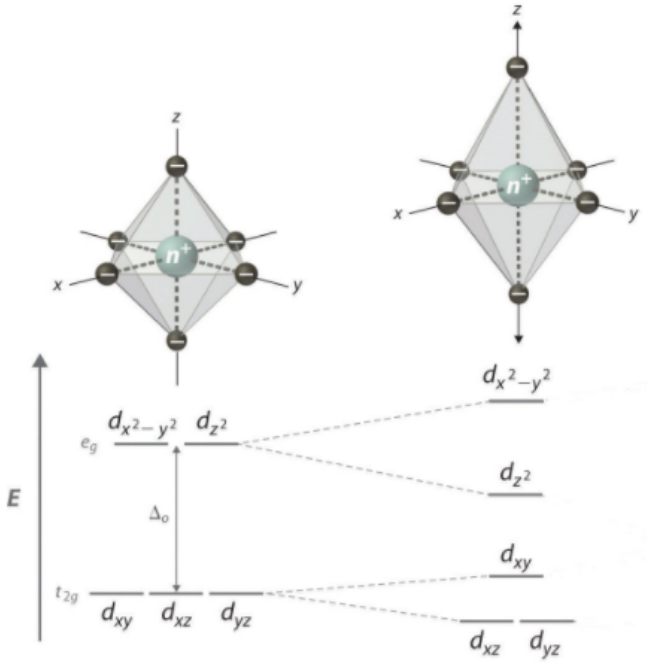

Figure 3.3: Energy splitting for an octahedral and a tetragonal environment. The energy levels of the orbitals in the tetragonal environment can be labelled, from bottom to top, e_t, b_{2t}, b_{1t}, b_{2t}.

3.3.2 Orbital Quenching

Using Hund's rules, one can predict the expected effective magnetic moment of a free ion using the formula

$$\mu_{eff} = \mu_B g_J \sqrt{J(J+1)} \tag{3.18}$$

where g_J is the Landé factor (see Eq. 3.12) and J is the predicted value of the total magnetic moment.

However, when comparing the computed values to experimental data, the result is that, for transition metal ions, the expected values are almost always overestimated. For example, Ni^{2+}, with $3d^8$ configuration, possesses the quantum numbers $S = 1$ and $L = 3$. According to Hund's rules, as it has a shell that is more than half-filled, its total angular momentum has quantum number $J = L + S = 4$. From this, using Eq. 3.18, the result is $\mu_{eff} = 5.6\mu_B$. This is quite different from the experimental value, usually about $3.1\mu_B$, which instead is in much better agreement with an effective magnetic moment of the form

$$\mu_{eff} = \mu_B g_e \sqrt{S(S+1)} \tag{3.19}$$

which gives the value of $2.8\mu_B$.

The effect underlying this discrepancy is known as *quenching of the orbital angular momentum*. This is due to the crystal field being of greater importance than the spin-orbit coupling, as 3d ions have orbitals easily interacting with neighbouring electrons. For *4f* ions, like rare earths, the orbitals are much less extended away from the nucleus and lie beneath the *5s* and *5p* shells so that the crystal field terms are much less important and Hund's third rule is obeyed.

The origin of the quenching effect can be deduced from the crystal-field hamiltonian. The crystal field in an octahedral environment is given by a constant plus a term proprtional to $x^4 + y^4 + z^4 - \frac{3}{5}r^4 + \mathcal{O}(\frac{r^6}{a^6})$, and is therefore a real function. The related hamiltonian term will thus have real eigenfunctions and eigenvalues. As seen in section 3.3.1, the presence of the crystal field removes the energy degeneracy of the orbitals, so the ground state can be supposed to be non-degenerate, and being an eigenfunction of the crystal field hamiltonian, can be expressed as a real function. The angular momentum operator $\hat{L}$ is Hermitian and therefore it has real eigenvalues, but the operator itself is purely imaginary ($\hat{\mathbf{L}} = -i\hat{\mathbf{r}} \times \boldsymbol{\nabla}\cdot$). Indicating the ground state as $|0\rangle$, the value $\langle 0|\, \hat{L}\, |0\rangle$ must be both purely imaginary, as the operator $\hat{L}$ is, and purely real, because the operator is also hermitian. To satisfy these conditions, it must be that

$$\langle 0|\, \hat{L}\, |0\rangle = 0 \tag{3.20}$$

so that all components of the angular momentum are quenched [16].

3.3.3 Anisotropic g-factor

In a real life scenario, the spin-orbit interaction is never completely negligible, and can be reintroduced as a perturbation of the hamiltonian. In this case, it can mix

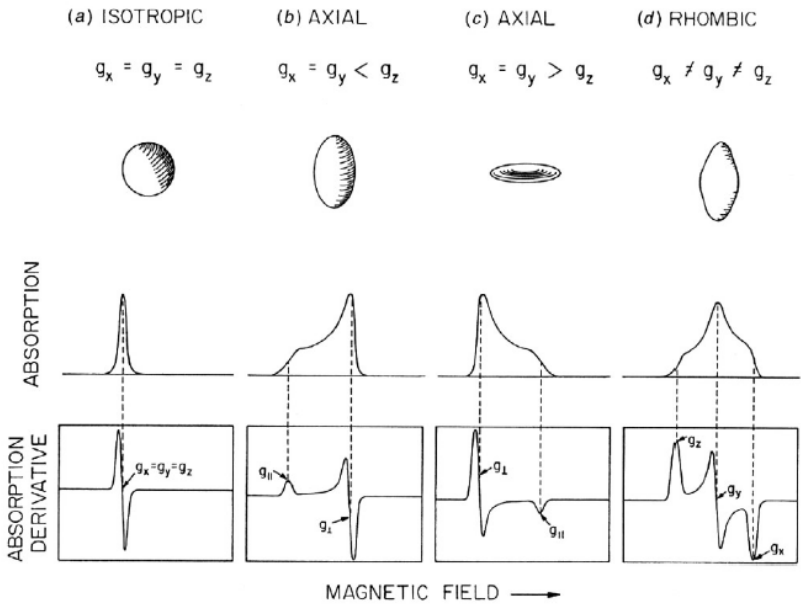

Figure 3.4: Schematic representation of g tensor and consequent EPR spectra for a fixed powder. The symmetry of the system are: isotropic (a), axial (b, c) and orthorombic (d).

the ground state with excited states, which have non-zero angular momentum. This results in a quenched ground state, but with a g-factor different from the spin-only value of 2 and slightly anisotropic. In this situation, the g-factor can be described by a tensor of the form $\mathbf{g} = g_e\mathbf{1} - 2\lambda\mathbf{\Lambda}$, where $\mathbf{\Lambda}$ is a symmetric tensor of the form

$$\Lambda_{ij} = \sum_{n\neq 0} \frac{\langle 0|\, \hat{L}_i \,|n\rangle \langle n|\, \hat{L}_j \,|0\rangle}{E_n - E_0} \tag{3.21}$$

where $|n\rangle$ is the n^{th} excited state and E_n and E_0 are the energies of the excited and ground states, respectively [17].

Usually, the g tensor principal axes frame is considered as the crystal field frame, and all interaction tensors are referred to this frame. Therefore three main cases for the values of g along the principal axes can be described: for cubic symmetry, with $g_x = g_y = g_z$, the axial symmetry, with $g_x = g_y \neq g_z$, and orthorombic symmetry, with $g_x \neq g_y \neq g_z$. The possible cases are represented in Fig. 3.4 [18].

3.4 Effective Hamiltonian

As seen in the previous section, there are various effects which can influence the resonance of a paramagnetic center. In order to simplify the classification of the obtained experimental results, various spectroscopies adopt the spin-Hamiltonian approach. This consists in replacing the orbital coordinates needed to describe the system with spin coordinates (S_x, S_y, S_z), using the symmetry properties of the system [17]. With regards to EPR spectroscopy, this approach is used to describe systems within the ground state, considering an effective spin S: in this situation, the hamiltonian can be divided in four main terms:

$$\mathcal{H} = \mathcal{H}_Z + \mathcal{H}_{ZFS} + \mathcal{H}_{EC} + \mathcal{H}_{HI} \tag{3.22}$$

where $\mathcal{H}$ is the Zeeman term, which describes the interaction with an external magnetic field, $\mathcal{H}_{ZFS}$ is the Zero Field Splitting, an intrinsic splitting of the energy levels caused by the crystal field, $\mathcal{H}_{EC}$ is the exchange interaction between paramagnetic centers, and $\mathcal{H}_{HI}$ is the hyperfine interaction between the electronic spin S and the nuclear isospin I.

In the next section, the first three terms and their effect on the EPR spectra will be described. The hyperfine interaction is usually too weak to be detected by EPR at High Field and High Frequency, and will thus be neglected. The spin $\vec{S}$ will be considered an operator vector, with each of the three components being the usual spin operator.

3.4.1 Zeeman Term and Zero Field Splitting

The simple hamiltonian for a free electron interacting with an external field contains only the Zeeman term, and it is of the form

$$\mathcal{H} = g_e \mu_B \vec{B} \cdot \vec{S} \tag{3.23}$$

as already seen in section 3.1. For an ion with more than one electron encased in a molecule, however, the interactions are more complex: spin-orbit coupling and the crystal field both give their contribution to the energy of the system. Including this effects, the Zeeman term becomes of the form

$$\mathcal{H}_Z = \mu_B \; g_e \; \vec{B} \cdot \vec{S} - \mu_B \; \vec{B} \cdot (2\lambda \; \mathbf{\Lambda}) \cdot \vec{S} \tag{3.24}$$

where $\mathcal{L}\dashv\Updownarrow\lfloor\lceil\dashv$ is defined by equation 3.21. By introducing the g-tensor $\mathbf{g} = g_e\mathbf{1} - 2\lambda\mathbf{\Lambda}$, the terms pertaining the interaction with the external field are usually written together as

$$\mathcal{H}_Z = \mu_B \vec{B} \cdot \mathbf{g} \cdot \vec{S} \tag{3.25}$$

with the g-factor depending on the direction of the applied field.

In order to describe the effect of the crystal field, a phenomenological term must be added to the hamiltonian. This splits the degeneracy of the energy levels for systems with $S > \frac{1}{2}$, even in the absence of the external field. This Zero Field Splitting term is of the form

$$\mathcal{H}_{ZFS} = \vec{S} \cdot \mathbf{D} \cdot \vec{S} \tag{3.26}$$

The D tensor is diagonal in the crystal field coordinate system, therefore equation 3.26 can be written as

$$\mathcal{H}_{ZFS} = D_{xx} S_x^2 + D_{yy} S_y^2 + D_{zz} S_z^2 \tag{3.27}$$

At this point, by defining the axial and transverse anisotropy parameters, $D = D_{zz} - D_{xx}/2 - D_{yy}/2$ and $E = D_{xx}/2 - D_{yy}/2$, respectively, the hamiltonian can be transformed to

$$\mathcal{H}_{ZFS} = D S_z^2 + E\left(S_x^2 - S_y^2\right) \tag{3.28}$$

and, by subtracting the constant $S(S+1)/3$, the hamiltonian becomes

$$\mathcal{H}_{\mathrm{ZFS}} = D\left[S_z^2 - \frac{S(S+1)}{3}\right] + E\left(S_x^2 - S_y^2\right) \tag{3.29}$$

which is the usually employed form, as it is traceless and easier to solve. The effect of this hamiltonian is a splitting of the energy levels even in the absence of an external field, as anticipated, and D and E are usually referred to as the axial and planar anisotropy term, respectively.

For example, in the octahedral symmetry, $D_{xx} = D_{yy} = D_{zz}$, so both D and E are equal to 0, meaning the hamiltonian is null too and the effect is not present. For a tetragonal symmetry, $D_{xx} = D_{yy} \neq D_{zz}$, so $E = 0$ and the effect can be described using only the axial anisotropy D.

As an example of the effect of the ZFS term on EPR results, the case of a Ni^{2+} in a tetragonal symmetry will be analyzed. This ion has a $3d^8$ configuration, with two unpaired electrons in the e_g orbitals, so it has a total spin $S = 1$. Considering an external field applied along the anisotropy axis z ($\vec{B}^T = (0, 0, B)$), the effective hamiltonian of its interaction with the paramagnetic ion is of the form

$$\mathcal{H} = \mathcal{H}_z + \mathcal{H}_{\mathrm{ZFS}} = \mu_B \; g_z \; B S_z + D\left[S_z^2 - \frac{S(S+1)}{3}\right] \tag{3.30}$$

The eigenstates of this hamiltonian are the pure states $|-1\rangle$, $|0\rangle$, $|+1\rangle$, which correspond to the possible values of the z-component of the spin. The eigenvalues

of the hamiltonian on this states are

$$E_0 = -2\frac{D}{3} \quad E_{\pm 1} = \pm g_z \mu_B B + \frac{D}{3} \tag{3.31}$$

It is thus possible to draw the dependance of the energy levels upon the magnetic field, as in the case with a free electron. The allowed transitions (with $\Delta m_S = \pm 1$) are $|-1\rangle \leftrightarrows |0\rangle$ and $|0\rangle \leftrightarrows |+1\rangle$, which have a different resonant condition (3.5), and so show up as different absorption lines in an EPR spectra. The two resonances differ in that one of them is related to a transition from the ground state, while the other transition is from an excited state: according to Boltzmann equation 3.6, the first transition will have a higher probability than the second, so its absorption line will have a higher amplitude than the second. The lowest energy level is decided by the sign of the axial anisotropy parameter D. In the case of $D < 0$ ("easy axis"), the lowest state in zero field is $E_{\pm 1}$, which is bi-stable, while for $D > 0$ ("easy plane"), the lowest state in zero field is the singlet E_0. For the easy axis case, the stronger absorption line shows up in the lower field, while for the easy plane scenario, the strongest line is the one in higher field. The energy levels and absorption spectra for the $D < 0$ case are reported in Fig. 3.5a.

For EPR results analysis, it is useful to make a plot of the frequency of the wave employed versus the field at which the absorption is registered. This type of plot for the case of $D < 0$ is reported in Fig. 3.5b. The lines present in this plot are called resonance branches, have a slope proportional to the g-factor in the direction of the applied field, and are associated with the two possible transitions. The change in the sign of the second line happens at the field where the energy levels E_0 and E_1 intersect in the energy level graph. The intersection of the upper line with the y-axis at zero field is associated to the anisotropy energy gap Δ, which is proportional to the D parameter as

$$\Delta = |D|\,(S^2 - (S-1)^2). \tag{3.32}$$

When the magnetic field is applied along a direction z' different from the anisotropy axis z, the hamiltonian can be given as

$$\mathcal{H} = \mu_B \; g_{z'} \; B S_{z'} + D\left[S_z^2 - \frac{S(S+1)}{3}\right] \tag{3.33}$$

In this case, the energy states can be found via diagonalization of the hamiltonian matrix given below (tab. 3.1). The different element of the matrix are computed by scalar product between the different pure states: for example, the $(-1,-1)$

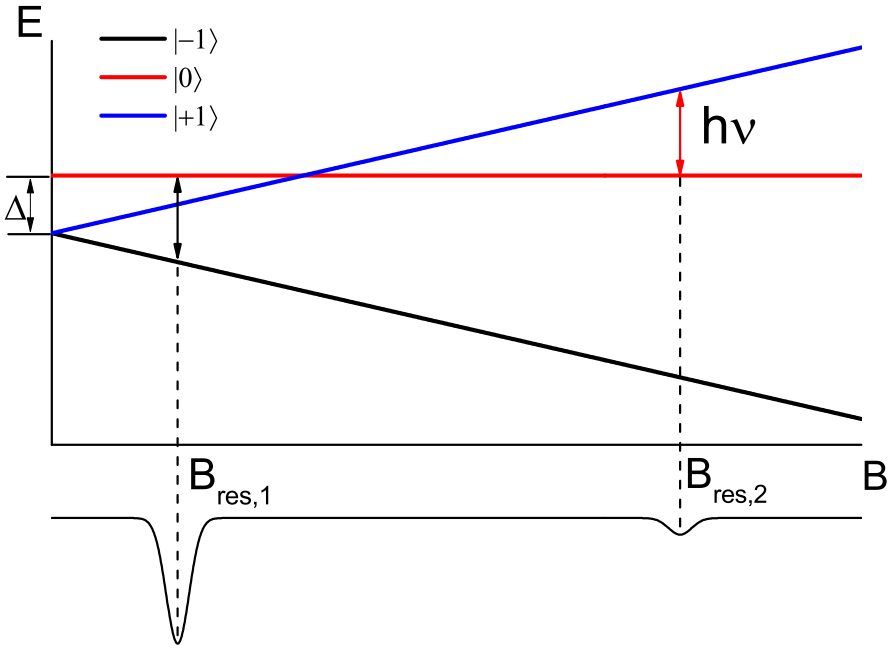

(a) Energy levels graph. The black arrow indicates the stronger allowed transition, the red arrow the weaker.

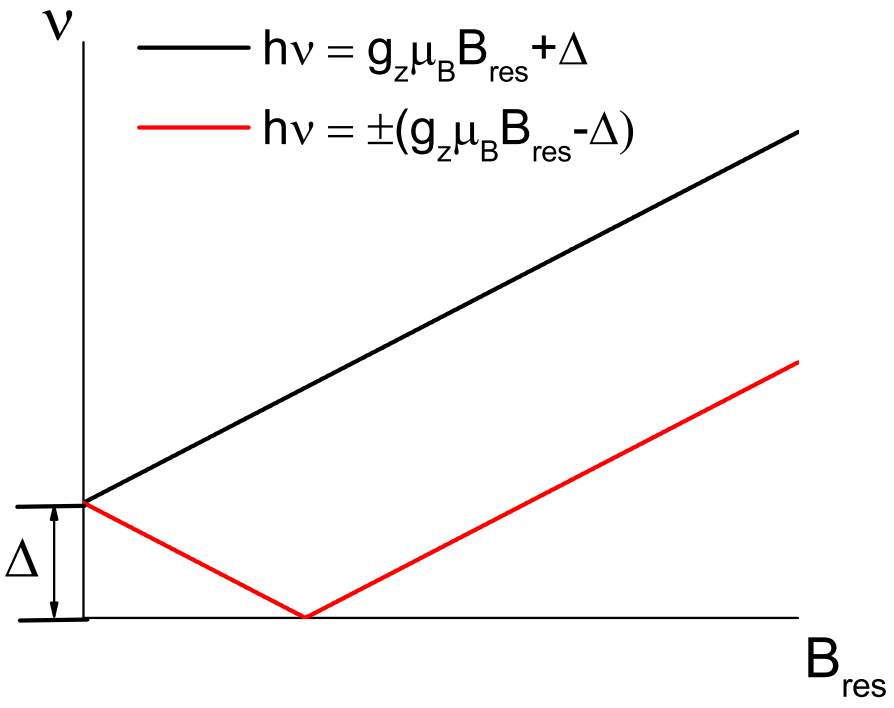

(b) Frequency vs resonance magnetic field graph, $\nu(B_{res})$, for the two allowed transitions.

Figure 3.5: Ni^{2+} paramagnetic centre in a tetragonal field schematics, with $D < 0$.

$S_{z'}$	-1	0	$+1$
-1	$\frac{1}{6}D(3\cos^2\theta - 1) - g\mu_B B$	$\frac{\sqrt{2}}{4}D\sin 2\theta$	$\frac{1}{2}D\sin^2\theta$
0	$\frac{\sqrt{2}}{4}D\sin 2\theta$	$-\frac{1}{3}D(3\cos^2\theta - 1)$	$-\frac{\sqrt{2}}{4}D\sin 2\theta$
$+1$	$\frac{1}{2}D\sin^2\theta$	$-\frac{\sqrt{2}}{4}D\sin 2\theta$	$\frac{1}{6}D(3\cos^2\theta - 1) + g\mu_B B$

(3.34)

Table 3.1: Hamiltonian matrix for a magnetic field tilted from the anisotropy axis direction [19].

element is derived as $\langle -1|\,\mathcal{H}\,|-1\rangle$. The angle θ is the angle between the magnetic field direction z' and the anisotropy axis z.

This matrix contains non diagonal elements which are not zero: this elements yield mixing of the energy states. In this situation, the eigenfunctions of the hamiltonian are not pure spin states as before, but are linear combinations of them. This means that there is a non-null probability of so-called forbidden transitions, with $\Delta m_S = \pm 2$. These transitions show themselves in the EPR spectrum as an absorption line with a slope double that of allowed transitions, $h\nu = \mu_B g'_z B|\Delta m_S| = \mu_B\ 2g'_z B$. The energy levels and spectra for a tilted magnetic field are reported in figure 3.6a, the resonant branches are reported in figure 3.6b. The different energy levels can no longer be linked to a specific pure state as before, as a consequence of the mixing. It is to be noted that the resonant branches in low field are curved lines, as a consequence of the angular dependance, while in higher field the spin aligns with the external magnetic field and the slope is again proportional to the g-factor.

3.4.2 Exchange Coupling Term

When dealing with multiple paramagnetic centers, the effective hamiltonian can be written as the sum of Zeeman and Zero-Field splitting terms for the different centers, but a new term must be introduced, which describes the possible interaction between them. This is usually called Exchange Coupling term, as it arises from the exchange interaction between the electrons of the different centers. This is usually an indirect interaction, i.e. it needs a non-magnetic mediator between the magnetic ions (for example, oxygen in oxides) [16]. The term in its most general

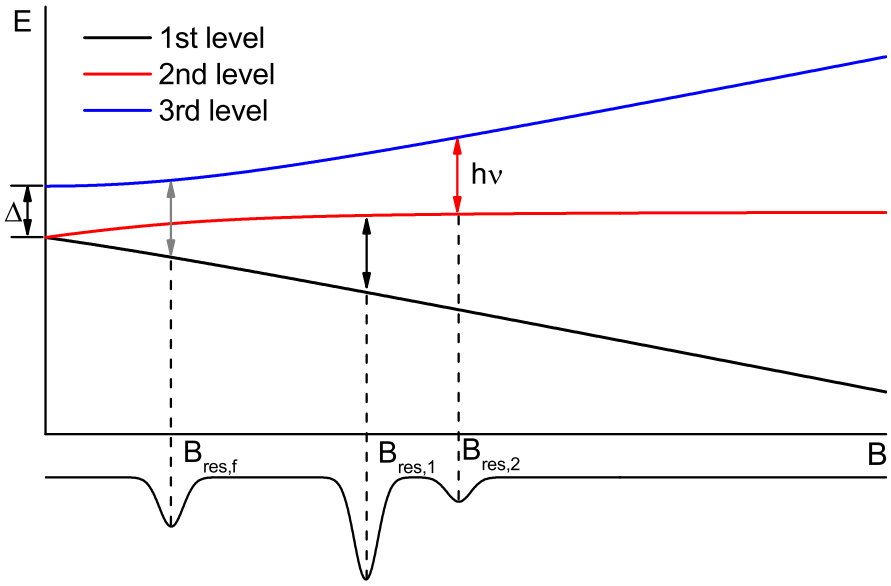

(a) Energy levels graph. The black and red arrows indicate the allowed transitions, the gray arrow indicates the "forbidden" transition.

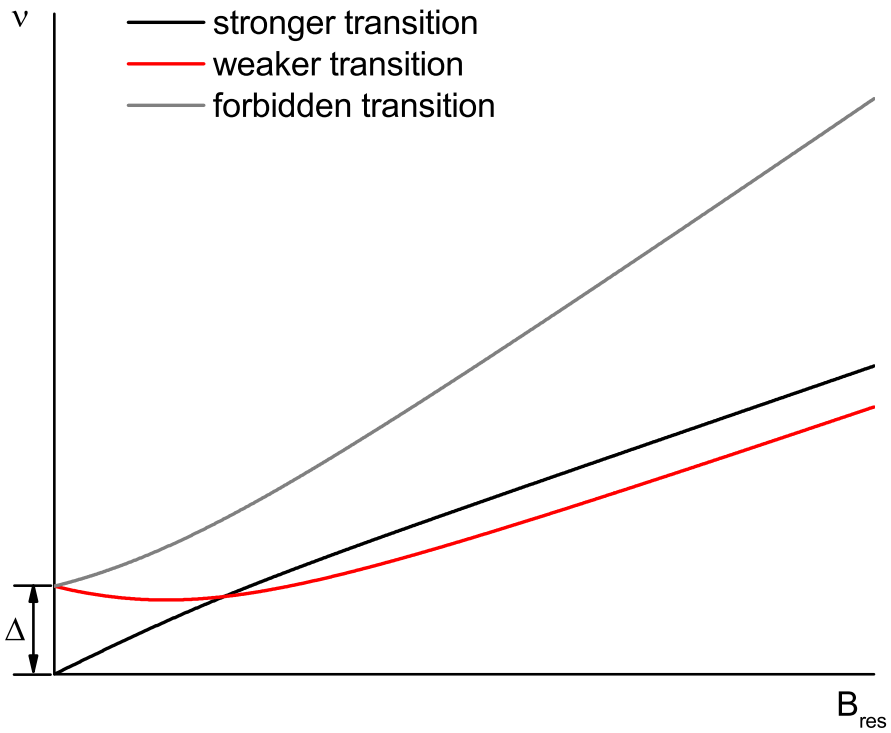

(b) Frequency vs resonance magnetic field graph, $\nu(B_{res})$, for the two allowed and one forbidden transitions.

Figure 3.6: Ni^{2+} paramagnetic centre in a tetragonal field schematics, with $D < 0$ and $\theta = 45°$.

form for two magnetic centers is

$$\mathcal{H}_{EC} = \vec{S_1} \cdot \mathbf{J}_{12} \cdot \vec{S_2} \tag{3.35}$$

where $\vec{S_1}$ and $\vec{S_2}$ are the spin operator vectors for the first and second centers, and $\mathbf{J}_{12}$ is a tensor describing all the possible interactions between the two. This tensor can be decomposed in three different contributions, each with its physical significance, and the term can be rewritten as

$$\mathcal{H}_{EC} = J_{12}\vec{S_1} \cdot \vec{S_2} + \vec{d_{12}} \cdot \vec{S_1} \times \vec{S_2} + \vec{S_1} \cdot \mathbf{D}_{12} \cdot \vec{S_2} \tag{3.36}$$

In this last equation, the first term is the isotropic (Heisenberg term), which minimizes energy in case of ferromagnetic ($J < 0$) or antiferromagnetic ($J > 0$) coupling: in the first scenario, it is energetically convenient for neighbouring spins to stay parallel to each other, in the second, to stay antiparallel. The second term is the antisymmetric contribution, which favours a 90° degree angle between the two spin vectors. The last term is the anisotropic contribution, which tends to keep the spins aligned along a given (by the tensor) orientation in space [20].

Usually, the first term can be considered dominant over the other two, which can be introduced as perturbations. If this condition is fulfilled, the total spin $\vec{S} = \vec{S_1} + \vec{S_2}$ eigenvalues remain good quantum numbers with possible values

$$|S_1 - S_2| \leq S \leq |S_1 + S_2| \tag{3.37}$$

Each of the values of S correspond to a spin multiplet with eigenvalues $-S, -S+1, \ldots, S-1, S$ and an energy of states of the form

$$E_S = \frac{1}{2}J_{12}[S(S+1) - S_1(S_1+1) - S_2(S_2+1)] \tag{3.38}$$

In figure Fig. 3.7 is reported an example for two Ni^{2+} ions in an octahedral environment ($D = E = 0$), with strong isotropic exchange coupling between each other. The effective hamiltonian of the system can be written in the form

$$\mathcal{H} = \mathcal{H}_{Z,1} + \mathcal{H}_{Z,2} + \mathcal{H}_{EC} = \mu_B g\vec{B} \cdot \vec{S_1} + \mu_B g\vec{B} \cdot \vec{S_2} + J_{12}\vec{S_1} \cdot \vec{S_2} \tag{3.39}$$

where $S_1 = S_2 = 1$. For a strong coupling (typically $J_{12}/h > 50GHz$), the different multiplets are far apart enough that the system can be described with the effective hamiltonian of a system with a single spin $\vec{S}$ with the same quantum number as the lowest multiplet, which is $S = 2$ for the ferromagnetic (FM) coupling, $S = 0$ (non magnetic) for the antiferromagnetic (AFM) coupling. For weaker coupling, the different multiplets are not easily distinguishable and the full hamiltonian must be employed.

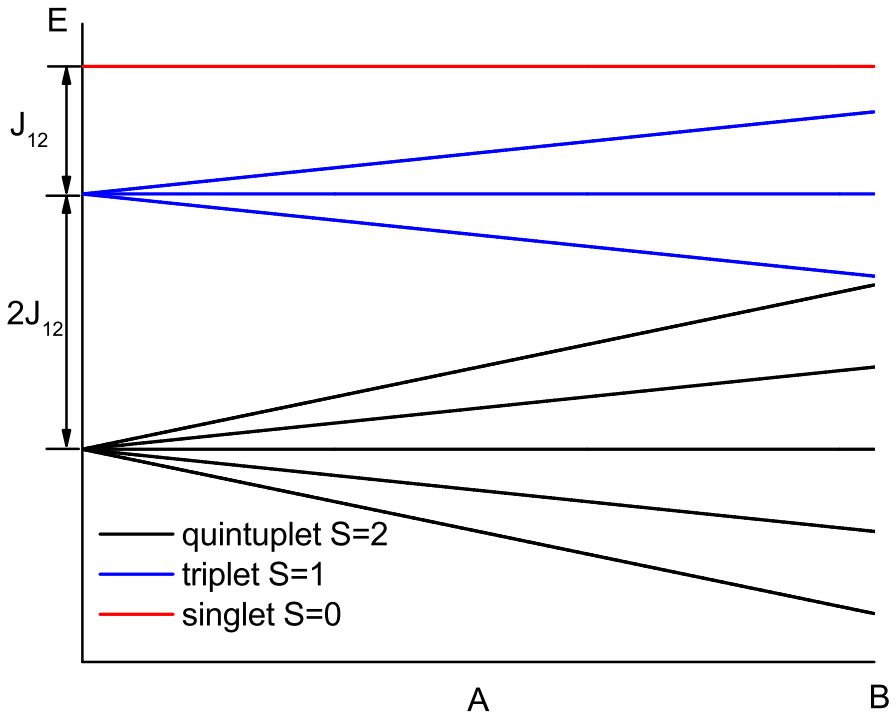

(a) Ferromagnetic coupling, $J < 0$.

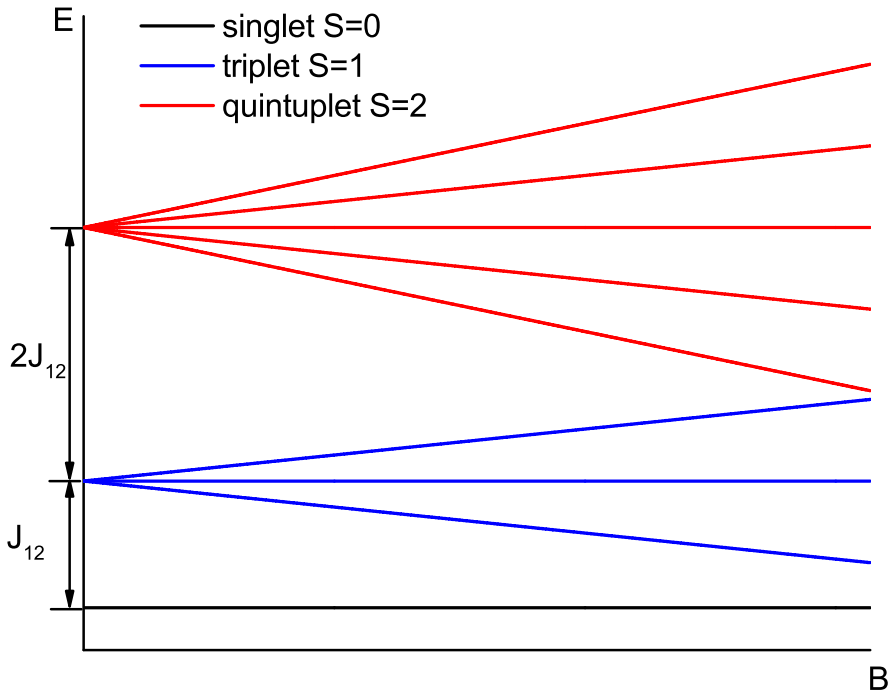

(b) Antiferromagnetic coupling, $J > 0$.

Figure 3.7: Energy levels for two Ni^{2+} in an octahedral environment, with strong Exchange Coupling. The Energy difference between the multiplets is computed from Eq. 3.38.

3.4.3 Full Hamiltonian Example

In real single molecular magnets, both the anisotropic crystal field and the exchange coupling are important factors in creating a paramagnetic center with large spin in the ground state, so both the Zero Field Splitting and the Exchange Coupling has to be taken in consideration for hamiltonians with more than one spin center. It is here reported the example of a spin system with two Ni^{2+} ions in the same tetragonal environment, with a $D < 0$ axial anisotropy along the z axis (in crystal field coordination), and a magnetic field pointing along the z direction, in the form $\vec{B} = (0, 0, B)$. The two ions are isotropically coupled with an antiferromagnetic coupling $J_{12} < 0$. The effective hamiltonian of this system is of the form

$$\mathcal{H} = \mu_B g_z B S_{1,z} + \mu_B g_z B S_{2,z} + \sum_{i=1,2} D \left[S_{i,z}^2 - \frac{S_i(S_i+1)}{3} \right] + J_{12} \vec{S_1} \cdot \vec{S_2} \qquad (3.40)$$

Where $\vec{S_1}$ and $\vec{S_2}$ are the spin operator vectors for the first and second Nickel ions, respectively. In Fig. 3.8 the energy levels of the system are reported for 2 particular scenarios. In the first one, the ferromagnetic coupling is taken to be very large, which means that the ground state spin multiplet is well isolated from excited states. In this case, this spin multiplet behaves like the energy levels of a spin $S = 2$ paramagnetic center, and can be studied with a single-spin effective spin hamiltonian (see for example Eq. 3.30). In the second one, the ferromagnetic coupling is instead very weak, so that the different multiplets are difficult to recognize, and the coupling acts more like a perturbation to the hamiltonian of two free paramagnetic centers. In this situation, a careful confrontation between observed and simulated resonant branches is necessary in order to estimate the parameters of the Hamiltonian.

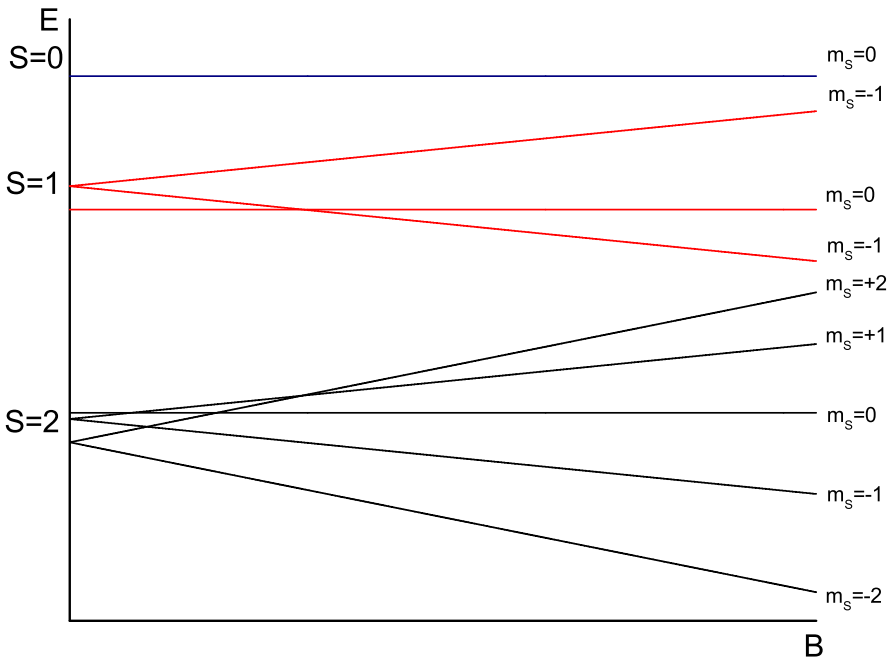

(a) Energy levels graph for a strong coupling scenario; the different spin multiplets are easily distinguishable.

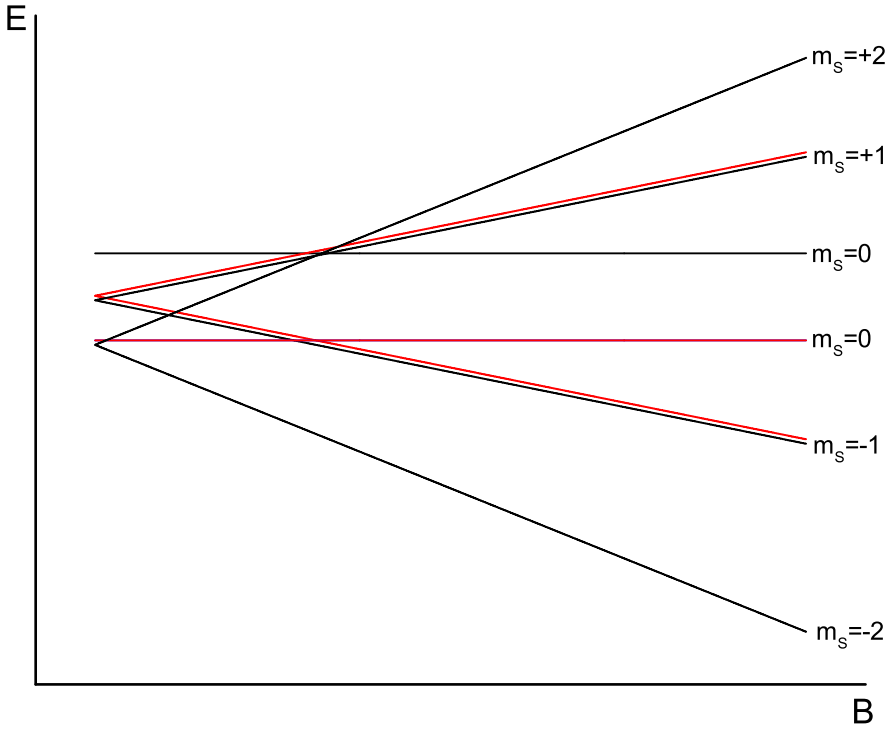

(b) Energy levels graph for a weak coupling scenario; the different multiplets are mixed and not easy to discern.

Figure 3.8: Energy levels simulation for two Ni^{2+} ions with an axial anisotropy parameter $D < 0$ and a coupling $J_{12} < 0$.

Chapter 4

Experimental Setup and Data Analysis

The data on which this thesis work is based were experimentally gathered by means of High-Frequency/High-Field Electron Spin Resonance (HF-ESR). The experimental and sample setup, as well as the software used for the analysis and simulation of results, will be described in the following chapter [21].

4.1 Electron Spin Resonance Spectroscopy Apparatus

The experimental apparatus for the High Field/High Frequency Electron Spin Resonance Spectroscopy (HF-ESR) is schematically represented in figure 4.1. The requirements of this kind of spectroscopy are high frequency microwaves, up to the order of the THz, high magnetic fields and very low temperatures. The instruments used to create the conditions necessary for the experimental procedure to successfully take place are described below.

The microwave electromagnetic radiation required for the spectroscopy is produced by a Millimeter Vector Network Analyzer (MVNA), which acts both as source and detector [22]. This device is produced by the company AB Millimetre [23]. It contains two YIG (Yttrium Iron Garnet) oscillators, which are continuously turnable in the range of 8 to 18.5 GHz. These sources have an intrinsic stability that drifts by only a few MHz per hour when working around 100 GHz.

The two sources are phase locked to each other, and their absolute frequency is stabilized by phase locking them to an external frequency counter with an internal quartz reference (Phase matrix), to conterbalance the intrinsic drift in frequency. The High Frequency signal is subsequently generated through the use of Schottky

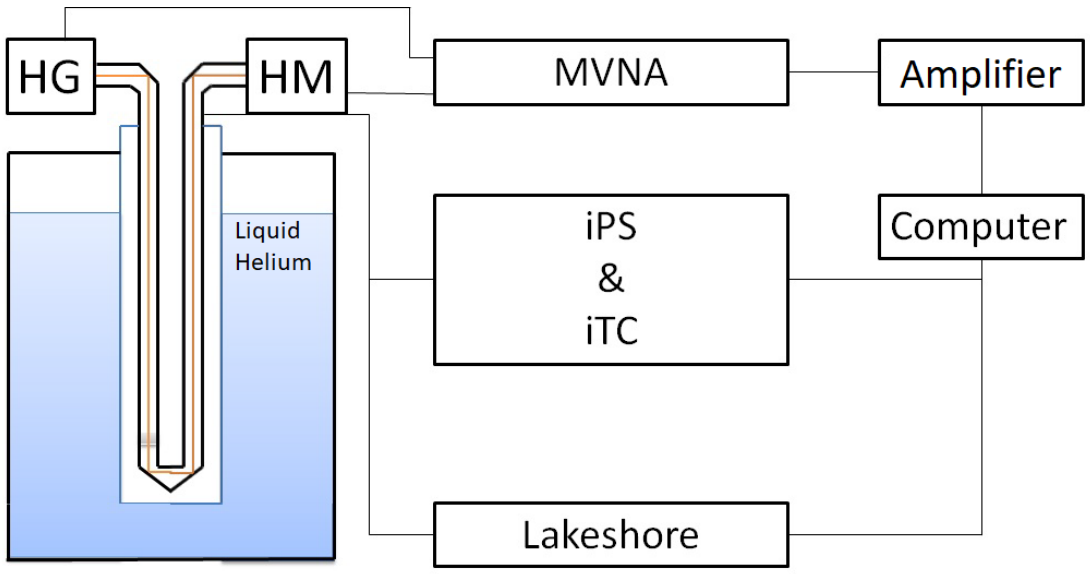

Figure 4.1: Apparatus schematics: through the MVNA the microwaves are generated, and the frequency is than amplified thorugh the Harmonic Generator HG and Harmonic Mixer HM. The resulting transmission signal is than measured by a computer. The control units iPS, iTC and Lakeshore control the magnetic field and temperature.

diodes, through which the frequency domain is extended from 8 GHz up to 1200 GHz.

The first source generates a signal at frequency $F1$ which is brought, through a coaxial cable, to the Harmonic Generator HG (a Schottky diode multiplier), where it is multiplied by the harmonic number N.

The signal is then conducted to the sample chamberr through a wave-guide. The chamber is made in such a way as to maximize the coupling between the microwave field and the sample itself.

The resulting frequency ($N \times F1$) is reflected back up a parallel waveguide to the Harmonic Mixer HM (a second Schottky diode), where it is mixed with the second frequency from 'Source 2' ($N \times F2$). This allows to produce a signal with a beat frequency $F = N(F1 - F2)$ suitable for detection and analysis. The transmission signal is than measured by a phase-sensible Lock-in amplifier, and registered in a computer measuring both the amplitude and the phase of the signal.

The magnetic field is generated by a semiconductor magnet with a standard homogeneity at 16/18 T, in an Oxford cryostat. The cooling of the samples, necessary to reach low temperatures and thus to analyze the ground state of the

paramagnetic centers, is made using liquid helium. The temperature domain can be varied in the range $2 - 300K$ by the use of a variable temperature inset (VTI). The temperature of the chamber is than kept under control by a Mercury iTC, while the sample temperature is automatically regulated by a Lakeshore 340 TC.

To allow the interaction between the microwaves and the samples, a reflecting pole with circular waveguides, upholstered with gold, is used. The samples are mounted at the end of the pole, centered in the homogeneous magnetic field. Helium is used as an exchange gas, to allow thermal exchange between the VTI and the sample pole.

(a) The MVCA apparatus, with an oscilloscope to control the signal.

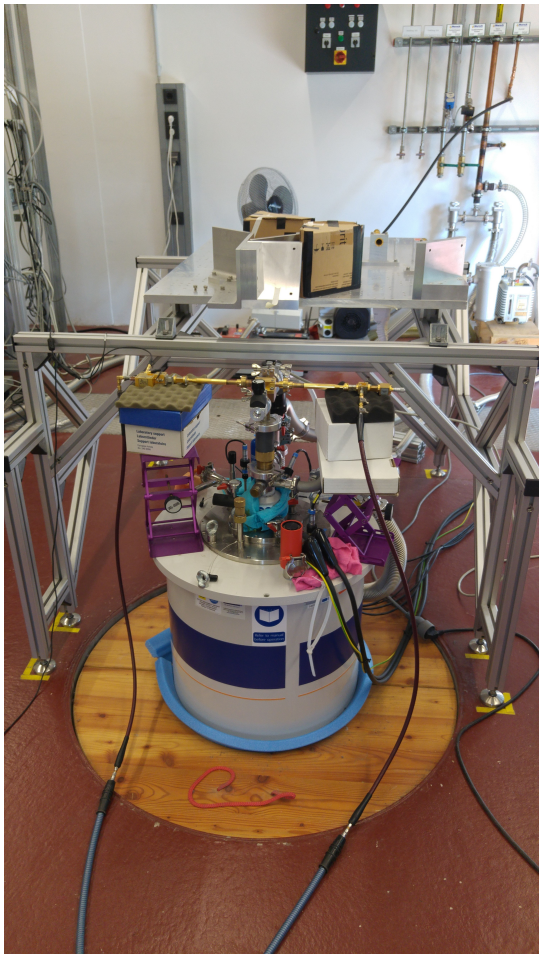

(b) The sample probe, with attached dyodes (HG and HM), inserted in the helium tank.

Figure 4.2: Microwave generation apparatus and sample setup.

Figure 4.3: The iPS, iTC and Lakeshore for temperature and magnetic field control

During a spectrum acquisition, first the desired frequency is selected through the MVNA, than it is kept constant while the magnetic field is swept with a maximum sweep speed of $1T/min$.

4.2 Sample preparation

In samples analyzed in this work were small quantity of powders, usually referred to as loose powders, of crystalline metal-organic materials. The usage of a loose powder allows reorientation of the micro-crystals in response to the magnetic field. The samples where thus kept in containers where the powder was free to rotate, namely small cylinders of Polyether-ether-ketone (PEEK). The other advantage of this type of container is that it also fits the SQUID magnetometer used in magnetization measurements by the research group [21]. The containers were fixed in the cavity by the use of Capton tape, and all the support structure was than enclosed in teflon tape to be more stable. Both Capton and teflon tape show no interaction with Electromagnetic fields.

4.3 Phase and background correction

The HF-ESR transmission spectra obtained in this setup are usually subject to a background signal caused by thermal fluctuations, or by a phase contribution due to little phase differences in the microwaves. By mixing the registered transmission amplitude with the phase the position and shape of the resonance features can be modified, in order to reproduce the pure transmission spectra. This is referred to as phase correction. The correction is achieved thorough the linear combination

$$T_{corr} = T_0 + \alpha\phi \tag{4.1}$$

with $|\alpha| < 0.1$, typically. Here T_0 stands for the transmission signal intensity, while *phi* stands for the phase signal intensity. The ambiguity of this correction is reflected in the errors attributed to the resonant magnetic fields of the registered absorption features.

4.4 Software employed

The software used for spectra recording and analysis, for phase correction, for peak positions identification and linear fitting, is the data analysis and graphing program OriginPro [24]. The hamiltonian construction and energy levels, as well as resonant branches simulations, where done by means of the EasySpin toolbox for Matlab [25].

Chapter 5

Sample Characterization

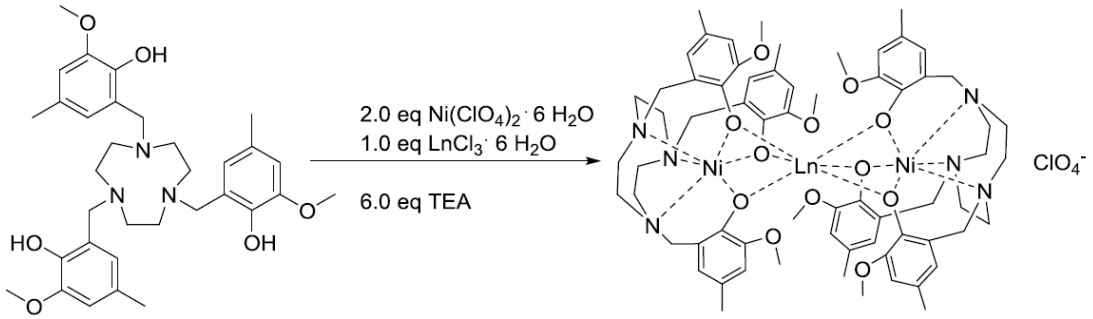

Figure 5.1: Schematics of the reaction that combines the L^{tacn} group (on the right) with the paramagnetic Ni and Ln ions in order to form the final compound (on the left) [26].

The complexes analyzed are two heterotrinuclear metalorganic compounds, synthesized during the PhD work of Michael Großhauser [26]. The first one, $[La(III)Ni(II)(L^{tacn})_2]ClO_4$ (tacn=trisazacyclononan) (see Fig. 5.1), from now referred to as $Ni(II)_2La(III)$ or Ni_2La to evidence the nature of the paramagnetic centers, contains the ion La^{3+}, which has no unpaired electrons and, thus, no paramagnetic behaviour: in this way, only the behaviour of the two Nickel ions can be taken into consideration in studying the data. The second compound, similar to the first, is $[Ho(III)Ni(II)(L^{tacn})_2]ClO_4$, where La^{3+} is substituted by Ho^{3+}. Ho^{3+} has a free ion total angular momentum of $J = 8$, so in this case the spin of the lanthanide must be taken into consideration in the study of the complex. The experimental idea was to gather hamiltonian parameters from the study and simulation of the data of the two compounds, and, by confronting them, to underline how much of a difference the insertion of different Lanthanide ions has on the Ni

anisotropy, and define the possibility of observing exchange coupling from the EPR data of this kind of complexes.

In the following chapter are reported the molecular and crystal structure of the compounds. All the informations concerning the molecular structure and orientation of the compounds were obtained by Prof. Wadepohl through X-Ray diffractometry.

5.1 Ni_2La

The sample under analysis was in powder form. The powder was stored inside a PEEK cylindrical container, which could be easily inserted inside the EPR sample probe.

The single molecule of this compound is reported in Fig. 5.2. As can be seen, the three paramagnetic centers are disposed in an almost straight line, with the two Nichel atoms surrounding the Lanthanium. The angle formed by the three centers is of 174.3°. The Ni(II) atoms are three times coordinated with nitrogen atoms, and three times coordinated with oxygen atoms. The 6 atoms surrounding Ni(II) form an octahedral coordination. The oxygen atoms connect Ni(II) with La(III). The latter is coordinated 6 times with the 6 oxygen atoms, and its coordination polyhedr can be described with a triangular prism.

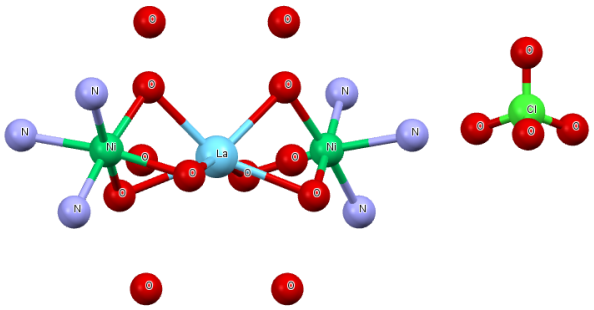

Figure 5.2: Molecular structure of the Ni_2La complex. Hydrogen and Carbon atoms are omitted for simplicity.

The crystal cell of this complex does not contain only one molecule. The compound is made in such a way as to present four different molecules inside the lattice unit. The cell is reported in Fig. 5.3. The space group of the crystal is Pnna, so it is Orthorombic, and the single cell is a parallelepiped with lattice parameters $a = 12.9$ Å, $b = 25.6$ Åand $c = 23.0$ Å, with angles $\alpha = \beta = \gamma = 90°$.

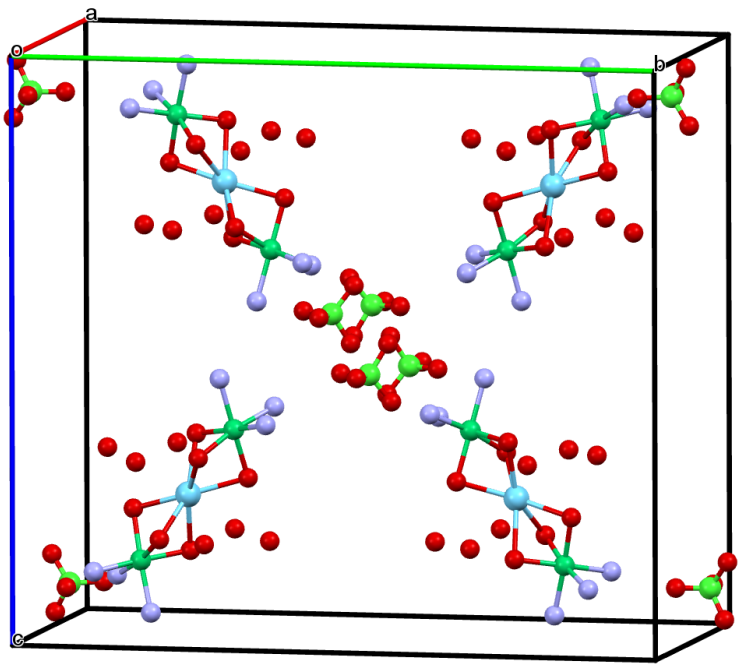

Figure 5.3: Crystal unit cell of the Ni_2La complex. Hydrogen and Carbon atoms are omitted for clarity.

5.2 Ni_2Ho

The Ni_2Ho sample was again in the form of powder, stored inside a PEEK cylindrical container.

The single molecule of this compound is reported in Fig. 5.4. As it can be seen, the structure is very similar to the one of Ni_2La, with the three paramagnetic centers disposed in an almost straight line, the two Nickel atoms at the two sides of Holmium. The angle formed by the three centers is of 178.8°. The Ni(II) coordination is very similar to Ni_2La, too, with the 3 nitrogen and 3 oxygen atoms disposed around it in an octahedron. Ho(III) is 6 times coordinated with the 6 oxygen atoms, and its coordination polyhedr can be described with a triangular prism.

The packing of the crystal shows again the presence of four different molecules in the reticule unit, as reported in figure 5.5. The space group of the crystal is P 2_1/n, so it is monoclinic, and the single cell is a parallelepiped with lattice parameters $a = 12.9$ Å, $b = 22.4$ Åand $c = 23.0$ Å, with angles $\alpha = \gamma = 90°$, $\beta = 93°$.

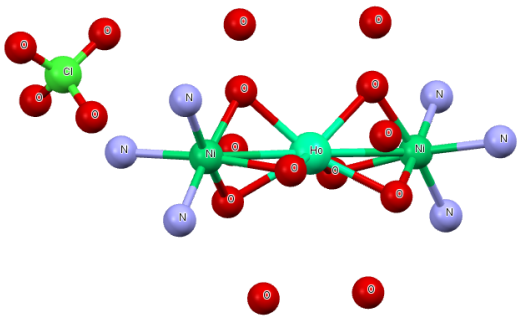

Figure 5.4: Molecular structure of the Ni_2Ho complex. Hydrogen and Carbon atoms are omitted for simplicity.

5.3 Molecular orientation problem

From the crystallographic layout of the two compounds, it is clear that the single cell of both complexes did not contain only one molecule, but four, which contained in total 8 paramagnetic centers. From the analysis of molecular data, performed by Dennis Müller [27][28], the four molecules show two different orientations, with two pair of molecules always pointing in the same direction (viewed from the c axis). The four molecules can thus be viewed as two pairs connected by a rotational symmetry and, by the magnetic point of view, only one pair needs to be considered. The two molecules in one pair are tilted, one from the other, of an angle of 71.4°. The two molecular axes, i.e., the axes connecting the first and second Nickel atoms, are also twisted of an angle of 13.6°. These two angles are reported in Fig. 5.6. Holmium shows a similar structure, with the two angles being 75.3° and 30.8°, respectively.

Information about the magnetic moments orientation of the ions in a similar Ni_2Dy sample was also gathered by Dennis Müller, leading to the two Nickel ions having a 36° angle between one another (see Fig. 6.8a). As the molecular coordination of the Nickel ions is the same in the three compounds, and being them almost perfect enantiomers, the magnetic structure can be assumed to be the same, and so the same 36° angle between the magnetic moments will be considered for the present study of the Ni_2La and Ni_2Ho samples. The presence of two different spin orientations for each canted molecule rendered necessary the consideration, when simulating the system hamiltonian, of four different Ni(II) paramagnetic centers.

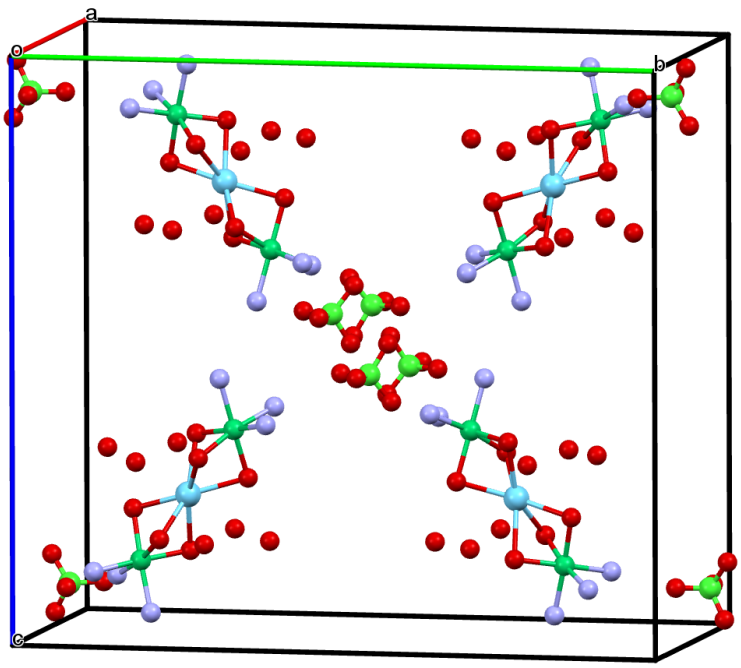

Figure 5.5: Crystal unit cell of the Ni_2Ho complex. Hydrogen and Carbon atoms are omitted for clarity.

5.4 Dy_2Ni

As a final mention, during this thesis also gathered hamiltonian information from a $[Dy(hfac)_{32}\text{-}Ni(dpk)_2(py)_2]$ (Hdpk = di-2-pyridyl ketoxime) compounds compound, taken from literature [9], and referred to as $[Dy_2Ni]$. The chemical structure of this compound, already shown in chapter 2, is reported in Fig. 5.7. This sample was used in order to gather information about a way of introducing the high-spin ground state of the Holmium ion inside the second sample hamiltonian, and than the energy levels of the complex were simulated and confronted with the original compound in order to test the goodness of the added hamiltonian terms.

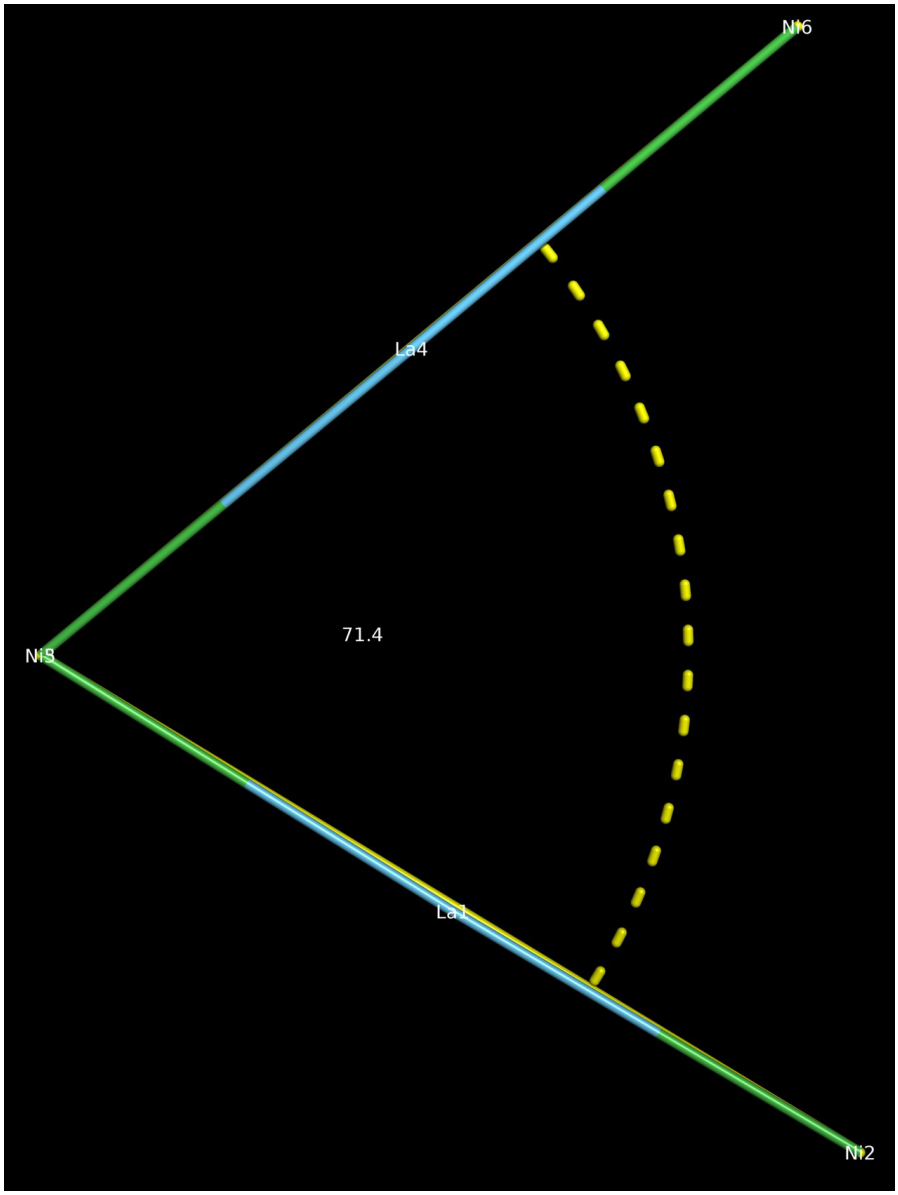

(a) Molecular axis separation of 71.4 degrees between the two main molecules in Ni_2La.

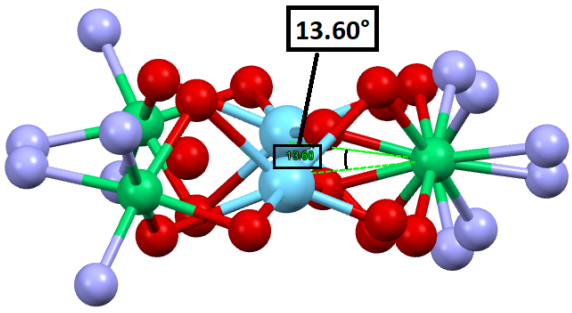

(b) Torsion between the first and second molecule

Figure 5.6: Main separation angles between the molecular axis.

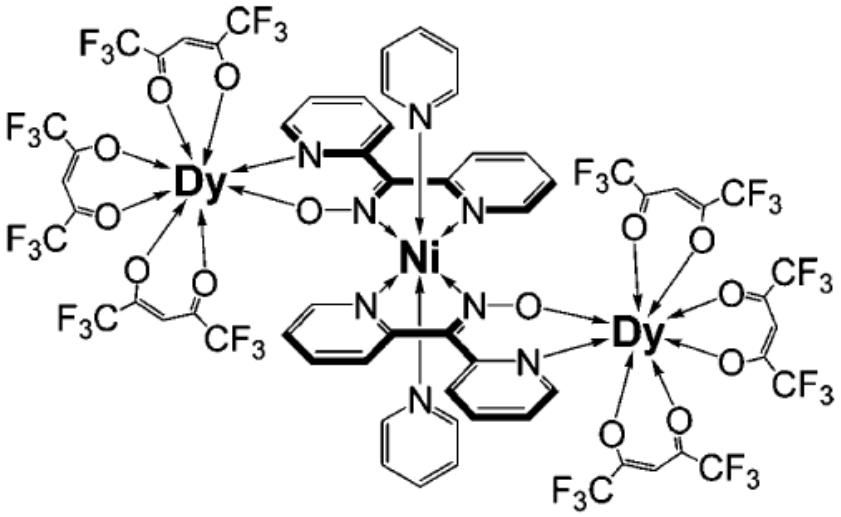

Figure 5.7: Chemical structure of the [Dy_2Ni] compound used for the Holmium hamiltonian building.

Chapter 6

Results and analysis

In this chapter, the experimental data acquired are reported, and their analysis is discussed.

The properties of these two compounds are investigated by means of HF-EPR spectroscopy, in a frequency range spacing from 50 GHz to 450 GHz, with the magnetic field ranging from 0 to 16 T.

6.1 Ni_2La

This section will discuss in detail the analysis and the results for the Ni_2La sample.

6.1.1 HF-EPR data

The first task carried out in order to study the sample was to perform HF-EPR spectroscopy at very low temperatures, so that the ground state of the system could be well isolated. In order to find the best temperature at which to acquire data, two sample spectra were taken at 208.0 GHz and at 180.1 GHz. The second one was chosen to perform a temperature-dependant acquisition, from 2 to 15 K.

The temperature-dependant acquisition was performed in order to check if more features would show up when increasing the temperature. In fact, as the sample contains only two Nichel ions as paramagnetic centers, there was the possibility of observing some of the weaker high (or low) field transitions due to the easy axis (or plane) anisotropy, D (see section 3.4.1). Considering for example two energy levels separated by an energy of $E/h = 150$ GHz, the temperature necessary for thermal fluctuations to populate the upper level is $T = E/k_B = 7$ K, and after being thermally populated this can also resonate with the incoming wave to give a new feature, activated by the temperature.

The acquired spectra are shown in Fig. 6.1. The vertical position of the spectra

was arbitrary chosen and doesn't carry any physical meaning, as the transmission is reported in arbitrary units. As the magnetic field produced by the apparatus goes up to 16 T at a rate of 1 T/min and then has to return down to 0 T at the same speed, two spectra are acquired by the software connected with the MVNA apparatus, one during the up-sweep and one during the down-sweep, both of which were used for the data analysis. The spectra depicted in this thesis, when it is not explicitly specified otherwise, are the ones taken during the down-sweep. All depicted spectra have already been corrected by background subtraction and phase correction (see section 4.3).

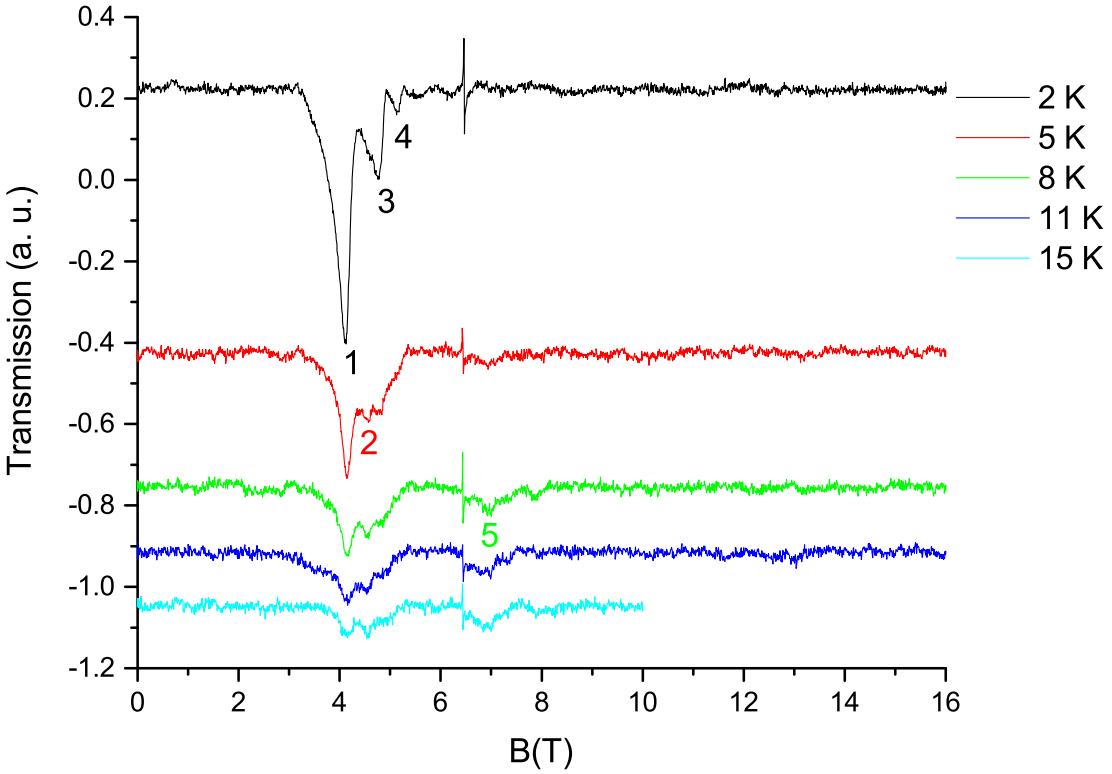

Figure 6.1: Temperature dependance of Ni_2La, from 2 to 15 K, at a frequency $\nu = 180.1$ GHz.

At the temperature of 2 K, there are three main features to be noted: one at around 4.1 T (Feature 1), the second at around 4.8 T (Feature 3), and the third at around 5.1 T (Feature 4). The sharp peak at 6.5 T is attributed to a resonance of a free radical inside the PEEK container (see Appendix A). As the temperature goes up, the intensity of the main features decreases, as expected for transitions from the lowest energy level. Moreover, new features seem to arise at around 4.6 T (Feature 2), in between the first two, and at around 6.9 T (Feature 5), with

a spectral weight increasing with temperature, as expected for transitions from higher energy levels, populated by thermal fluctuations. In order to better analyze the behaviour of all the transitions, the temperature of 8 K was chosen for the acquisition of frequency dependant data.

The frequency dependant spectra obtained for this sample are reported in Fig. 6.2, along with the frequency of acquisition. Frequencies below 98.7 GHz are not reported, as the resonance signal was not observable anymore. All the features that have been reported for $T = 8$ K, $\nu = 180.1$ GHz can be observed at almost all the frequencies, apart from the lowest or highest ones where the experimental noise covers the less prominent resonances.

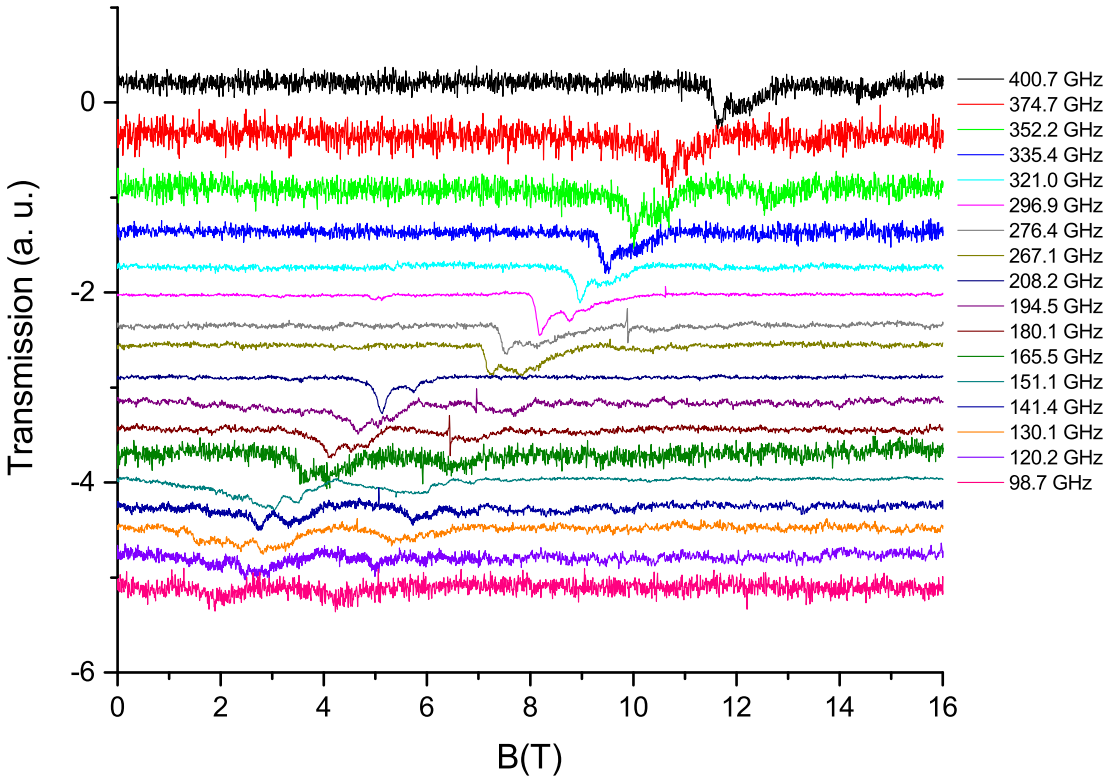

Figure 6.2: Transmission spectra for the Ni_2La sample for various frequencies between ∼90-400 GHz. The presence of 5 main features can be recognized.

In order to study the resonant branches, and obtain from them informations about the system parameters, the field-position of each resonance feature must be recorded and then reported in a frequency *vs.* resonance-field graph. The position of the peak in the graph was identified using the Origin program, and attributed a systematic error which took into consideration the difficulty of identifying the exact position of the peak due to broadening or phase mixing. This operation

was performed both for up-sweep and down-sweep spectra, and afterwards the weighted mean between the two was computed. The resulting graph is reported in figure 6.3.

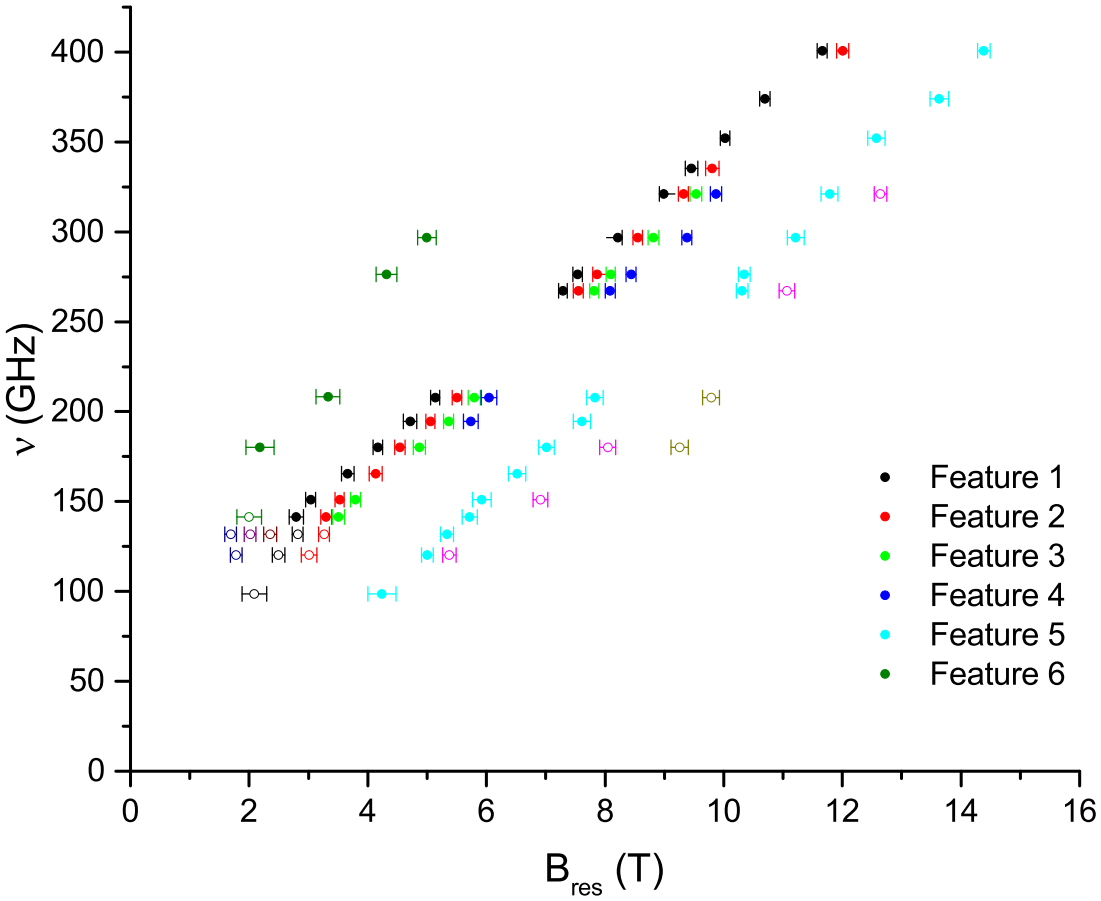

Figure 6.3: Resonant features obtained for Ni_2La. The plain dots represent the features that linearly follow the ones observed at 180.1 GHz, the empty ones represent the features that were unexpected or non-linear in respect to the behaviour observed at the other frequencies.

In graph 6.3, six main spectral features can be identified. These features were first examined using the temperature-dependant acquisition in Fig. 6.1, through which each feature was assigned a number for easier identification.

Feature 1 is the leftmost one and it has the most spectral weight at all frequencies. Feature 2 is the feature arising with temperature in between Feature 1 and Feature 3, and at 8 K is the second feature for spectral weight. Feature 3 has lower spectral weight than Feature 2 at 8 K, and Feature 4 is the weaker one. This feature tends to disappear at higher temperatures, so it does not always appear in

the spectra in Fig. 6.2. At higher frequencies, due to the increase in the harmonic numbers required to achieve them, more noise is present in the spectra, so the features become less and less recognizable, as well. Feature 5 is the second feature arising with temperature at around 8 K, beside the PEEK container signal, with a lower spectral weight than the other features. Feature 6 is a very weak resonance clearly identified only at 4 frequencies, at lower field than all the others.

Apart from these main trackable features, other resonances are reported in the graph as empty dots. The features at higher field than feature 5 were very weak, they only appeared at a couple different frequencies and couldn't be ascribed to linear behaviour. At the frequency of 130.1 GHz, three more features appeared at lower resonant field than feature 1, and could be partially recognized at lower frequencies. Moreover, the spectra seemed to suggest a non linear behaviour of the main features at low frequency. This unaccounted behaviours will be adressed after the simulation of the resonance branches through effective spin hamiltonian.

In order to start gathering some rough information about the system under study, a linear fitting of the main features was carried out. This fit can give starting informations both about the axial anisotropy parameter D (see Eq. 3.32) and about the g-factor (see Eq. 3.5) of the Nickel ions. In Figure 6.4 the fitting lines for features 1, 2, 3, 4, 5, 6 are reported. This fit left out on purpose the empty dotted data, for which resonance behaviour hints to non linearity. This analysis was performed using the Origin program, by means of weighted fits which took into consideration the x-error attributed to the resonant field of the data. Errors along the y-axis, which could only be caused by the intrinsic error of the MVNA apparatus, where neglected for the purpose of this analysis. The intercepts and slopes obtained from the fit, as well as the respective errors, are reported in table 6.1.

The intercept values can be used to get a rough idea about the absolute value of the Zero Field Splitting parameter D, and so about the anisotropy of the Nickel ions in the system, and the negative value of the intercept of the line of Feature 5 suggests that this is not a ground state transition, as seen in chapter 3.

The slope of the lines can give information about the g-factor of the Nickel ions: in fact, from the resonance equation 3.5, one can obtain

$$\nu = \frac{\mu_B}{h} g B_{res} \tag{6.1}$$

so that the g-factor can be obtained from the linear slope by dividing it by $\mu_B/h \sim 14.00$. The results in the table are already in the most suitable form and, being all compatible, suggest a value of the g-factor of around 2.1. This is different and non-compatible with $g_e = 2$, as expected from section 3.3.3. The value of the slope

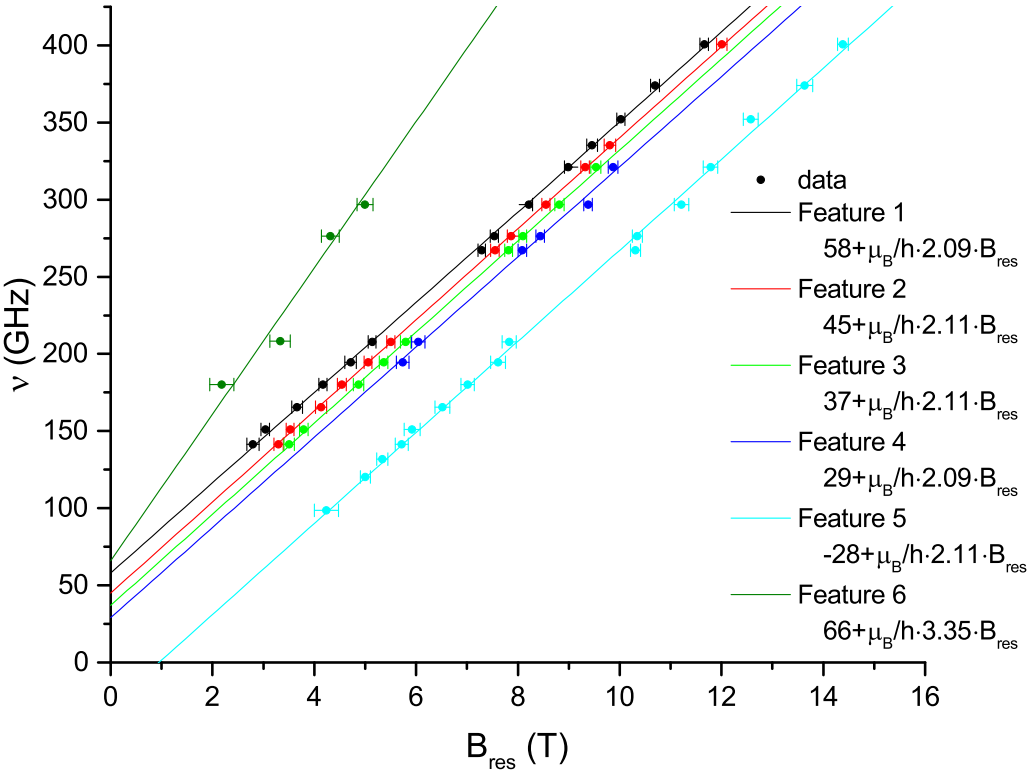

Figure 6.4: Ni_2La resonance features with linear behaviour and the respective fitting lines.

of the Feature 6 line is far greater than 2, suggesting a forbidden transition. The fact that the errors of line 4 and 6 are greater than the others is due to the poor amount of data points which could be used for the fitting.

The next step in the study of the sample was taking a more complete temperature-dependant acquisition of the spectrum, to have a more detailed idea about the resonance weight transfer. This was done after the frequency-dependant acquisition in order to detect the most suitable frequency for showing the behaviour of all the features. The frequency of 276.4 GHz was selected for this measurement, as it was one of the frequencies were, at 8 K, the features could be observed more clearly and with less amount of phase correction, especially the main one. The spectra resulting from this acquisition are reported in Fig. 6.5. The features which can be seen in the $T = 2K$ data are Feature 1 at $B_{res} \sim 7.5T$, Feature 3 at $B_{res} \sim 8.1T$, and Feature 4 at $B_{res} \sim 8.4T$.

The temperature dependance spectra acquired are not as good as the previous ones at $\nu = 180GHz$. The data show again the rising of a new feature, previously labelled Feature 2, at $B_{res} = 7.8T$ for $T = 6K$, which becomes evident for $T = 8K$

	Slope	**Intercept**
Feature 1	$\frac{\mu_B}{h}(2.09 \pm 0.02)$	58 ± 2 GHz
Feature 2	$\frac{\mu_B}{h}(2.11 \pm 0.02)$	45 ± 2 GHz
Feature 3	$\frac{\mu_B}{h}(2.11 \pm 0.03)$	37 ± 3 GHz
Feature 4	$\frac{\mu_B}{h}(2.09 \pm 0.09)$	29 ± 11 GHz
Feature 5	$\frac{\mu_B}{h}(2.11 \pm 0.03)$	-28 ± 3 GHz
Feature 6	$\frac{\mu_B}{h}(3.35 \pm 0.47)$	66 ± 27 GHz

Table 6.1: Slope and intercepts obtined from the linear fitting of the different features in Ni_2La, with the respective errors.

(signaled by black arrows in the graph). Moreover, as soon as the temperature rises from 2 K, Feature 4 tends again to disappear. However, the high field feature (Feature 5) is in this case very subtle, and in most spectra it's barely noticeable.

In order to have a more complete set of data, another temperature-dependant acquisition was taken, to better follow the behaviour of the resonance features at higher temperature. Before doing so, the sample probe was opened and some of the sample powder was removed from inside it. This was done both to guarantee a better coupling of the powder with the microwave field inside the chamber, and to test the aligned-powder hypothesis. If too much powder is inserted inside the probe, its space could be reduced to the point that it goes from being a loose powder sample to a packed powder sample, and could show a powder-spectra even in the presence of easy axis crystal field anisotropy, not having space to self-align along the magnetic field direction.

After the sample was inserted back inside the probe, a new temperature dependance acquisition was taken, at the same frequency $\nu = 276.4GHz$. Fig. 6.6 reports a comparison between the $T = 2K$ spectra for the two cases, the original one and the one with less powder. As can be seen from the graph, the second acquisition shows much better absorption, which translates in higher spectra weight of the resonance features, and the main features become more evident. This gives credit to the hypothesis that all three features come from a preferred orientation of the powder sample. For the sample with less powder, the present of the reso-

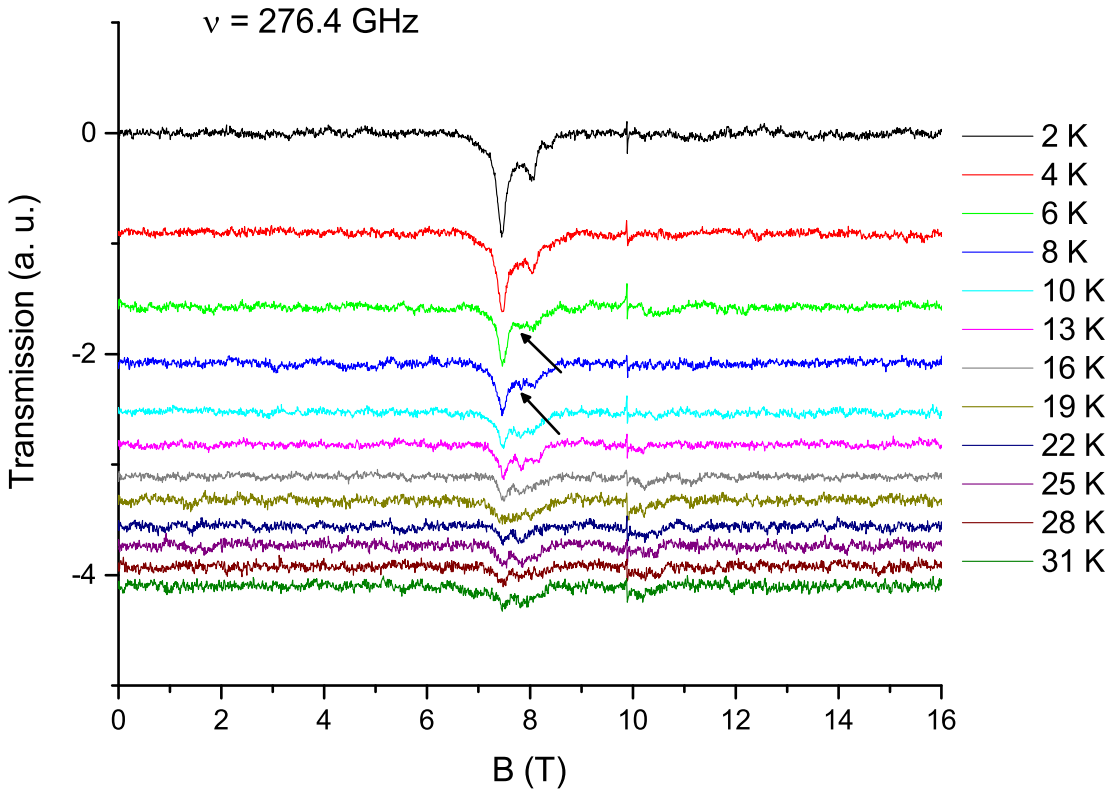

Figure 6.5: Ni_2La temperature dependance at $\nu = 276.4GHz$. The black arrows signals the rising of Feature 2 between Feature 1 and 3.

nance referred to as Feature 6 is also evident. The results for the new temperature dependant acquisition are reported in Fig. 6.7.

This new acquisition confirms all the previous information: feature 1, 3, 4 and 6 are transitions from the lowest energy level, while features 2 and 5 only arise at higher temperatures, and their spectral weight increases with respect to the others, suggesting transitions from an excited state. The fact that the spectral weight of the system transfers from lower to higher fields by increasing the temperature hints to the negative sign of the D parameter, and so to an easy axis anisotropy. This means that, for the spin, it is energetically preferable to stay along the z-axis of the crystal field, and this axial anisotropy can lead to the self-aligning of the powder grains along the magnetic field. The alignment of the powder is suggested also from the proximity of Feature 1, 2 and 4 at 2 K, which are all found in an interval of $\sim 1\ T$, because powder spectra are usually more broadly distributed and present only one sharp peak in their spectra.With the information gathered, it is possible to try to build an hamiltonian to simulate the behaviour of the system.

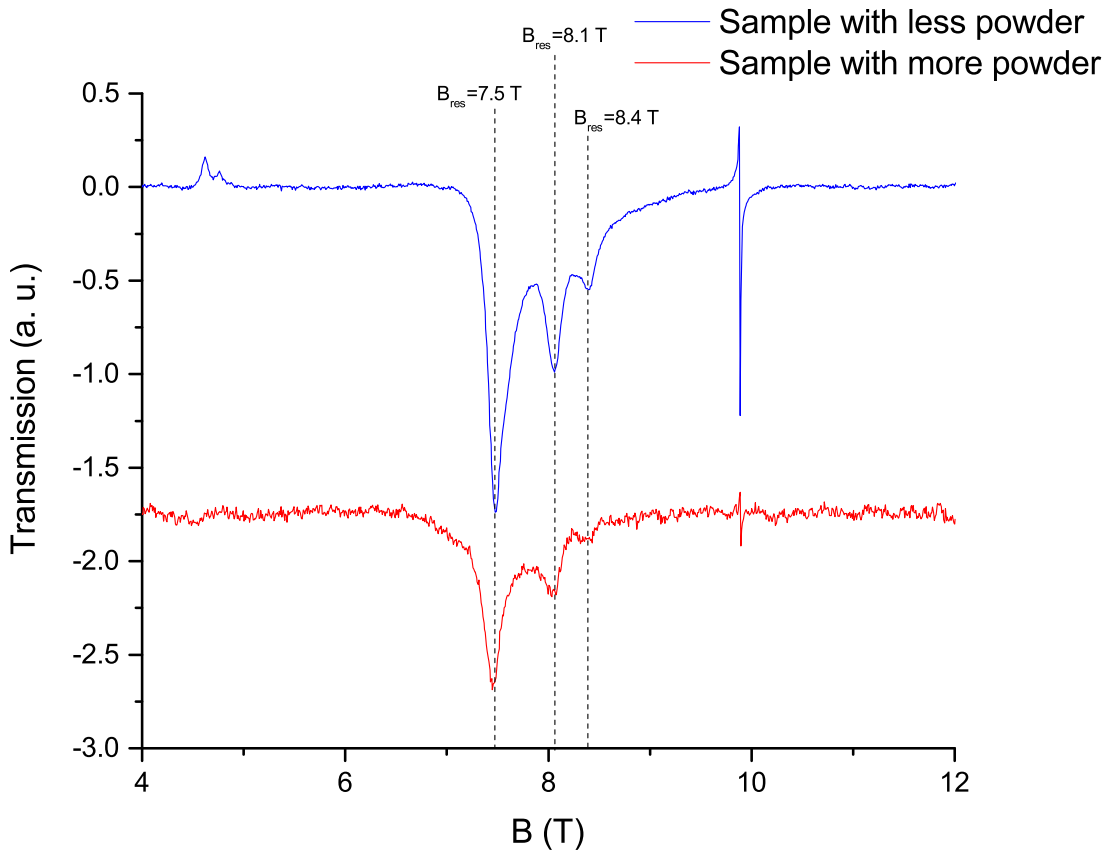

Figure 6.6: Comparison between the Ni_2La samples with more and less powder. The peak positions for the main resonant features are reported, and are the same for the two cases.

6.1.2 Simulation Work and Results

The main concern about the correct simulation of the system is the presence of three different features in the main orientation of the complex, one of them rising with temperature. As this can not be explained by considering only one of the crystal molecule orientations, the inclusion of all the four spin centers discussed in chapter 5 will be necessary. In order to simulate the behaviour of the system, an effective ground state spin hamiltonian must be built. As there are two canted molecules to consider, the system has been divided in two hamiltonians, one for each molecule, and the energy levels resulting from the two where simultaneously taken into consideration when looking for transitions compatible with the gathered data. A MATLAB script was written in order to produce rotation matrices which would describe the single spins' canting inside the molecules. The simulation considered the preferred orientation axis as passing in between the two molecules,

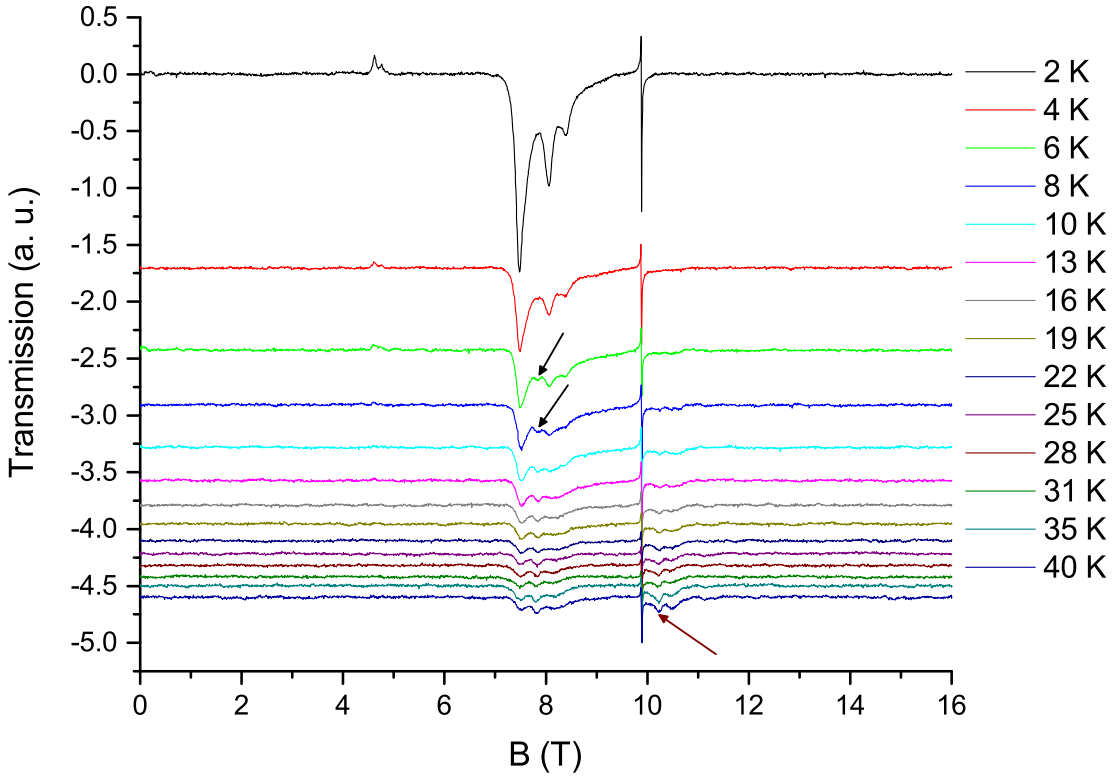

Figure 6.7: Temperature dependance for the Ni_2La sample with less powder. Black arrows indicate the rise of Feature 2 between $T = 6K$ and $T = 8K$. A brown arrow indicates the presence of Feature 5 at higher temperatures.

as to give all the spins the same weight in the self-orientation of the powder.

The script working process is summarized in Fig. 6.8b: the molecular reference frames are first twisted of an angle of 13.6°, than canted in order to have a 71.4° separation between the z-axis of each molecule. Their reference frame is than rotated around the axis according to the parameter β. This is due to the fact that the correct rotation angle of the magnetic structure in respect to the molecular one is not well known from the molecular structure data, so it has to be left as a free parameter. The two molecules are rotated one clockwise and the other one counter clockwise, in order to respect the symmetry of the system. Then each spin axis is tilted from the molecular one according to the parameter α, keeping an angle of 36° between the two spins in each molecule. The parameter values were inferred from the molecular and magnetic structure of the system, and then adjusted according to the confrontation between the simulation results and the gathered data.

The hamiltonian for each molecule should contain an anisotropic Zeeman Term,

(a) Magnetic structure of Ni_2Dy, which can be assumed to be the same as Ni_2La, apart from the fact that Lantanium has no net magnetic moment.

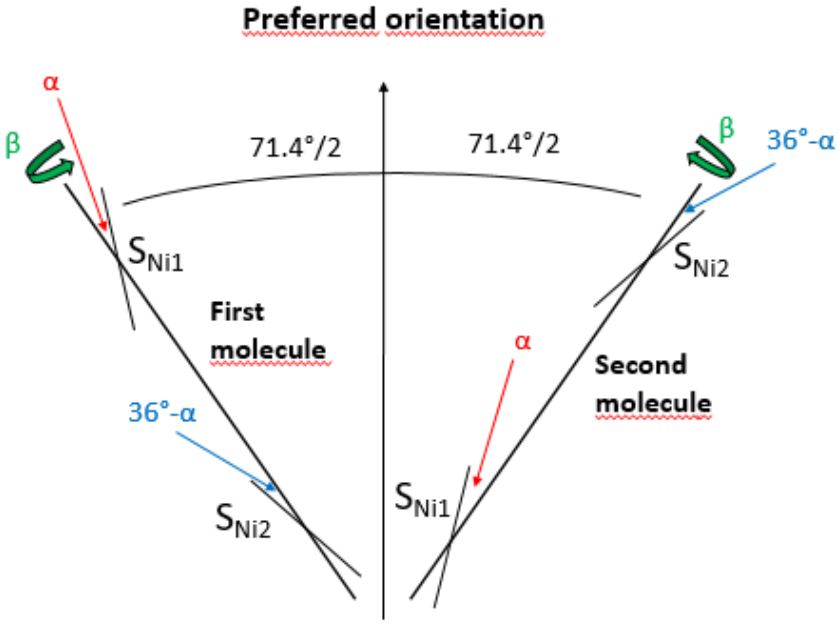

(b) Schematization of the angle parameters used for the simulation.

Figure 6.8: Angle information and parameters for the Ni_2Ln type compounds.

a Zero Field Splitting Term and an Exchange Coupling Term. ZFS is necessary to explain non-null intercepts for the linear fitting, and is connected to the presence of crystal field anisotropy. An anisotropic g-factor was also considered. A weak exchange coupling can split the different multiplets slightly enough to help explain the rise of a non-ground-state feature in the middle of ground-state ones.

The resulting hamiltonian, which takes the spin canting into consideration, is than of the form

$$\mathcal{H} = \sum_{i=1,2} \left(\mu_B \vec{B} \cdot \mathbf{R}_i^T \cdot \mathbf{g} \cdot \mathbf{R}_i \cdot \vec{S}_i + \vec{S}_i \cdot \mathbf{R}_i^T \cdot \mathbf{D} \cdot \mathbf{R}_i \cdot \vec{S}_i \right) + J \vec{S}_1 \cdot \vec{S}_2 \tag{6.2}$$

and, by considering $\vec{S}' = \mathbf{R} \cdot \vec{S}$, can be rewritten as

$$\mathcal{H} = \sum_{i=1,2} \left(\mu_B \vec{B} \cdot \mathbf{R}_i^T \cdot \mathbf{g} \cdot \mathbf{R}_i \cdot \vec{S}_i + D \left((S'_{i,z})^2 - \frac{S_i(S_i+1)}{3} \right) + \right.$$
$$\left. + E \left((S'_{i,x})^2 - (S'_{i,y})^2 \right) \right) + J \vec{S}_1 \cdot \vec{S}_2 \tag{6.3}$$

where the g-tensor is diagonal, of the form $\mathbf{g} = d(g_x, g_y, g_z)$. In this way, all the parameters describing the system are visible in the hamiltonian. The rotation matrices $\mathbf{R}_i$ are reference frame rotations which were built using the previously mentioned MATLAB script.

The simulated hamiltonian was diagonalized and solved, by means of the EasySpin program, obtaining the energy levels for each molecule. This energy levels where carefully analysed in order to find transitions that could best explain the observed resonance branches. Once the transitions were found, simulated resonant branches could be obtained from them: at this point, the reasonable parameters to describe the system where found by trial and error comparisons, starting from the free angle parameters, and then switching to the magnetic parameters of the hamiltonian. The final parameters are reported in table 6.2, where the errors are given by the maximum parameter range in which the simulation remains in good agreement with the data. The angles used are $\alpha = (22 \pm 1)^\circ$ and $\beta = (90 \pm 2)^\circ$.

The energy levels obtained for the two molecules are reported in Fig. 6.9, as well as the proposed transitions for a frequency of $\nu = 276.4 GHz$. Feature 1 can be explained by a transition from the first to the third energy level of either molecule 1 or 2, as the two resonant fields are very similar. Feature 3 is obtained as a transition, in the first molecule, from the first to the second energy level, while Feature 4 is the same transition, but for the second molecule. Feature 2 can be obtained, as initially hypothesized, only by using a weak ferromagnetic J parameter and thus with a weak ferromagnetic coupling, and can be best explained

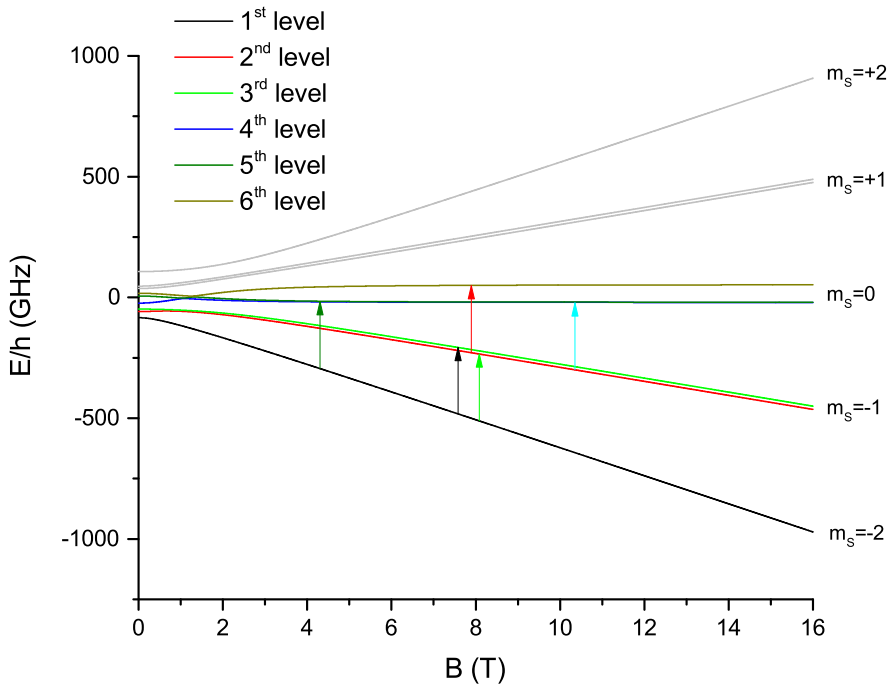

(a) Energy levels simulated for the first molecule. The transitions for Features 1, 2, 3, 5 and 6 can be observed.

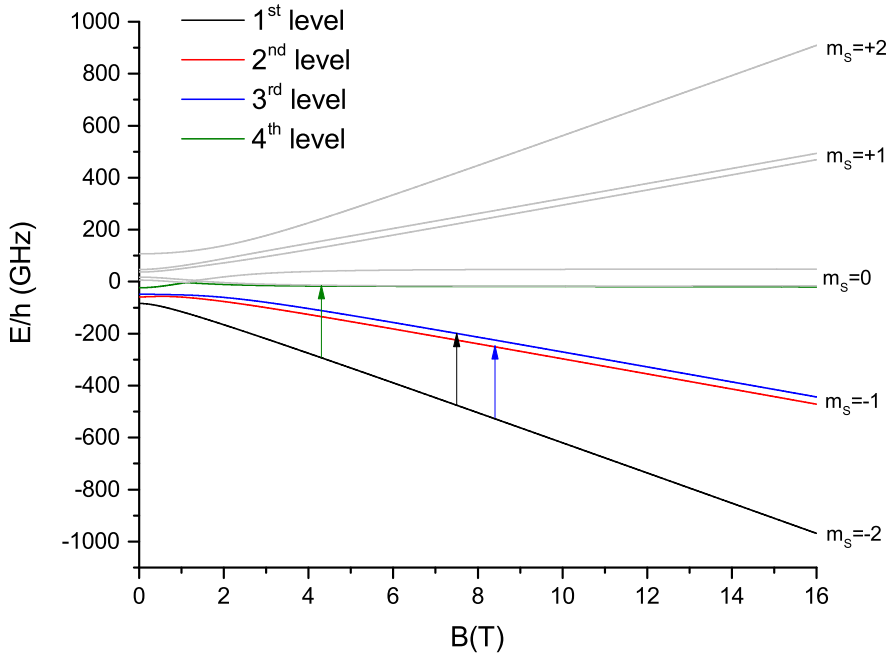

(b) Energy levels simulated for the second molecule. The transitions for Features 1, 4, 6 can be observed.

Figure 6.9: Energy levels simulated for the system. The color of the arrows is linked to the obtained resonance: black for Feature 1, red for Feature 2, light green for Feature 3, blue for Feature 4, light blue for Feature 5 and olive green for Feature 6.

Parameter	Value
$g_x = g_y$	2.04 ± 0.02
g_z	2.12 ± 0.01
$D/h(GHz)$	-80 ± 4
$E/h(GHz)$	15 ± 3
$J/h(GHz)$	-6 ± 1

Table 6.2: Hamiltonian paramters obtained from the simulation of the resonant branches of Ni_2La.

by a transition from the second to the sixth energy level. As expected, this is not a transition from the lowest energy level, and gets only activated once the second level gets populated enough from thermal fluctuations. This is also true for Feature 5, which can instead be best explained by a transition, in the first molecule, from the second to the third level. Finally, Feature 6 can be ascribed to a transition from the first to the fourth level both in the first and second molecules.

In Fig. 6.10 the resonant branches obtained from the simulation are reported. The resulting branches are in good agreement with data at high frequency, where they follow smoothly the observed resonances.

At lower frequencies, the situation gets mixed up: the resonant branches come very close to each other, as well as the energy levels, and it becomes difficult to identify the transitions. Moreover, the proposed effective spin hamiltonian works best for strongly coupled systems, while being an approximation for weakly coupled one. Therefore, the features at low energy can be influenced by an abmixture of energy levels and states not predicted by the proposed model.

What is explained by the simulation, however, is the non linearity of the observed features: the simulated resonant branches all curve down at low frequency, more or less following the data, even if the single transitions are not well identifiable. The non-linear features at higher field are not explained by this simulation: as the system is extremely complex, it's possible that not exactly all the powder grains got perfectly aligned along the supposed preferred orientation, and that this very weak observed resonances could be given by this slight non-alignment.

This, however, is a more complex problem which can't be exactly computed by the means employed for this thesis work.

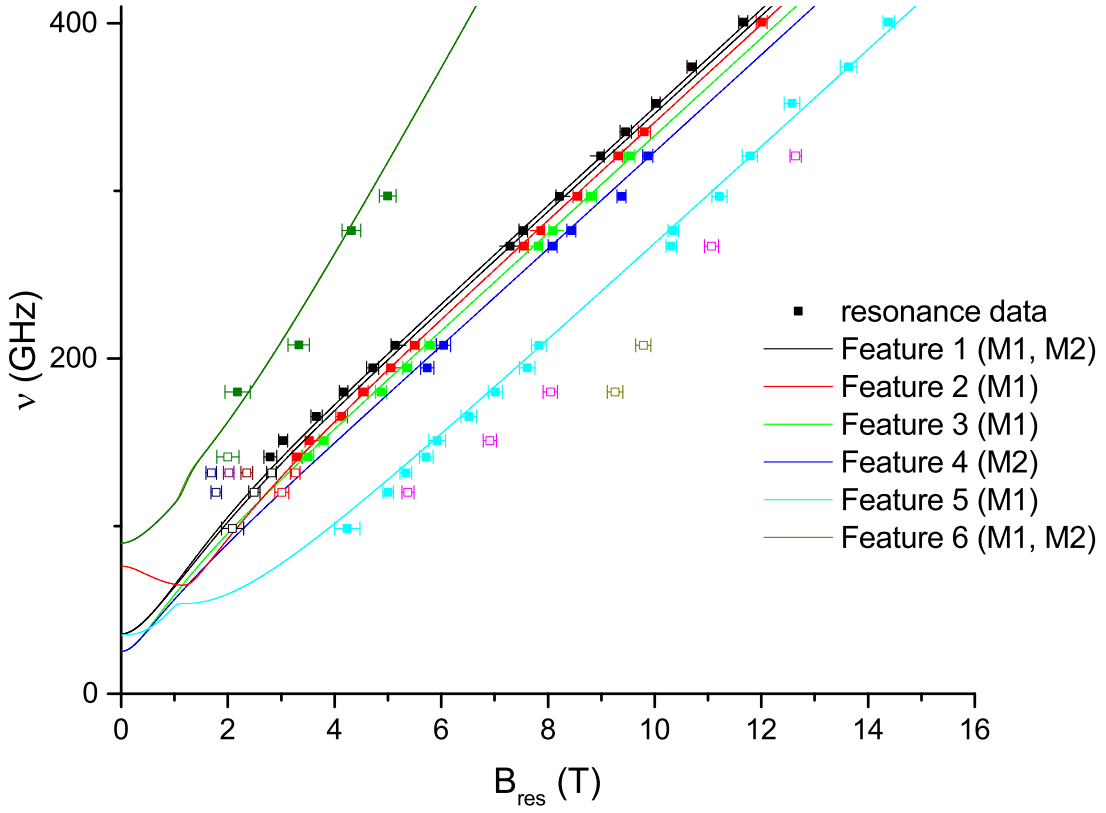

Figure 6.10: Resonance data compared to the simulated resonance branches for the Ni_2La sample. The plain dots are features computed by the simulation, while empty dots are features that can not be straight away observed in the proposed model.

6.1.3 Conclusions for the Ni_2La sample

In conclusion, the analyzed Ni_2La sample presents a complex crystal packing, with four possible spin orientations. This leads to the necessity of building an hamiltonian capable of taking into consideration all possible orientations. The proposed model is able to explain most of the resonant branches' behaviour observed from the data, and thus of giving reasonable magnetic parameters to describe the system.

The results show a slightly anisotropic g-tensor, with $g_x = g_y = 2.04(2)$ and $g_z = 2.12(1)$, where g_z is also in good agreement with the results from the linear fit. A distorted octahedral environment leads also to the presence of both D and E parameters, which are usually reported in Kelvin, with $D/k_B = -3.84(18)K$ and $E/k_B = 0.72(14)K$. The negative sign of the D factor is in agreement with the linear fitting of the data, as expected, and leads to the presence of an easy

axis anisotropy. The simulation also unambiguously yields to the necessity of introducing a weak ferromagnetic coupling, $J/k_B = -0.29(5)K$, between the two Nickel ions to explain the temperature dependant data. The superexchange coupling is carried out by the oxygen bridges, and is very weak due to the presence of the non-magnetic Lanthanium ion in between the two Nickels, but can be a good indicator of the capability of this compounds to couple Nickel and Lanthanide magnetic moments, which will be tested out in the Ni_2Ho sample.

6.2 Ni_2Ho

This section will discuss in detail the analysis and the results for the Ni_2Ho sample, following the layout of the previous section.

6.2.1 HF-EPR data

The HF-EPR measurements were carried out at a temperature T=2 K: as the Ho(III) is a high total angular momentum ion, with an high value of L and with high spin-orbit coupling, it is best to directly acquire spectra at the lowest possible temperature in order to isolate the ground state. The spectrum for frequency $\nu = 267.3GHz$ is reported in Fig. 6.11. The different resonance features are labelled with numbers for better identification. The features, in order of spectral weight, are found at $B = 10.2$ T (Feature 1), $B = 9.0$ T (Feature 2), $B = 9.5$ T (Feature 3), $B = 11.6$ T (Feature 4) and $B = 5.3$ T (Feature 5).

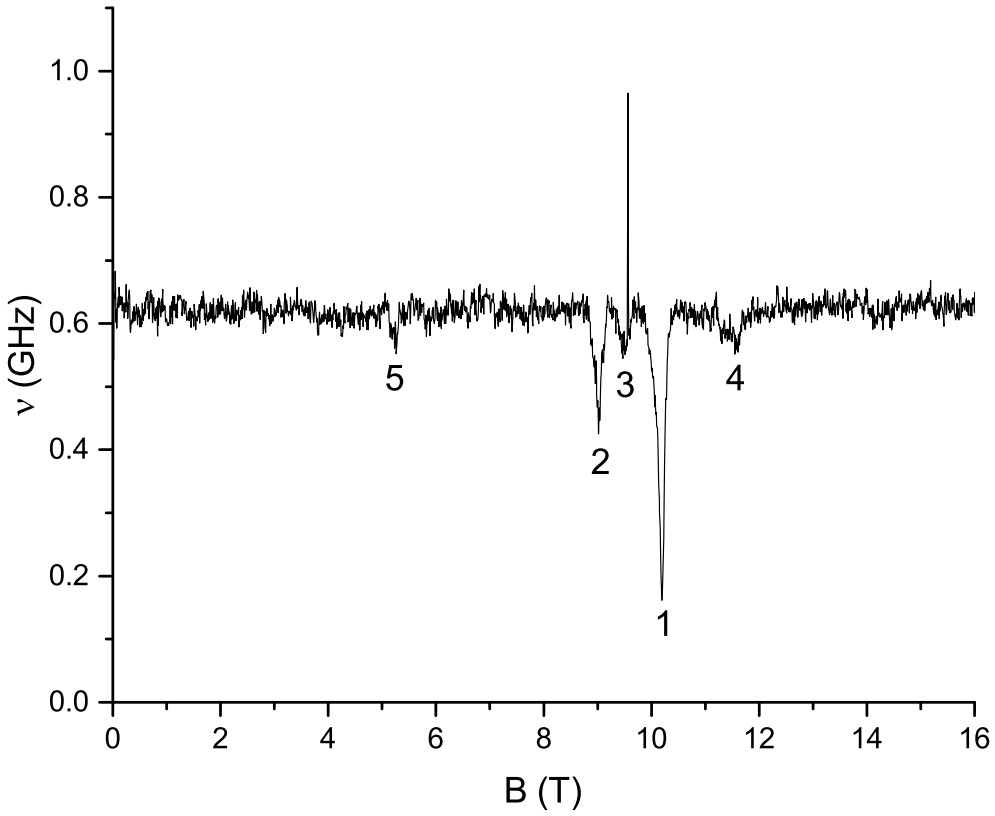

Figure 6.11: Ni_2Ho spectrum for frequency $\nu = 267.3$ GHz and temperature $T = 2$ K.

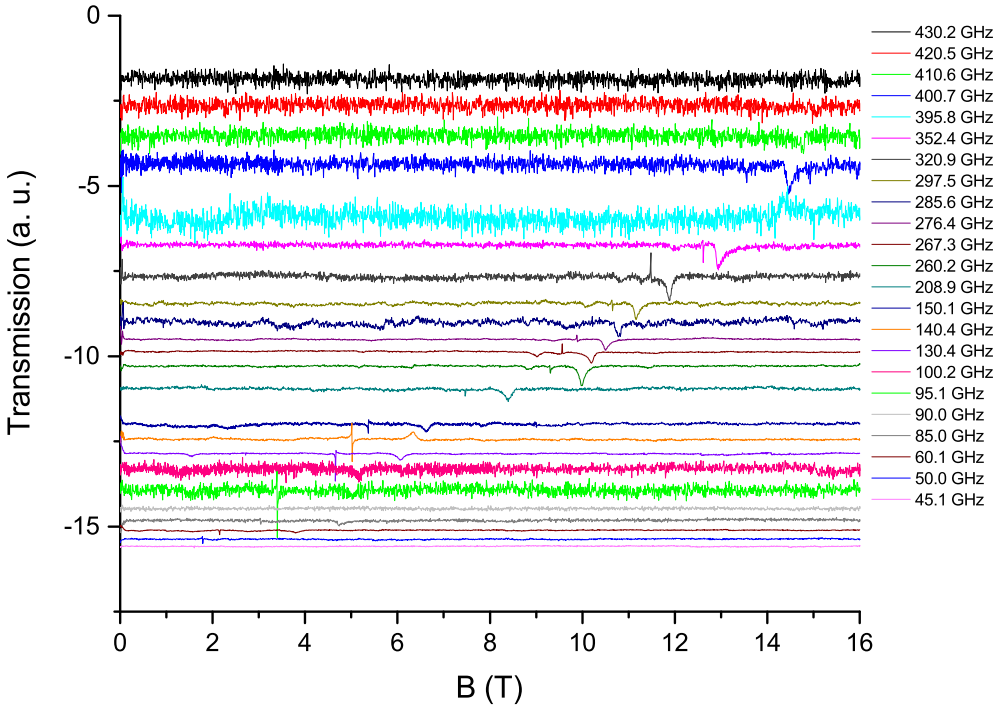

(a) Transmission spectra for the Ni_2Ho sample for various frequencies between ∼80-450 GHz. The presence of 1 main feature can be recognized in all graphs, while the others are weaker and diffcult to spot from this graph.

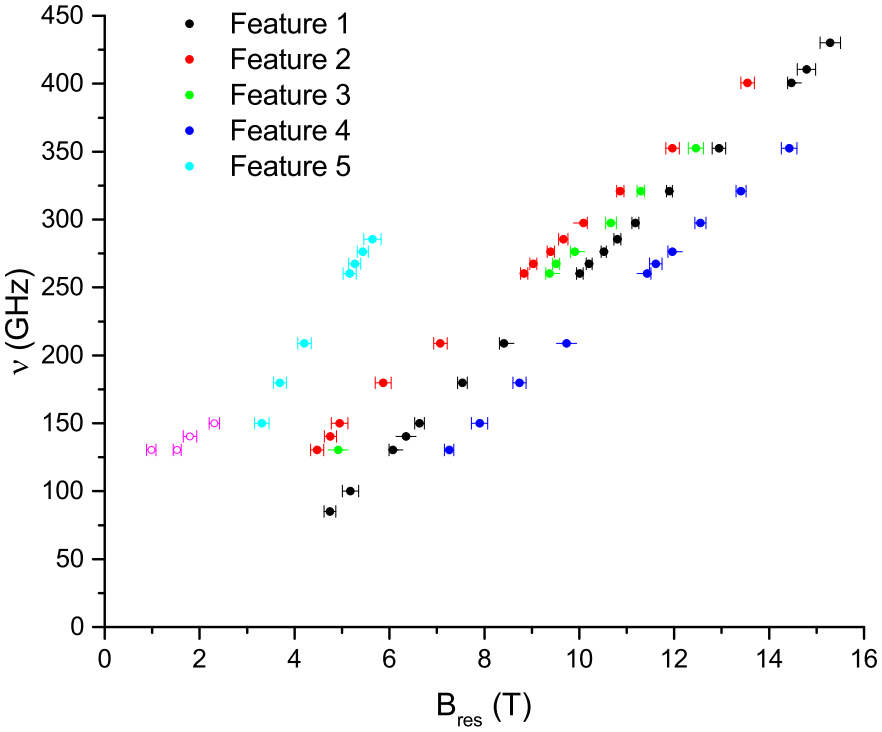

(b) Resonant features obtained for Ni_2Ho. The plain dots represent the features that linearly follow the ones observed at 267.3 GHz, the empty ones represent the features that were unexpected or non-linear in respect to the behaviour observed at the other frequencies.

Figure 6.12: Frequency dependant data for Ni_2Ho.

The frequency dependant spectra are shown in Fig. 6.12a. The lowest acquired frequency is $\nu = 85GHz$, as the resonance signal couldn't be observed for lower ones. The features described for $\nu = 267.3$ GHz can be better observed at higher frequencies. For lower ones ($\nu < 208.9$ GHz) Feature 3 became expecially difficult to identify, as it was mixed with the PEEK container signal, while the low resonance weight of Features 3 and 4 made them difficult to spot, as well.

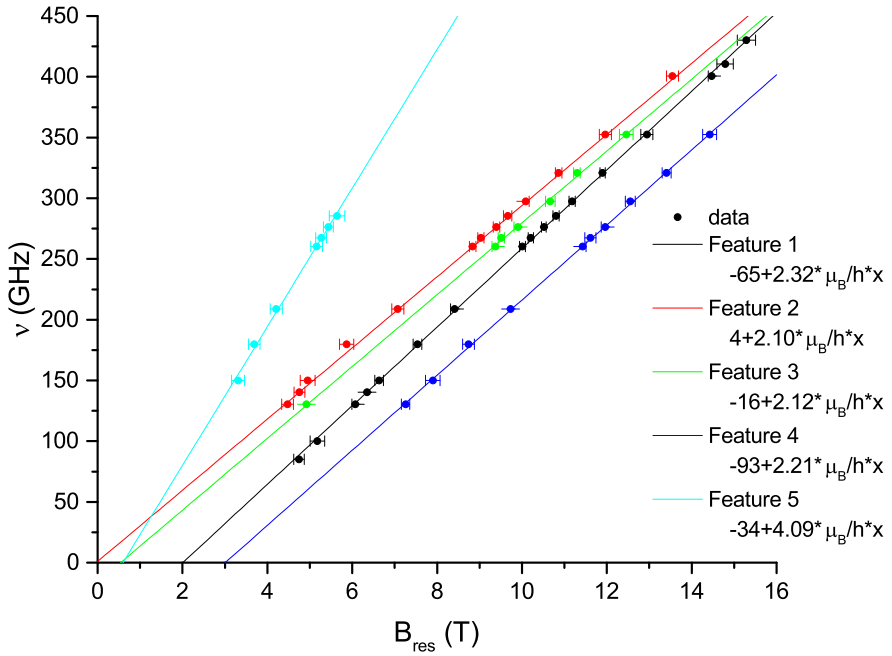

Figure 6.13: Ni_2Ho resonant features with linear behaviour and respective lines.

In Fig. 6.12b the frequency *vs* resonance-field graph is reported, as was done for Ni_2La. The resonance features are again attributed a weighted mean error from the up and down-sweep spectra acquisition. It can be observed, as previously mentioned, that the majority of data points is located at frequencies higher than 208.9 GHz. Apart from the 5 main resonance peaks, a 6^{th} feature is reported with empty dots, as it appears only for three low frequencies and it doesn't have a linear behaviour. This feature will be adressed to after the simulation work has been carried out.

In order to gain informations about the g-factor and the axial anisotropy D parameter, linear fitting of the resonance branches by means of the Origin program was carried out, as was done for Ni_2La. The results from the fitting procedure are reported in table 6.3.

The first thing to notice is that the lines which can be attributed to allowed transitions, $\Delta m_S = \pm 1$, present different slopes: this can be due to the anisotropy

	Slope	Intercept
Feature 1	$\frac{\mu_B}{h}(2.32 \pm 0.02)$	-65 ± 3 GHz
Feature 2	$\frac{\mu_B}{h}(2.10 \pm 0.03)$	1 ± 4 GHz
Feature 3	$\frac{\mu_B}{h}(2.12 \pm 0.04)$	-16 ± 5 GHz
Feature 4	$\frac{\mu_B}{h}(2.21 \pm 0.04)$	-93 ± 6 GHz
Feature 5	$\frac{\mu_B}{h}(4.09 \pm 0.26)$	-34 ± 17 GHz

Table 6.3: Slope and intercepts obtined from the linear fitting of the different features in Ni_2Ho, with the respective errors.

of the g-factor, meaning we could be able to observe different Ni(II) orientations with different g-factors. This will be tested with the effective spin hamiltonian simulation. The intercept of the lines can again give a rough idea of the magnitude of the D parameter. In this case, regardless of its sign, the self-alignment of the powder is guaranteed, by the presence of the Ho(III) ions: the strong single-ion anysotropy (see chapter 2) typical of 4f ions and the high magnetic moment create the conditions for the existence of a preferred orientation. The line of Feature 5 has an higher, and almost double, slope in respect to the others, suggesting that such resonance is connected to a forbidden transition. The lines obtained by the fit are reported in Fig. 6.13.

All the features observed until now can be attributed to ground state resonances, as they can be observed at the very low temperature of $T = 2$ K. In order to observe if the system could present any non ground-state transition, a temperature dependant measurement was carried out. The frequency chosen to perform it was $\nu = 130.4$ GHz. The obtained spectra are shown in Fig. 6.14a. As it can be observed, the spectra presents only three of the main features previously discussed, and they rapidly disappear with temperature, leaving no visible resonance at $T = 16$ K. There are no visible features arising with temperature, too, so no resonances from higher energy levels can be observed. The absence of features arising with temperature in lower fields and the slight transfer in spectral weight from higher to lower field with the rising of the temperature hints to the positive sign of the D parameter.

As the chosen spectra proved not really good for the temperature dependant

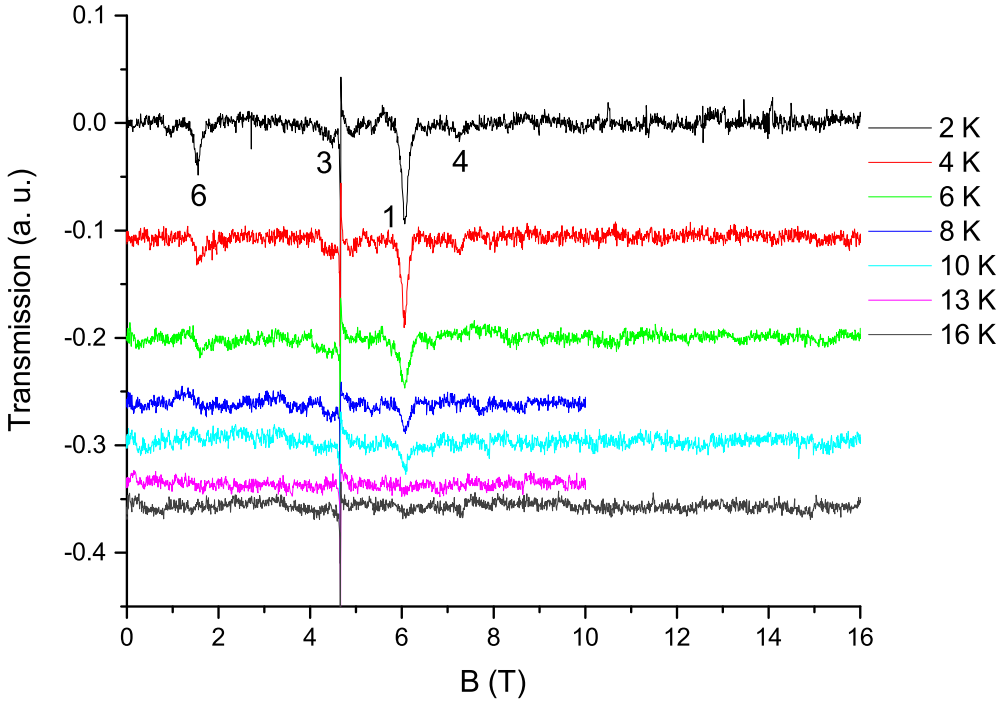

(a) Temperature dependance for Ni_2Ho at $T = 130.4$ GHz. The features at $T = 2$ K are labelled for better reading of the spectra.

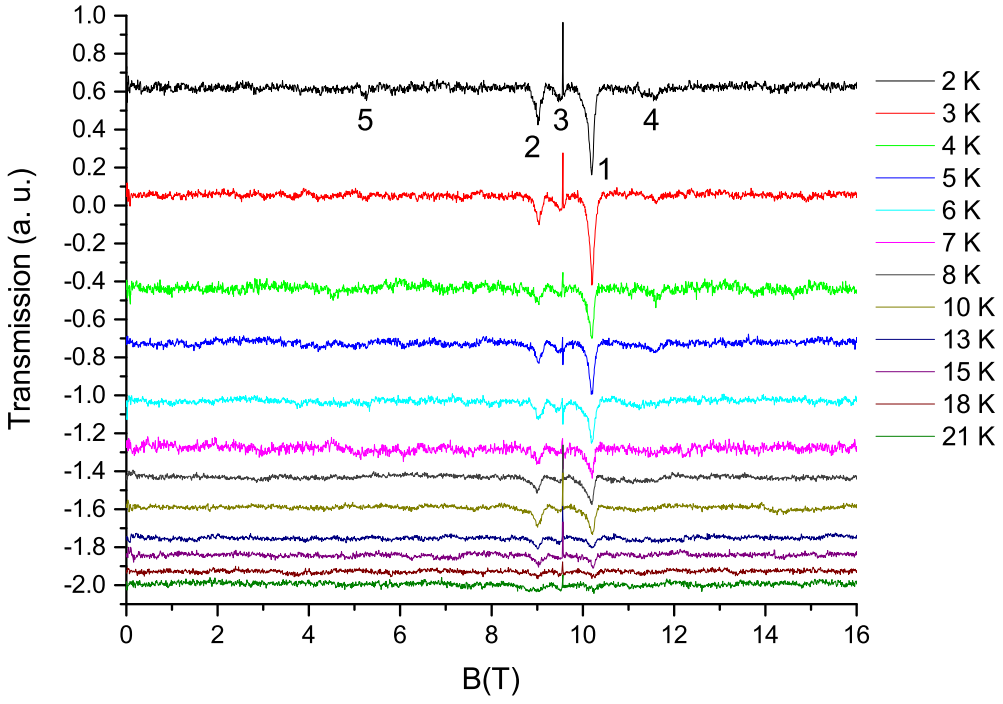

(b) Temperature dependance for Ni_2Ho at $T = 130.4$ GHz. The features at $T = 2$ K are labelled for better reading of the spectra.

Figure 6.14: Temperature dependant data for Ni_2Ho.

acquisition, presenting few features and not optimal noise, another such acquisition was carried out, this time at the previously reported frequency of $\nu = 267.3$ GHz. The new acquisition is reported in figure 6.14b. This time, the spectra present all the main features previously mentioned, from 1 to 5, with a higher signal-to-noise ratio than the previous acquisition. All the features go down with temperature, and eventually all disappear at $T = 21$ K, leading to the conclusion that no transition from higher energy levels can be observed. With the gathered information, it's possible to try building an hamiltonian for the system, adapting the one used for Ni_2La to the present case.

6.2.2 Simulation Work and Results

In the holmium case, a simulation is necessary, too, in order to find the most appropriate value of the D and E factor, to explain the different slopes observed for the 3 main features, and to try to evaluate the coupling of the Ni and Ho ions. The presence of three resonant features near to each other at most frequencies also require the inclusion of all four spin centers from the two main molecular orientation. As seen in 5, the measured angle between the molecules is 75.3°, and the torsion angle between them is of 30.8 degrees, with the 2 Ni(II) ions magnetic moments in one molecule having an angle of 36° between each other, and with one of the two being aligned to the magnetic moment of Ho(III). The same rotation script employed for the previous sample (see Fig. 6.8b) was used here, with one slight modification: in order to introduce the fact that the total magnetic moment of the molecule now is mainly determined by Ho(III), and thus lies along its direction, the angle α was set to 0°. The angle β was instead obtained by the confrontation between simulation and results.

In order to introduce in the hamiltonian the presence of a lanthanide with a non-null magnetic moment, a similar model as the one adopted by Okazawa et al. [9][10] was employed. In particular, the terms here reported refer to a [Dy_2Ni] compound. Due to the high single-ion anisotropy splitting the energy levels of the 4f ions in multiplets with decreasing $|m_J|$ (see chapter 2), with the ground state being bi-stable with $m_J = \pm 15/2$, the magnetic moment of Dysprosium was introduced in the hamiltonian as an Ising spin, with $|J_z| = 15/2$ and $g_J = 4/3$. The hamiltonian they developed for their complex is

$$\mathcal{H} = J_{Dy-Ni}(J^z_{Dy1} \cdot S^z_{Ni} + J^z_{Dy2} \cdot S^z_{Ni}) + D_{Ni}\left(S'^2_{z,Ni} - \frac{S_{Ni}(S_{Ni}+1)}{3}\right) + E_{Ni}(S'^2_{x,Ni} - S'^2_{y,Ni}) + \mu_B B^z g_{Dy}(J^z_{Dy1} + J^z_{Dy2}) + \mu_B g_{Ni}\vec{B} \cdot \vec{S}_{Ni} \tag{6.4}$$

As Easyspin doesn't natively support the insertion of a high megnetic moment Ising term (so with only up and down possible orientations), such a term was

created for the purpose of this thesis in the following way: a spin $S_{Dy} = 1/2$ was added to the system, and the total angular momentum value of $J = \pm 15/2$ was introduced by multiplying the terms containing the 1/2 spin by a constant $J_{Dy} = 15$. The z preferred direction of the orientation was introduced by means of a g-tensor in the form $\mathbf{g} = d(0, 0, g_D y)$, with $g_{Dy} = 4/3$, and an exchange coupling tensor of the form $\mathcal{J} = d(0, 0, J_{Dy-Ni})$. In this way, it was possible to introduce a high spin bi-stable Ising ion in an Easyspin hamiltonian. This script is reported, together with the other employed scripts, in Appendix B.

In order to test the developed script, a simulation of the compound previously cited was run. The comparison between the simulated energy levels and the ones computed in the article is reported in Fig. 6.15. As can be seen, the results are in perfect agreement with the the ones reported in literature, thus confirming that the proposed script is a good way to add a Lanthanide ion to the effective spin hamiltonian.

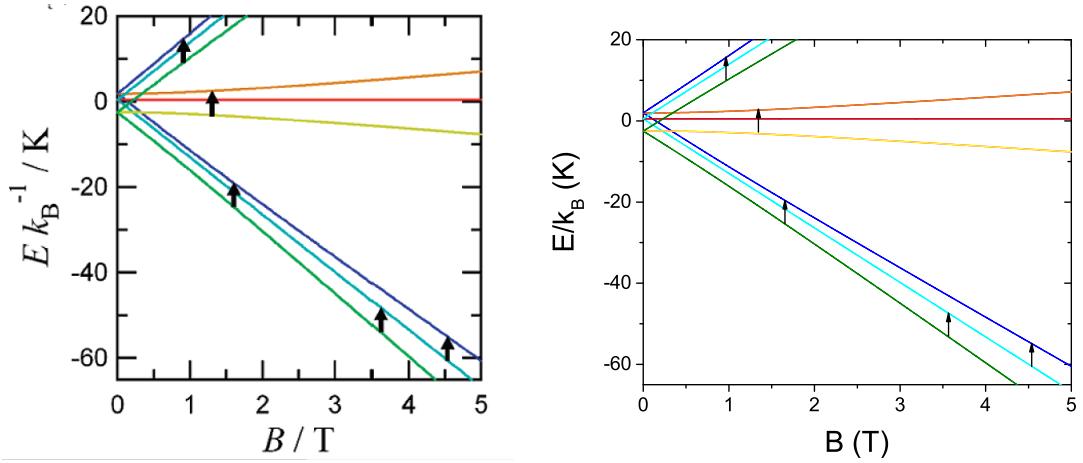

Figure 6.15: Confrontation between the energy levels from the Okazawa article with the simulated ones.

The final hamiltonian for the Ni_2Ho simulation is, putting together Eq. 6.3 and 6.4, in the form

$$\mathcal{H} = \sum_{i=1,2} \left(\mu_B \vec{B} \cdot \mathbf{R}_i^T \cdot \mathbf{g} \cdot \mathbf{R}_i \cdot \vec{S}_i + D \left((S'_{i,z})^2 - \frac{S_i(S_i+1)}{3} \right) + \right.$$
$$\left. + E \left((S'_{i,x})^2 - (S'_{i,y})^2 \right) \right) + J_{Ho-Ni}(J_{z,Ho} \cdot S_{z,1} + J_{z,Ho} \cdot S_{z,2}) + \mu_B g_{Ho} B_z \cdot J_{z,Ho} \tag{6.5}$$

where J_{Ho-Ni} is the coupling costant between the Nickel(III) and Holmium(II) ions, $g_{Ho} = 5/4$ is the Landé factor (see Eq. 3.12) and $J_{z,Ho} = 8$ the total angular

Parameter	Value
$g_x = g_y$	2.18 ± 0.02
g_z	2.32 ± 0.02
$D(GHz)$	90 ± 5
$E(GHz)$	28 ± 4
$J_{Ho-Ni}(GHz)$	-0.6 ± 0.1

Table 6.4: Hamiltonian paramters obtained from the simulation of the resonant branches of Ni_2Ho.

momentum for Ho(III) (from Hund's rules, the ground state for Ho(III) is $^4I_8$ [16]). The presence of the paramagnetic Ho ion in between the two Ni atoms prevents the superxchange coupling from connecting them, and the Ni-Ni coupling term can thus be neglected.

The proposed Hamiltonian written by the author for this thesis was first applied by Msia Tavhelidse for a crystalline sample of Ni_2Dy [21], obtaining a good agreement with the experimental data, with parameters $D = -2.5/k_B$ K, $E = 0.8/k_B$ K, g=2.14 and a ferromagnetic coupling of $J = -0.11/k_B$ K. The effective spin hamiltonian proposed can thus be considered a good approximation for the Ni_2Ln systems under study, and was diagonalized and solved in order to simulate the resonant branches of the Ni_2Ho sample, with the same process employed for Ni_2La. The final parameters for the hamiltonian are reported in table 6.4. The angle parameter employed was $\beta = (60 \pm 2)^\circ$.

The energy levels obtained for the two different molecules are reported in Fig. 6.16, as well as the proposed transitions for a frequency $\nu = 267.3$ GHz. The energy levels for this system split in a lot of different lines, as a result of the double interaction between the Ni ions and Holmium, so only the lowest in energy are reported in the picture. The highest are completely symmetric to the lowest ones, and are of no interest for the present results. Looking at the energy levels graphs, Feature 1 can be explained with a transtion form the first to the second energy level of the first molecule. Feature 2 can be explained either by a transition, in the first molecule, from the first to the third level, or a transition in the second molecule from the first to the second level. Feature 3 is obtained as a transition from the first to the second level in the first molecule, while Feature 5 is a transition from the first to the fourth level of the second molecule, and it is, as expected, a forbidden transition ($|\Delta m_S| > 1$). Finally, it is also possible to account for the presence of Feature 6, which can be described by the same transition from the first to the fourth level in the first molecule. As expected, none of the observed transitions is a resonance from a level higher than the ground state.

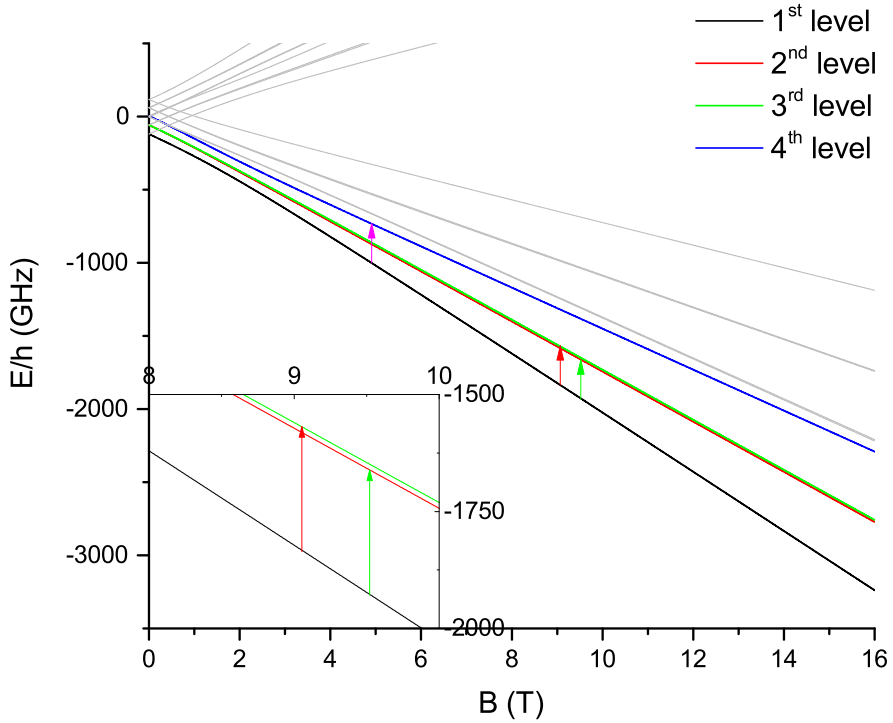

(a) Energy levels simulated for the first molecule. The transitions for Features 2, 3, and 6 can be observed.

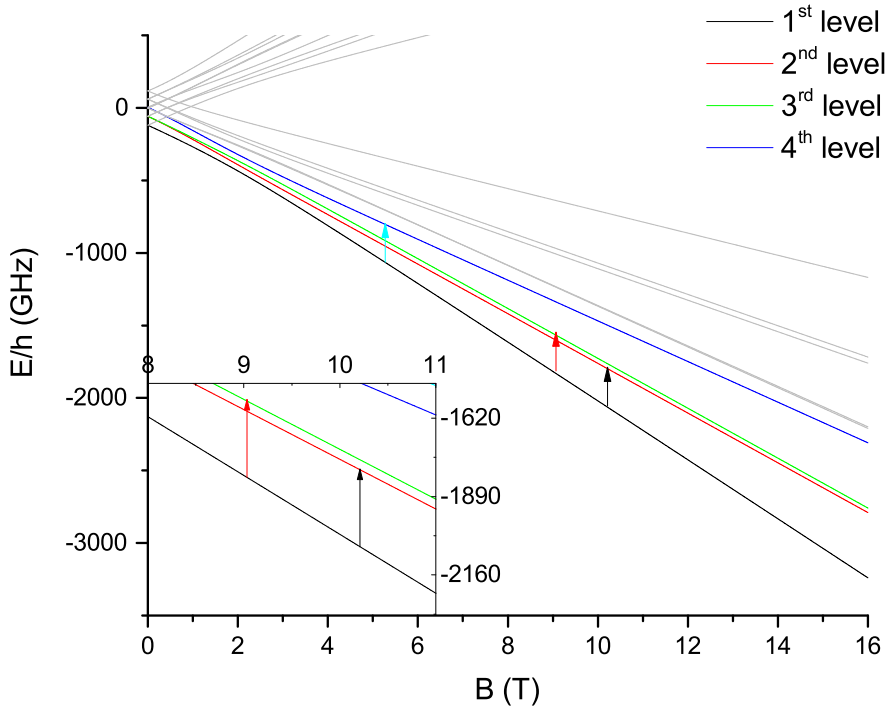

(b) Energy levels simulated for the second molecule. The transitions for Features 1, 2 and 5 can be observed.

Figure 6.16: Energy levels simulated for the system. The color of the arrows is linked to the obtained resonance: black for Feature 1, red for Feature 2, light green for Feature 3, light blue for Feature 5 and magenta for Feature 6.

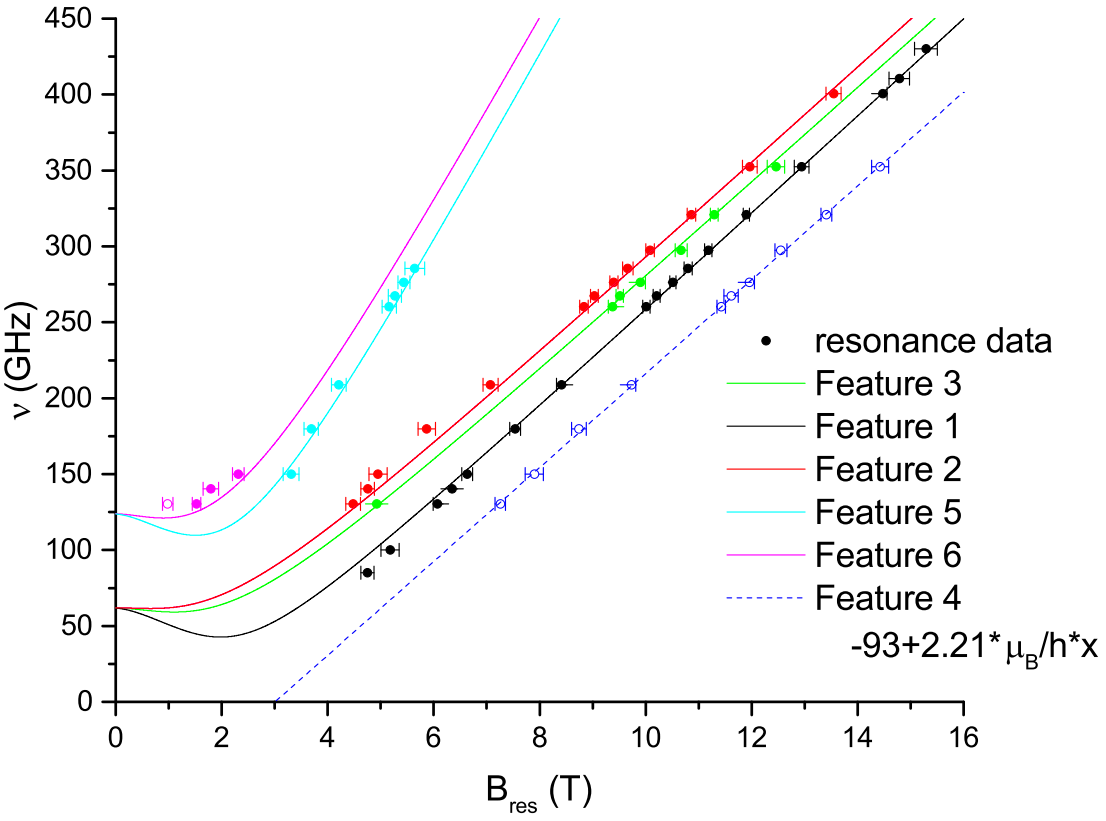

Figure 6.17: Resonance data compared to the simulated resonance branches for the Ni_2Ho sample. The plain dots are features computed by the simulation, while empty dots are features that can not be straight away reproduced with the proposed model.

The obtained resonant branches are reported in Fig. 6.17. The first thing to notice is that the preferred orientation of the powder hypothesised by the model does not address the presence of Feature 4. This resonance can however be explained by some grains which does not self-orient along the proposed direction, and show the easy plane transition of the Nickel atoms: this is confirmed by the low spectral weight of this feature at all frequencies, by its intercept value being perfectly compatible with the easy plane D parameter computed by the simulation, and by the g-factor obtained from the linear fitting, which is in agreement with the value of $g_x = g_y$ (the values of the g-tensor of Nickel in the easy plane.). The other features are in good agreement with the proposed branches. In particular, the difference in slope between features 1, 2 and 3 is reproduced by the simulation, meaning that the anisotropy of the g-factor can be observed due to the different molecular orientations. The ferromagnetic coupling is required in order for the

simulation to to be in agreement expecially with the resonant data of feature 5.

6.2.3 Conclusions for the Ni_2Ho sample

The analyzed Ni_2Ho sample presents a crystal packing very similar to that of Ni_2La, and presents four possible spin orientations, too. Moreover, the presence of the Ho(III) paramagnetic ion, with high magnetic moment (the ground state is $^4I_8$, with a total angular momentum J=8). This leads to the necessity of adding a new term to the previously built hamiltonian, which takes into consideration the high-spin contribution of the Ho ion.

The proposed model is able to explain most of the resonant branches' behaviour observed from the data, and thus of giving reasonable magnetic parameters to describe the system, both for the present Ni_2Ho sample and for a similar Ni_2Dy sample.

The results show an anisotropic g-tensor, with $g_x = g_y = 2.18(2)$ and $g_z = 2.32(2)$, where g_z is also in good agreement with the results from the linear fit of the main resonance feature, while the lower value of $g_x = g_y$ helps explain the different slope of the other features observed in the data. A distorted octahedral environment leads also to the presence of both D and E parameters, with $D/k_B = 4.32(24)$K and $E/k_B = 1.34(19)$K.

The positive sign of the D factor is in agreement with the linear fitting of the data, and leads to the presence of an easy plane ground state, differently from the Ni_2La sample. The simulation also requires the presence of a weak ferromagnetic coupling $J = -0.029(5)$ K between the Ni and the Holmium atoms, carried out by the same exchange interaction proposed for Ni_2La. The difference in magnitude of the exchange interaction, and the abilty to determine it more precisely, comes from the fact that both Ni ions interact with the high magnetic moment of the Ho ion, giving a contribution to the energy of the system much greater than the one obtained by the interaction between the two Nickel ions in the Ni_2La system.

Chapter 7

Conclusions

The work presented in this thesis consisted in the study of two trinuclear heterometallic complexes by means of High Frequency/High Field Electron Paramagnetic Resonance (HF-EPR) Spectroscopy. The two complexes under analysis were two *3d-4f* metalorganic compounds with chemical formula $[Ln(III)Ni(II)(L^{tacn})_2]ClO_4$. The lanthanide Ln was chosen to be either La or Ho. These two compounds are referred to, respectively, as Ni_2La and Ni_2Ho and they both presented themselves as microcrystalline powders.

These two compounds were examined whithin the frame of a bigger, systematic effort to explore the magnetization characteristics of lanthanide metalorganic complexes, in order to find suitable candidates for the realization of Single Molecular Magnets at relatively high temperatures.

Transmission spectra were gathered for the two compounds at various frequencies, in the range 50-450 GHz, and the spectra were subsequently analyzed in order to determine the resonance-field position of the resonance features. Temperature dependant measurement where also gathered, in order to obtain informations about energy level transitions which could describe the observed features.

The first sample analyzed was Ni_2La. The linear fitting of the resonance features in a frequency *vs* field graph was performed, showing an intercept of the lines consistent with an easy axis axial anisotropy, with $D < 0$. The temperature dependant measurement showed the presence of two resonance features from excited states. After carefully analyzing the molecular informations about the compound, a spin effective hamiltonian model for the system was built. The hamiltonian was diagonalized and solved in order to obtain the energy levels of the system, and simulated resonant branches were computed from them. These were tuned to the data in order to obtain the best estimate of the magnetic parameters which describe the system.

The final results were $g_x = g_y = 2.04(2)$, $g_z = 2.12(1)$, $D/k_B = -3.84(19)$ K,

$E/k_B = 0.72(14)$ K and $J/k_B = -0.29(5)$ K. These values point to a system with Ni ions in a distorted octahedral coordination, with a strong easy axis anisotropy and slightly anisotropic g-factor. The determination of the weak ferromagnetic coupling was mainly due to the complex molecular structure of the system, which created the conditions for the observation of a resonance from an excited state connected with an energy level created by the coupling.

The linear fitting and temperature dependant analysis was than employed for the analysis of the Ni_2Ho compound, as well. Contrary to the case of the Ni_2La, the linear fitting yielded slopes of the resonant branches which suggested an easy plane anisotropy, with $D > 0$. The temperature dependant acquisition characterized all the observed resonances as ground-state transitions. The hamiltonian used for Ni_2La was then updated to include the presence of a magnetic *4f* ion, and the simulation process was repeated for the Ni_2Ho sample.

The final results were $g_x = g_y = 2.18(2)$, $g_z = 2.32(2)$, $D/k_B = 4.32(24)$ K, $E/k_B = 1.34(19)$ K and $J = -0.029(5)$ K. Again, these values point to a system with the two Ni ions inserted in a distorted octahedral coordination, with a strong easy plane anisotropy and anisotropic g-factor. The peculiar orientation of the molecules made it possible to observe the anisotropy of the g-factor from an oriented powder spectra, as the different lines had different slopes, connected with the values of $g_x = g_y$ and g_z.

The obtained results demonstrated that HF-EPR is capable of detecting the exchange coupling, carried out by the ligand bridges, inside *3d-4f* compounds produced on the model of Ni_2La. It was thus shown that these compounds are good candidates for SMM applications, thanks also to the anisotropy of the Ni ions. Moreover, they showed the sensitivity of HF-EPR to the peculiar molecular and spin orientations and that informations about the angles of the systems are vital in order to correctly reproduce the observed data.

Lastly, they showed that the substitution of one *4f* ion with another, even if the shape of the molecule remains unchanged, has strong effects on the Ni ions coordination and thus on their anisotropy. In particular, in the present thesis, it was shown that the Ni anisotropy goes from easy axis to easy plane when substituting the La ion with Ho. This has to be taken in serious consideration for future improvements on this class of complexes, as having an easy plane condition for the Ni ions is more suitable for the increase in anisotropy of the system.

The results presented here are consistent to literature-known values obtained from the study of similar compounds. In fact, a positive value of the D factor is a shared characteristic with the complexes studied by Okazawa [10]. These compounds yielded values for D similar to the ones found for the Holmium sample present in this thesis (see 2.1), but showed better exchange coupling between the Nichel and Lanthanide ions. This comparison makes it clear that the study of the

different ligands carrying the coupling in this class of compounds will be necessary in order to find new ways of improving the coupling.

The simulation work done for this thesis will help in the analysis of other compounds of the class [Ni_2Ln], having already being employed for the analysis of a crystal sample of Ni_2Dy [21], which showed better exchange coupling of $J/k_B = -0.11$ K and easy axis $D/k_B = -2.5$ K. The informations gathered by comparing the results of the different lanthanides will help in the building of more refined *3d-4f* complexes, in order to improve the anisotropy and coupling and obtain better SMMs performances.

Appendix A

PEEK Container Signal

The experimental spectra shown in this thesis work always presented, among the others, a very sharp resonance feature, not related with the sample under analysis. In order to explain it, an empty PEEK container was analyzed by HF-EPR. The PEEK container was cleaned by using ethanol, acetone and ultrasonic cleaning, in ordernto avoid external contamination. In Fig. A.1 are reported three spectra taken at different frequencies for the empty and cleaned PEEK container: the presence of the sharp resonance feature even in the absence of a sample showed that such feature was indeed realted to the PEEK container itself. The three resonance features have been linearly fitted, obtaining a line with a g-factor of 1.99(7) and an intercept of 0.73(50). This resuts are perfectly compatible with the resonace of a free electron, S=1/2, which can be easily explained by the presence of a free radicalin the PEEK material. The resonances and the fitting line are reported in Fig. A.2.

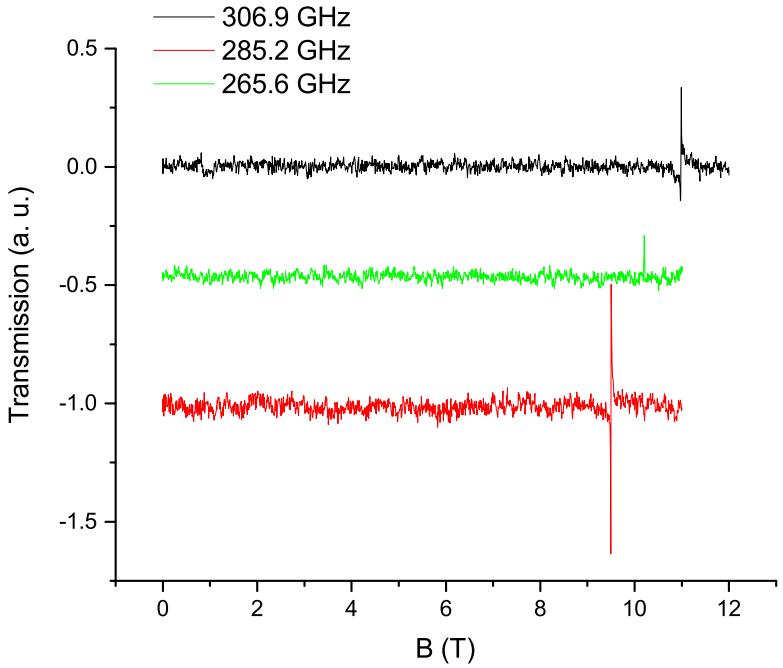

Figure A.1: Transmission spectra obtained at three different fre quencies for the empty and cleaned PEEK container.

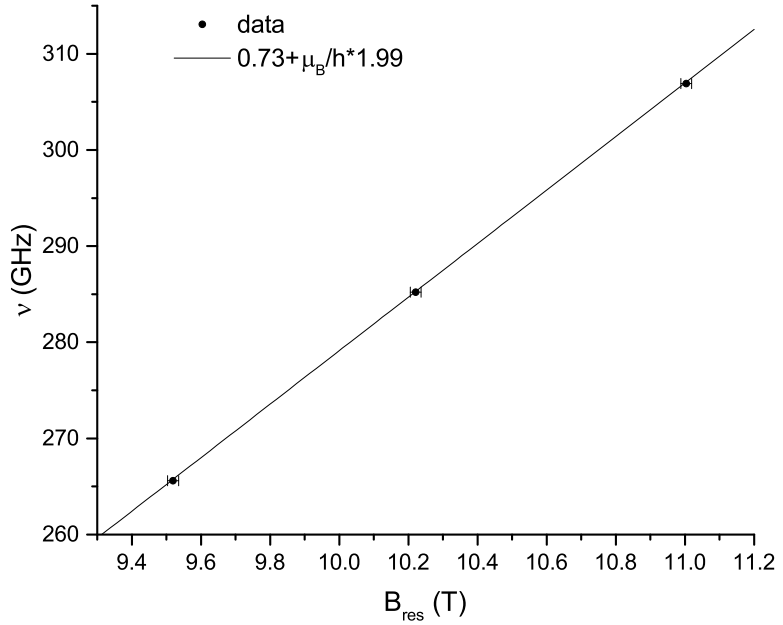

Figure A.2: Resonance data and linear fitting for the PEEK container feature.

Appendix B

MATLAB Scripts

Here are reported all MATLAB scripts adopted for the present thesis work.

B.1 Ni_2La Script

Here is reported the MATLAB script used for the Ni_2La Hamiltonian building, diagonalization and solving by the Easyspin toolbox.

```
close all
clearvars
%Building the rotation matrices
choice='s'; %'s' to show the molecular orientations diagram
    ,
%'n' to not show it
[R11,R12,R21,R22,R1,R2]=Rotazioni(35.13,13.6,90,22,choice
    ,1); %34.93
%Calling the function to build rotation matrices

%Common system parameters
S=1;
D=-80*1e3;
E=15*1e3;
J=-6*1e3;
g1=2.04;
g2=2.04;
g3=2.12;
g=[g1 g2 g3];
B=linspace(0,16000,6400);
Ori=[0 0]*pi/180;
```

```
20
21 %First molecule
22 Sys1.S=[S,S];
23 Sys1.g=[g;g];
24 Sys1.D=[D E; D E];
25 Sys1.DFrame=[eulang(R11) ; eulang(R12)]; %Rotation of the D
       frame according
26 %to spin orientation
27 R=erot(eulang(R11));
28 disp(R);
29 Sys1.gFrame=[eulang(R11) ; eulang(R12)]; %Rotation of the g
       frame according
30 %to spin orientation
31 Sys1.ee=J; %isotropic exchange interaction
32 Sys1.eeFrame=eulang(R1);
33 Sys1.lw=[150 150]; %linewidth: mixture of gaussian and
     lorentzian
34
35 %Second molecule
36 Sys2.S=[S,S];
37 Sys2.g=[g;g];
38 Sys2.D=[D E; D E];
39 Sys2.DFrame=[eulang(R21) ; eulang(R22)]; %Rotation of the D
       frame according
40 %to spin orientation
41 Sys2.gFrame=[eulang(R21) ; eulang(R22)]; %Rotation of the g
       frame according
42 %to spin orientation
43 Sys2.ee=J; %isotropic exchange interaction
44 Sys2.eeFrame=eulang(R2);
45 Sys2.lw=[150 150]; %linewidth: mixture of gaussian and
     lorentzian
46
47 %Energy levels diagrams
48 E1=1e-3*levels(Sys1,Ori,B);
49 E2=1e-3*levels(Sys2,Ori,B);
50 [B,E1]=sort_elevel(B,E1);
51 [B,E2]=sort_elevel(B,E2);
52 figure;
53 plot(B,E1);
```

```
figure;
plot(B,E2);

%Frequency vs field diagram
nu=[];
nu(:,1)=E1(:,2)-E1(:,1); %second main feature, from first molecule
nu(:,2)=E1(:,3)-E1(:,1); %first main feature
nu(:,3)=E2(:,2)-E2(:,1); %second main feature, from first molecule
nu(:,4)=E2(:,3)-E2(:,1); %first main feature
nu(:,5)=E1(:,4)-E1(:,1); %forbidden transition, lower field, around 4.5 T
nu(:,6)=E2(:,4)-E2(:,1); %forbidden lower field
nu(:,7)=E1(:,4)-E1(:,2); %feature at around 10.2 T, case 6,7,8,9,10
nu(:,8)=E1(:,6)-E1(:,2); %forbidden 7.8 T for case 2,4,8
simR = [B nu];
%xlswrite('Ni2La_sim',simR);

figure;
[Bf,feat] = textread('Ni2La_features_2.txt','%f %f');
plot(B,nu,Bf*1e3,feat,'r+');
ylim([0;450]);
xlabel('B (mT)');
ylabel('Frequency (GHz)');
simR1=[B*1e-3 E1];
%xlswrite('Lamol1',simR1);
simR2=[B(:)*1e-3 E2];
%xlswrite('Lamol2',simR2);
```

B.2 Ni_2Ho Script

Here is reported the MATLAB script used for the Ni_2Ho Hamiltonian building, diagonalization and solving by the Easyspin toolbox.

```
close all
clearvars

%Building the rotation matrices
```

```
choice='s';
[R11,R12,R21,R22,R1,R2]=Rotazioni(34.82,30.77,60,1e-3,
    choice,2);

%Common system parameters
S=1;                    %Nickel
Jz=1/2;
JHo=16;%Holmium
gxy=2.18;
gz=2.32;
gHo=5/4*JHo;
D=90*1e3;
E=28*1e3;
J=-0.6*1e3*JHo;
Ori=[0 0]*pi/180;
B=linspace(0,16000,6400);

%First molecule
Sys1.S=[S;Jz;S];
Sys1.g=[gxy gxy gz; 0 0 gHo; gxy gxy gz];
Sys1.gFrame=[eulang(R11) ; 0 0 0  ; eulang(R12)];
Sys1.D=[D E; 0 0; D E];
Sys1.DFrame=[eulang(R11) ; 0 0 0 ; eulang(R12)];
Sys1.ee=[0 0 J; 0 0 0; 0 0 J];
Sys1.lw=[80 80];

%Second molecule
Sys2.S=[S;Jz;S];
Sys2.g=[gxy gxy gz; 0 0 gHo; gxy gxy gz];
Sys2.gFrame=[eulang(R21) ; 0 0 0 ; eulang(R22)];
Sys2.D=[D E; 0 0; D E];
Sys2.DFrame=[eulang(R21) ; 0 0 0 ; eulang(R22)];
Sys2.ee=[0 0 J; 0 0 0; 0 0 J];
Sys2.lw=[80 80];

E1=1e-3*levels(Sys1,Ori,B); %Energy levels for the first
    molecule
E2=1e-3*levels(Sys2,Ori,B); %Energy levels for the second
    molecule
[B,E1] = sort_elevel(B,E1);
```

```
[B,E2] = sort_elevel(B,E2);
simR1=[B*1e-3 E1];
%xlswrite('Ni2Homol1',simR1);
simR2=[B*1e-3 E2];
%xlswrite('Ni2Homol2',simR2);
figure;
plot(B,E1);
figure;
plot(B,E2);
nu(:,1)=E1(:,2)-E1(:,1); %resonant branches caomputation
nu(:,2)=E1(:,3)-E1(:,1);
nu(:,3)=E2(:,2)-E2(:,1);
nu(:,4)=E2(:,3)-E2(:,1);
nu(:,5)=E1(:,4)-E1(:,1);
nu(:,6)=E2(:,4)-E2(:,1);
figure;
[B1,f] = textread('Ho_feat.txt','%f %f');
plot(B,nu,B1*1000,f,'r+');
ylim([0;450]);

simR = [B*1e-3 nu];
%xlswrite('Ni2Ho_sim',simR);
```

B.3 Reference Frame Rotation Scripts

B.3.1 Rotazioni

Here is reported the script used to obtain the correct reference frame rotations for the 4 spins taken in ìnto consideration by the simulation.

```
function [varargout]=Rotazioni(tilt,beta,gamma,diff,choice,
    el)

%The function uses Rotate2 for building matrices for
    rotations around a
%given axis

%Common axis reference frame
x=[1;0;0];
y=[0;1;0];
```

```
9  z=[0;0;1];
10
11 if el==1
12      alfa=70.26;%69.86; 70.26 this angle is chosen to have a
            ~71.4 angle
13     %between molecules after 13.6 degrees twisting
14 elseif el==2
15      alfa=69.64;%69.64: this angle is chosen to have a ~75.3
            angle between
16     %molecules after 30.77 degrees twisting
17 end
18
19 phi=36; %tilting between the nichel ions
20 %First molecule building
21
22 rot=rotx(-tilt); %rotation around original frame x axis to
       get the first
23 %moelcule tilting to the common axis
24 R1=rot;
25 x1=rot*x; %Building the new reference frame
26 y1=rot*y;
27 z1=rot*z;
28 rot=Rotate2(-(tilt/alfa)*beta,y1); %Rotation around new
       reference y axis to
29 %have the right planar tilting: each molecule is tilted in
       the plane
30 %proportionally to the previous angle
31 R1=rot*R1; %Building the new reference frame
32 x2=rot*x1;
33 y2=rot*y1;
34 z2=rot*z1;
35 rot=Rotate2(-gamma,z2); %Rotation around the new reference
       frame z axis:
36 %this makes the spin rotate around the molecule
37 R1=rot*R1;
38 xM1=rot*x2; %Building the new reference frame = molecular
       frame,
39 %first molecule
40 yM1=rot*y2;
41 zM1=rot*z2;
```

```
42 rot=Rotate2(-diff,xM1); %Rotation around the molecular
     frame z axis to get
43 %the first spin tilting in respect to it
44 R11=rot*R1; %Rotation matrix for the first spin of the
     first molecule
45 varargout{1}=R11;
46 xM1S1=rot*xM1; %Building the first spin reference frame
47 yM1S1=rot*yM1;
48 zM1S1=rot*zM1;
49 rot=Rotate2(sign(diff)*(phi-abs(diff)),xM1); %Rotation
     around the molecular
50 %frame z axis to get the second spin tilting in respect to
     it
51 R12=rot*R1; %Rotation matrix for the second spin of the
     first molecule
52 varargout{2}=R12;
53 xM1S2=rot*xM1; %Building the second spin reference frame
54 yM1S2=rot*yM1;
55 zM1S2=rot*zM1;
56 costheta = dot(zM1S1,z)/(norm(zM1S1)*norm(z));
57 theta11 = acos(costheta)*180/pi; %Angle between the
     starting z axis and the
58 %first spin direction (z axis of the spin frame)
59 varargout{5}=R1;
60 costheta = dot(zM1S2,z)/(norm(zM1S2)*norm(z));
61 theta12 = acos(costheta)*180/pi; %Angle between the
     starting z axis and the
62 %second spin direction (z axis of the spin frame)
63
64 %Second molecule bulding
65 rot=rotx(alfa-tilt);
66 R2=rot;
67 x1=rot*x;
68 y1=rot*y;
69 z1=rot*z;
70 rot=Rotate2(((alfa-tilt)/alfa)*beta,y1);
71 R2=rot*R2;
72 x2=rot*x1;
73 y2=rot*y1;
74 z2=rot*z1;
```

```
75  rot=Rotate2(gamma,z2);
76  R2=rot*R2;
77  xM2=rot*x2;
78  yM2=rot*y2;
79  zM2=rot*z2;
80  rot=Rotate2(-sign(diff)*(phi-abs(diff)),xM2);
81  R21=rot*R2; %Rotation matrix for the first spin of the
        second molecule
82  varargout{3}=R21;
83  xM2S1=rot*xM2;
84  yM2S1=rot*yM2;
85  zM2S1=rot*zM2;
86  rot=Rotate2(diff,xM2);
87  R22=rot*R2; %Rotation matrix for the second spin of the
        second molecule
88  varargout{4}=R22;
89  xM2S2=rot*xM2;
90  yM2S2=rot*yM2;
91  zM2S2=rot*zM2;
92  costheta = dot(zM2S1,z)/(norm(zM2S1)*norm(z));
93  theta21 = acos(costheta)*180/pi;
94  varargout{6}=R2;
95  costheta = dot(zM2S2,z)/(norm(zM2S2)*norm(z));
96  theta22 = acos(costheta)*180/pi;
97
98  costheta = dot(zM1,zM2)/(norm(zM1)*norm(zM2));
99  thetac = acos(costheta)*180/pi;
100 disp(thetac);
101
102 %3D Plot of the molecular structure diagram
103 if choice=='s'
104     X=[0,0,0,0,zM1(1)*3/4,zM1(1)*1/4,0,zM2(1)*3/4,zM2(1)
            *1/4];
105     Y=[0,0,0,0,zM1(2)*3/4,zM1(2)*1/4,0,zM2(2)*3/4,zM2(2)
            *1/4];
106     Z=[0,0,0,0,zM1(3)*3/4,zM1(3)*1/4,0,zM2(3)*3/4,zM2(3)
            *1/4];
107     U=[x(1),y(1),z(1),zM1(1),zM1S1(1)/3,zM1S2(1)/3,zM2(1),
            zM2S1(1)/3,zM2S2(1)/3];
```

```
108             V=[x(2),y(2),z(2),zM1(2),zM1S1(2)/3,zM1S2(2)/3,zM2
                    (2),zM2S1(2)/3,zM2S2(2)/3];
109         W=[x(3),y(3),z(3),zM1(3),zM1S1(3)/3,zM1S2(3)/3,zM2(3),
                zM2S1(3)/3,zM2S2(3)/3];
110         scale=0;
111         figure;
112         quiver3(X,Y,Z,U,V,W,scale);
113 end
```

B.3.2 Rotate2

Here is reported the script used to obtain a rotation around a given direction in space.

```
1 function rot=Rotate2(phi,u)
2     phi=phi*pi/180;
3     u(1)=u(1)/norm(u);
4     u(2)=u(2)/norm(u);
5     u(3)=u(3)/norm(u);
6     uu=[u(1)^2,u(1)*u(2),u(1)*u(3);u(1)*u(2),u(2)^2,u(2)*u
          (3);u(1)*u(3),u(2)*u(3),u(3)^2];
7     uper=[0,-u(3),u(2);u(3),0,-u(1);-u(2),u(1),0];
8     rot=cos(phi)*eye(3)+sin(phi)*uper+(1-cos(phi))*uu;
```

Bibliography

[1] Wolfgang Wernsdorfer. Molecular nanomagnets: towards molecular spintronics. *International Journal of Nanotechnology*, 7(4-8):497–522, 2010.

[2] T Lis. Preparation, structure, and magnetic properties of a dodecanuclear mixed-valence manganese carboxylate. *Acta Crystallographica Section B: Structural Crystallography and Crystal Chemistry*, 36(9):2042–2046, 1980.

[3] M Affronte, F Troiani, A Ghirri, A Candini, M Evangelisti, V Corradini, S Carretta, P Santini, G Amoretti, F Tuna, et al. Single molecule magnets for quantum computation. *Journal of Physics D: Applied Physics*, 40(10):2999, 2007.

[4] George Christou, Dante Gatteschi, David N Hendrickson, and Roberta Sessoli. Single-molecule magnets. *Mrs Bulletin*, 25(11):66–71, 2000.

[5] Haruki Eguchi, Masanari Umemura, Reiko Kurotani, Hidenobu Fukumura, Itaru Sato, Jeong-Hwan Kim, Yujiro Hoshino, Jin Lee, Naoyuki Amemiya, Motohiko Sato, et al. A magnetic anti-cancer compound for magnet-guided delivery and magnetic resonance imaging. *Scientific reports*, 5, 2015.

[6] Jeffrey D Rinehart and Jeffrey R Long. Exploiting single-ion anisotropy in the design of f-element single-molecule magnets. *Chemical Science*, 2(11):2078–2085, 2011.

[7] Lidia Rosado Piquer and E Carolina Sañudo. Heterometallic 3d–4f single-molecule magnets. *Dalton Transactions*, 44(19):8771–8780, 2015.

[8] Naoto Ishikawa, Miki Sugita, and Wolfgang Wernsdorfer. Nuclear spin driven quantum tunneling of magnetization in a new lanthanide single-molecule magnet: bis (phthalocyaninato) holmium anion. *Journal of the American Chemical Society*, 127(11):3650–3651, 2005.

[9] Atsushi Okazawa, Takashi Nogami, Hiroyuki Nojiri, and Takayuki Ishida. Ferromagnetic dy- ni and antiferromagnetic dy- cu couplings in single-molecule magnets [dy2ni] and [dy2cu]. *Inorganic chemistry*, 47(21):9763–9765, 2008.

[10] Atsushi Okazawa, Takashi Shimada, Norimichi Kojima, Shunsuke Yoshii, Hiroyuki Nojiri, and Takayuki Ishida. Exchange coupling and its chemical trend studied by high-frequency epr on heterometallic [ln2ni] complexes. *Inorganic chemistry*, 52(23):13351–13355, 2013.

[11] Ayuk M Ako, Ian J Hewitt, Valeriu Mereacre, Rodolphe Clérac, Wolfgang Wernsdorfer, Christopher E Anson, and Annie K Powell. A ferromagnetically coupled mn19 aggregate with a record s= 83/2 ground spin state. *Angewandte Chemie*, 118(30):5048–5051, 2006.

[12] Shutaro Osa, Takafumi Kido, Naohide Matsumoto, Nazzareno Re, Andrzej Pochaba, and Jerzy Mrozinski. A tetranuclear 3d- 4f single molecule magnet:[cuiiltbiii (hfac) 2] 2. *Journal of the American Chemical Society*, 126(2):420–421, 2004.

[13] Jean-Pierre Costes, Sergiu Shova, and Wolfgang Wernsdorfer. Tetranuclear [cu–ln] 2 single molecule magnets: synthesis, structural and magnetic studies. *Dalton Transactions*, (14):1843–1849, 2008.

[14] Fumihito Mori, Tetsuya Nyui, Takayuki Ishida, Takashi Nogami, Kwang-Yong Choi, and Hiroyuki Nojiri. Oximate-bridged trinuclear dy- cu- dy complex behaving as a single-molecule magnet and its mechanistic investigation. *Journal of the American Chemical Society*, 128(5):1440–1441, 2006.

[15] Bruce R Rosen and Thomas J Brady. Principles of nuclear magnetic resonance for medical application. *Magnetic Resonance Imaging*, 2(2):158, 1984.

[16] Stephen Blundell. *Magnetism in Condensed Matter (Oxford master series in condensed matter physics)*. Oxford University Press, 2001.

[17] B. Bleaney A. Abragam. *Electron Paramagnetic Resonance of Transition Ions*. Oxford Classic Texts in the Physical Sciences. OUP Oxford, Oxford, 2012. Description based upon print version of record.

[18] E. Duin. Electron paramagnetic resonance theory e. duin. 2013.

[19] Yulia Krupskaya. *Magnetic Properties of Molecular and Nanoscale Magnets*. PhD thesis, 2011.

[20] Dante Gatteschi, Roberta Sessoli, and Jacques Villain. *Molecular nanomagnets*, volume 5. Oxford University Press on Demand, 2006.

[21] Msia Tavhelidse. Statische und dynamische magnetische eigenschaften von metallorganischen ni2- und ni2-lanthanoid-verbindungen. Master's thesis, Kirchhoff-Institut für Physik, Heidleberg Universität, 2016.

[22] Jonathan D Lawrence. *Comprehensive High Frequency Electron Paramagnetic Resonance Studies of Single Molecule Magnets*. PhD thesis, 2007.

[23] AB Millimetre. A quick overview of the mvna-8-350 millimeter vector network analyzer produced by ab millimetre.

[24] Originpro documentation http://www.originlab.com/origin.

[25] Easyspin documentation http://easyspin.org/easyspin/documentation/.

[26] Michael Großhauser. *Molekularer Magnetismus von homo-und heterooligonuklearen phenolatverbrückten 3d-4f-Verbindungen*. PhD thesis, 2015.

[27] Dennis Müller. *Theoretische Beschreibung der magnetischen Anisotropie in homo-und hetero-oligonuklearen 3d-4f-Verbindungen*. PhD thesis, 2015.

[28] Private mail exchange with dennis müller, inorganic chemistry, universität heidleberg, 2016.